UNIVERSITY OF SOUTHERN CALIFORNIA
DEPARTMENT OF CIVIL ENGINEERING

BROAD BAND EXTENSION OF FOURIER AMPLITUDE SPECTRA OF STRONG MOTION ACCELERATION

by

Mihailo D. Trifunac

Report No. CE 93-01

March, 1993

Los Angeles, California

ABSTRACT

This report reviews the physical bases and the observations of strong earthquake ground motion for quantitative extrapolation of spectral amplitudes to long ($T > 10$ sec) and to short ($T < .04$ sec) periods. This will serve as a basis for the subsequent formulation of empirical scaling equations for the response spectrum amplitudes in the same broad frequency band. The present empirical scaling equations of response spectrum amplitudes are limited to periods between .04 and 10 seconds. As the design of long structures and of structures on multiple distant supports requires knowledge and specification of design ground motions well beyond this frequency range, this report addresses the first important step in the extrapolation of the available response spectrum amplitudes, and deals with the formulation of the physical basis for such extrapolation.

ACKNOWLEDGEMENTS

This report summarizes a part of our effort in establishing the basis for development of smooth elastic response spectra for use in seismic design in Southern California. This work has been supported in part by the joint project of the California Department of Transportation and the City and County of Los Angeles. This project is entitled "The Characteristics of Earthquake Ground Motions for Seismic Design". This report addresses the topics in Task H-1 of the above project and deals with the "Characteristics of Earthquake Response Spectra in Southern California". The financial support from the California Department of Transportation and the City and County of Los Angeles, as well as the organizational support from the Southern California Earthquake Center, are gratefully acknowledged.

TABLE OF CONTENTS

I. GENERAL INTRODUCTION

The earthquake resistant design of extended soils and structures (such as tunnels, channels, dams, landfills and reclaimed land) and of structures with multiple supports (such as bridges, aqueducts, pipelines and transmission lines) requires that the specification of the design motions be given in a broad frequency range which may extend beyond the currently available strong motion data. Irrespective wether the analysis and the design are carried out using spectrum superposition methods or computer simulation of the response in the time domain (nonlinear analysis), it is possible to view the response of extended structures as a combination of two parts: 1) the pseudo static response caused by the differential motions of extended or multiple foundations, and 2) the dynamic response resulting from the action of the inertial forces (Kashefi and Trifunac, 1986; Kojić and Trifunac 1991a,b).

The fundamental periods of vibration of long bridges are in the range longer than 5 seconds. Depending on the local soil and geologic site conditions, these frequencies may correspond to wave lengths in the range from about 1 km to about 50 km. At high frequencies (for example a wave with period $T = .1$ sec, propagating through soft soil with wave velocity of, say, 100 m/sec, will have wave length of 10 m), the waves shorter than the bridge spans or the tunnel lengths will contribute differential motions which may lead to significant quasi-static contribution to the shears and moments in the structural components, and to large relative sliding and rigid body motions in statically determinate structures. Thus, as our ultimate aim is to present a general, broad band description of spectra of strong ground motion in California, we begin by analyzing the physical basis for extension of the spectral amplitudes to short and to long periods, but well beyond the currently available frequency band $\sim$ .1 to 25 Hz. Once this extension has been accomplished for the Fourier amplitude spectra, it will be simple to extend these results to scaling of the response spectrum amplitudes.

This report is divided into four chapters. Following this general introduction, Chapter II examines the extension of the existing empirical scaling equations to prediction of spectral amplitudes for long periods ($T > 10$ sec). Chapter III analyses the existing data and interpretations in the intermediate frequency range (.1 to 25 Hz), and attempts to reconcile the observed trends with the plausible interpretation of the physical phenomena at the earthquake source. The fourth Chapter presents an extension of the available spectra to high frequencies ($f > 25$ Hz), and analyzes the physical implications of the relationships presented here with other independent high frequency studies. All the chapters have been organized into self contained units and have separate discussions, conclusions, and references.

II. LONG PERIOD FOURIER AMPLITUDE SPECTRA OF STRONG MOTION ACCELERATION

The empirical equations for scaling Fourier amplitude spectra in the frequency band from $\sim$ .1 to 25 Hz can be extrapolated to describe the long period strong motion amplitudes. The results of this extrapolation can agree with (1) the seismological and field estimates of permanent ground displacement (near field), and with (2) the independent estimates of seismic moment and the observed corner frequencies of far field Fourier spectrum amplitudes.

II.1 INTRODUCTION

Since the 1960's and the early 1970's, following the pioneering works of Haskell (1964; 1969) and Brune (1970), numerous studies and interpretations were published dealing with spectral representation of the physical processes at the earthquake source (Anderson, 1991). From those, we learned that the corner frequencies in the observed far-field spectra can be associated with the characteristic source dimensions, that the high frequency fall-off of ground displacement amplitudes, beyond the corner frequency, can be described by ω^{-n} (where n is in the range between 2 and 3), and that the zero frequency spectral amplitudes can be related to the seismic moment M_0 (Keilis-Borok, 1960). During the following 20 years, many papers were published on (1) the physical interpretations of the processes at the earthquake source and their influence on the shape and amplitudes of the far-field displacement spectra, (2) the simple source characteristics as determined by the measured features of the observed far-field spectra, and (3) the use of the inferred source characteristics and the statistics of the observed source parameters to predict spectra of future strong and distant ground motion.

Simultaneously, in earthquake engineering, the strong motion data base was growing, and the first studies of the near field spectral characteristics using strong motion accelerograms at distances typically less than 100 km could be carried out. At present, detailed empirical equations are available to describe the Fourier amplitude spectra of strong motion acceleration in the frequency range from $\sim$ 0.1 to 25 Hz and for distances between about 10 and 100 km (e.g., Trifunac, 1989a,b).

The purpose of this chapter is to address mainly two questions: (1) is it possible to extrapolate the empirical equations for scaling Fourier amplitude spectra of strong ground motion, near the source, to frequencies $f < 0.1$ Hz, and (2) can thus extrapolated spectral amplitudes be tested and used to verify the physical continuity between the observations in the near field and at intermediate and teleseismic distances. The engineering need for such information continues to grow with design of long bridges, fluid storage tanks, large dams and long tunnels, for example. Also, providing consistent and continuous spectral representation of earthquake wave amplitudes for long period motions and from small to large distances, should help in the studies and in the use of distant spectral amplitudes. Earthquake ground motion recorded by strong motion accelerographs contains fairly complete and reliable information on the earthquake source,

because the scattering, diffraction, geometrical spreading, and inelastic attenuation along the wave path are smaller than for other distant recordings. The proximity to the source offers more detailed, direct and more complete data on strong ground motion, and thus can be used to (1) check and calibrate the distant recordings, and (2) learn more about the high frequency features of the earthquake source.

This study differs from many seismological analyses in that it uses regression equations in the frequency band from $\sim .1$ to 25 Hz, and is based on actually recorded strong motion data in the western U.S. and mainly in California. Our equations have terms which can be attributed to the processes at the earthquake source, the attenuation along the wave path and the observed ground motion in general, but in the end represent a carefully chosen empirical regression models, with coefficients and coefficient functions significantly different from zero in the frequency band considered. In this chapter, we do not modify these equations, but merely explore how those can be extrapolated to lower ($f \leq .1$ Hz) frequencies.

In contrast, most seismological studies assume functional forms for the spectral amplitudes, for example following Brune's (1970) shear wave spectra (e.g., Boore, 1983; Joyner, 1984), or assume a physical model of the source which then results in a functional form which determines these spectral estimates (e.g. Aki, 1967; Boatwright, 1988; Gusev, 1983; Papegeorgiou and Aki, 1983, 1985). These models are specified by the scaling parameters: seismic moment, M_0, one or two long period corner frequencies (f_1 and f_2 which are inversely proportional to the source dimensions), some form of stress drop on the fault plane, and the low-pass filtering characteristics of the surrounding medium ($f_{\max}$, Hanks, 1982) or the non-linear phenomena at the tip of a propagating dislocation (Papageorgiou, 1988). Since M_0 determines the long period spectral amplitudes, while the stress drop characterizes the high frequencies, such models provide means to interpolate the spectral behavior for the intermediate frequency band. In the end, these results can be calibrated in part using the recorded strong motion data (e.g., Gusev, 1983; Papageoriou and Aki, 1985), but their accuracy finally depends on one's ability to predict M_0 and the stress drop.

In the following sections, we will extrapolate the near-field spectra of strong motion acceleration $FS_{NF}(\omega)$ (see Eq. (13)), by using equations whose functional form can be related to the earthquake source theory. We will use the source theory to determine the shape of the spectra only. The spectral amplitudes will be chosen so that the assumed spectra have same amplitude as the empirically determined spectra (see Eq. (1)) at period $T(N_c)$, which will be defined in the following as the longest period for which Eq. (1) can be relied on.

To describe the spectra for the far-field strong motion acceleration, $FS_{FF}(\omega)$ (see Eq. (26)), we will assume that the shape of the Fourier spectral amplitudes can be described by functions which are similar to the body wave spectra in the Haskell (1969) source model. The amplitudes of the far field spectra will be determined by matching their amplitudes at $T(N_c)$ with the empirically determined spectra (Eq. (1)). Finally, to present the spectral amplitudes for all distances, we will consider a linear combina-

tion of the far field and of the near field spectra $a_{NF}FS_{NF}(\omega) + a_{FF}FS_{FF}(\omega)$, with $a_{NF} + a_{FF} = 1$ for all distances. The overall quality of this approach will be tested by comparing the implied (extrapolated) spectral amplitudes and their scaling parameters with independent measurements of various source and strong motion characteristics.

II.2 STRONG MOTION DATA

The strong motion acceleration data base started to grow from March 10, 1933, when the first strong motion accelerograms were recorded during the Long Beach (M = 6.3), earthquake in California. The San Fernando, California earthquake of February 9, 1971, contributed the first major increment to the strong motion data base. After all the accelerograms were digitized, together with selected older recordings from the period between 1933 and 1971, 186 uniformly processed free-field strong motion records were available (Trifunac, 1976a,b). Following the Imperial Valley, in 1979, the Coalinga in 1983, and the Morgan Hill in 1984, earthquakes in California, the uniformly processed strong motion data base more than doubled, to 493 uniformly processed records. With the recent recordings by the Los Angeles strong motion array (1987 through 1992) and following the Loma Prieta, 1989 California, earthquake, when all this data is uniformly processed, there will be well over 1000 excellent records in the strong motion data base.

II.3 EMPIRICAL SCALING EQUATIONS

The most recent equation for empirical scaling of Fourier amplitude spectra, $FS(T)$, is of the form

$$\begin{aligned}\log_{10} FS(T) = M + \mathcal{A}tt(\Delta, M, T) + b_1(T)M + b_2(T)h + b_3(T)\mathrm{v} + b_4(T)h\mathrm{v} \\ + b_5(T) + b_6(T)M^2 + b_7^{(1)}(T)S_L^{(1)} + b_7^{(2)}(T)S_L^{(2)},\end{aligned} \tag{1}$$

where M is the earthquake magnitude (Richter, 1958; Trifunac, 1991), $b_1(T)$ through $b_7^{(2)}(T)$ are scaling coefficient functions of the period T, and $\mathcal{A}tt(\Delta, M, T)$ is the frequency dependent attenuation function (Trifunac and Lee, 1990),

$$\mathcal{A}tt(\Delta, M, T) = \begin{cases} \mathcal{A}_0(T)\log_{10}\Delta; & R \le R_0 \\ \mathcal{A}_0(T)\log_{10}\Delta_0 - (R - R_0)/200; & R > R_0, \end{cases} \tag{2}$$

with Δ, the "representative" source to station distance,

$$\Delta = S \ln\left[\frac{R^2 + H^2 + S^2}{R^2 + H^2 + S_0^2}\right]^{-1/2}. \tag{3}$$

R is the epicentral distance and H is the focal depth, both in kilometers. R_0 is the transition distance (about 150 km for $T < 0.05$ and $\approx$ 50 km for $T > 1$ sec) beyond which the attenuation equation has slope equal to 1/200, and Δ_0 is the value of Δ in Eq. (3) when $R = R_0$ (more detailed description of R_0 can be found in Trifunac and Lee

1990). $\mathcal{A}tt(\Delta, M, T)$ depends on M implicitly, through S, which is the linearized "source dimension"

$$S = 0.2 + 8.51(M - 3), \text{ for } M > 3. \tag{4}$$

S_0 is the coherence radius of the source (Gusev, 1983) and is approximated by $S_0 \sim \beta T/2$, where β is the shear wave velocity in the source region, and T is the period of motion. When S/R and S_0/R become small, $\Delta \rightarrow (R^2 + H^2)^{1/2}$, which is the hypocentral distance to the source. $\mathcal{A}_0(T)$ in Eq. (2) is represented by a parabola (in $\log_{10} T$), between $T = 0.04$ and 1.8 sec. It is near -2 for $T = 0.04$, it increases to ~ -0.7 and remains constant for $T > 1.8$ sec (Trifunac and Lee, 1989).

h represents the thickness of the sedimentary layer, extending from the ground surface to the basement rock (in kilometers). v = 0 is for horizontal motion and v = 1 is for vertical motion. The term $b_4(T)h$v models progressively steeper incidence of body waves for soft and deeper sedimentary sites. $b_1(T)M$ and $b_6(T)M^2$ model the saturation of strong motion amplitudes versus M, for $-b_1(T)/(2b_6(T)) \equiv M_{\min} < M < M_{\max} \equiv -(1 + b_1(T))/(2b_6(T))$. $S_L^{(1)}$ and $S_L^{(2)}$ are indicator variables defined by

$$S_L^{(1)} = \begin{cases} 1 & \text{if } s_L = 1 \text{ (stiff soil)} \\ 0 & \text{otherwise} \end{cases} \quad \text{and} \quad S_L^{(2)} = \begin{cases} 1 & \text{if } s_L = 2 \text{ (deep soil)} \\ 0 & \text{otherwise} \end{cases} \tag{5}$$

where $s_L = 0$, 1 and 2 represent "rock", stiff soil and deep soil sites. The sites with soft to medium clays with strata of sands and gravels, as defined in the original investigation by Seed et al. (1976), are not common in the Western United States and are therefore not considered in this analysis.

With $\widehat{FS}(T)$ representing the Fourier amplitude spectra estimated from Eq. (1), and $FS(T)$ indicating the spectra computed from recorded accelerograms, the residues $\varepsilon(T)$ can be calculated from

$$\varepsilon(T) = \log_{10} FS(T) - \log_{10} \widehat{FS}(T). \tag{6}$$

$\varepsilon(T)$ can be described as a normal random variable with cumulative probability distribution function $p(\varepsilon, T)$, mean $\mu(T)$ and standard deviation $\sigma(T)$. Then,

$$p(\varepsilon, T) = \frac{1}{\sigma(T)\sqrt{2\pi}} \int_{-\infty}^{\varepsilon(T)} \exp\left[-\frac{1}{2}\left(\frac{x - \mu(T)}{\sigma(T)}\right)^2\right] dx \tag{7}$$

is the probability that $\log_{10} FS(T) - \log_{10} \widehat{FS}(T) \leq \varepsilon(T)$. Table I gives $b_1(T)$ through $b_7^{(2)}(T)$, $M_{\min}$, $M_{\max}$, $\mu(T)$ and $\sigma(T)$ at 12 periods $T(N)$, $N = 1, 2, ..., 12$, between $T(1) = 0.04$ and $T(12) = 14.0$ sec.

The first empirical model for scaling $\log_{10} FS(T)$ that involves the frequency dependent attenuation $\mathcal{A}tt(\Delta, M, T)$ was developed in 1985, but without explicit consideration of the soil site parameters s_L (Trifunac and Lee, 1985, 1987, 1989). Simultaneously with that analysis and with the model described above by Eq. (1), we studied also the geologic

site conditions using $s = 0, 1$ and 2, in place of h (see Trifunac and Brady, 1975, for definition and examples of site characterization with s, and Seed et al. 1976 for definition and examples of assigning s_L). The reader may wish to peruse the details on how these models have evolved, starting with our analysis in 1976 (Trifunac, 1976a), but for the purposes of this report it will suffice to recognize only the four most recent models:

1. MAG-SITE Model (Trifunac and Lee, 1989),

2. MAG-DEPTH Model (Trifunac and Lee, 1989),

3. MAG-SITE-SOIL Model (Trifunac, 1989b), and

4. MAG-DEPTH-SOIL Model (Trifunac, 1989a, Eq. (1) and Table I)

In what follows, we will use these four models collectively, and will refer to them as the "group of four recent scaling models" (G4RM). In the above, "MAG" implies scaling in terms of earthquake magnitude, "SITE" indicates the use of the geological site parameters $s = 0$, 1 or 2, and "DEPTH" implies the use of h as in Eq. (1) above. "SOIL" shows that the soil site parameters $s_L = 0$, 1 and 2 are used in the scaling equation. In the models 1 and 2 such dependence is omitted.

Fig. 1 illustrates $\log_{10} FS(T)$ plotted versus frequency, $f = \frac{1}{T}$. It shows Fourier amplitude spectra (dashed lines) for probability of exceedance equal to 50 percent ($p(\varepsilon,\ T) = 0.5$ in Eq. (7)), and for $M = 4$, 5, 6, 7 and 8 (bottom to top), at epicentral distance $R = 10$ km, and for source depth $H = 0$ km. For the long periods, the spectral amplitudes, computed from Eq. (1), are valid for progressively shorter periods ($T(N_c) = 1/f_{co}$) as the magnitude decreases and the source to station distance increases. This is caused by the recording and processing noise, whose spectral amplitudes are shown in Fig. 1 by the rectangular shaded zone, increasing from $FS \sim 10^{-1}$ in/sec for $f \sim 10$ Hz, to $FS \sim 1$ in/sec near $f = .1$ (Lee and Trifunac, 1990; Amini et al., 1982). At the high frequency end, the empirical spectra are defined only up to 25 Hz, the limit chosen more for convenience in data processing than for poor signal to noise ratio. At high frequencies, the spectral amplitudes recorded by the strong motion accelerographs have smaller amplitudes than what is shown in Fig. 1, because most strong motion transducers which contributed data to this database had natural frequencies between 14 Hz and 25 Hz (Trifunac and Hudson, 1970; Trifunac, 1971, 1972c; Lee et al., 1982). While the algorithms for correction of the instrument response and for reconstruction of the ground motion can be extended to apply for frequencies higher than 25 Hz, so far, we did not find it necessary to preserve the digitized data at sampling rate higher than 50 points per second (Lee and Trifunac, 1990). In Fig. 1, the top shaded area shows the region where the empirical Eq. (1) is valid. Table II shows the cut-off periods, $T(N_c) = 1/f_{co}$, versus magnitude. For uniformity, all G4RM empirical equations are defined for 12 periods $T(N)$, $N = 1, ..., 12$, listed in the first row of Table I, but can be used only for the periods with $N \leq N_c$ (in Table II).

Table I.

$$\log_{10} FS(T) = M_< + Att(\Delta, M, T) + b_1(T)M_{<>} + b_2(T)h + b_3(T)\mathrm{v} + b_4(T)h\mathrm{v} + b_5(T) + b_6(T)M^2_{<>} + b_7^{(1)}(T)S_L^{(1)} + b_7^{(2)}(T)S_L^{(2)}$$

$N =$	1	2	3	4	5	6	7	8	9	10	11	12
Period, T(sec)	0.040	0.065	0.11	0.19	0.34	0.50	0.90	1.60	2.80	4.40	7.50	14.0
Coefficients.												
$b_1(T)$	0.652	0.667	0.819	0.962	0.977	0.927	0.854	0.876	0.940	0.856	0.382	-0.707
$b_2(T)$	0.067	0.063	0.056	0.047	0.040	0.039	0.049	0.067	0.084	0.087	0.069	0.020
$b_3(T)$	0.127	0.091	-0.012	-0.155	-0.272	-0.292	-0.233	-0.152	-0.122	-0.126	-0.132	-0.131
$b_4(T)$	0.006	-0.002	-0.015	-0.030	-0.041	-0.047	-0.051	-0.048	-0.040	-0.033	-0.030	-0.034
$b_5(T)$	-3.921	-3.876	-4.151	-4.532	-4.809	-4.924	-5.151	-5.568	-5.881	-5.529	-3.791	-0.019
$b_6(T)$	-0.095	-0.098	-0.114	-0.127	-0.128	-0.123	-0.112	-0.110	-0.113	-0.110	-0.080	-0.006
$b_7^{(1)}(T)$	-0.314	-0.282	-0.219	-0.120	-0.008	0.052	0.120	0.161	0.161	0.127	0.065	-0.002
$b_7^{(2)}(T)$	-0.264	-0.260	-0.238	-0.151	-0.012	0.069	0.144	0.169	0.152	0.103	0.004	-0.144
$M_{\min}$	3.429	3.389	3.604	3.780	3.810	3.773	3.814	3.991	4.155	3.897	2.376	0.000
$M_{\max}$	8.691	8.472	8.006	7.711	7.711	7.845	8.282	8.549	8.576	8.450	8.600	14.500
$\mu(T)$	-0.002	-0.002	-0.002	-0.001	-0.001	-0.001	-0.002	-0.001	0.002	0.003	0.001	-0.001
$\sigma(T)$	0.445	0.462	0.388	0.343	0.316	0.317	0.338	0.352	0.343	0.328	0.315	0.305

$M_< = \min(M,\ M_{\max}), M_{<>} = \max(M_{\min},\ M_<)$

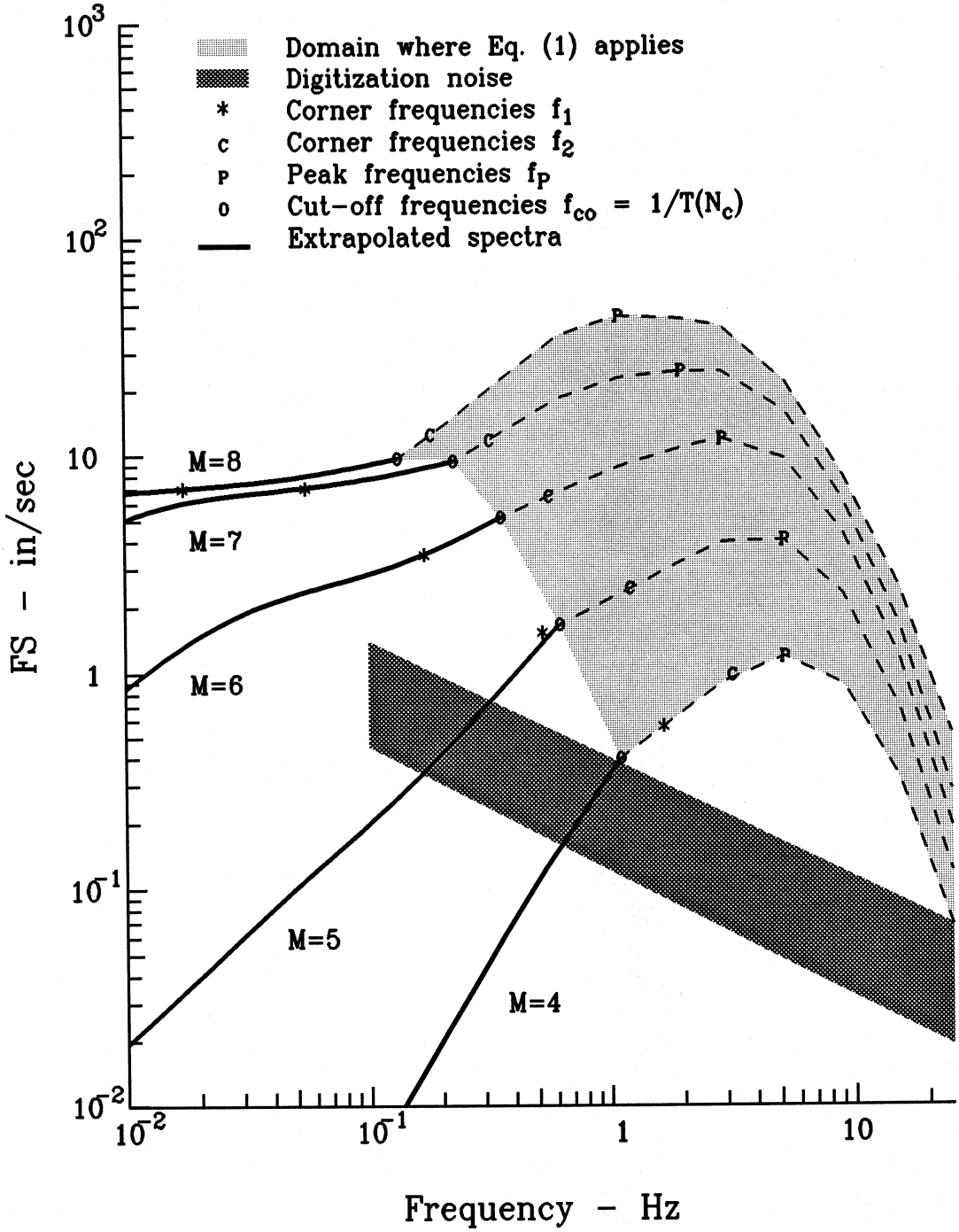

Fig. 1 Fourier amplitude spectra (in/sec) versus frequency (Hz), for probability of exceedance equal to 0.5, for $M = 4, 5, 6, 7$ and 8 (bottom to top), at epicentral distance $R = 10$ km, and for a source at depth $H = 0$. Outside the shaded region, between $f_{co} = 1/T(N_c)$ and $f = 25$ Hz where Eq. (1) is valid, the spectral amplitudes (heavy solid lines) can be extrapolated to $f < f_{co}$ as it is suggested in this paper. The corner frequencies f_1, f_2 and f_{co} are defined in the text. The processing and digitization noise amplitudes are shown by the shaded zone increasing from $FS \approx 10^{-1}$ to $FS \approx 1$ in/sec for frequencies decreasing from 10 to .1 Hz.

Table II.

Cut-off periods $T(N_c)$ versus magnitude

M	$T(N_c)$	N_c
3	.90	7
4	.90	7
5	1.60	8
6	2.80	9
7	4.40	10
8	7.50	11

In what follows, we will extend the spectral amplitudes to low frequencies, starting at the "end period", $T(N_c)$, of the spectra, as shown in Fig. 1 by the heavy solid lines for $T > T(N_c)$ sec ($f < f_{co} = 1/T(N_c)$). Also, all the spectra and the analysis will be based on the estimates of strong ground motion at sites on basement rock ($s = 2$ or $h = 0$) and on a "rock" soil site ($s_L = 0$). This will eliminate complications introduced by the local site conditions (Trifunac, 1990) and will allow more direct comparison with the seismological studies and observations. Finally, without loss of generality, we will use the results of Eq. (1) for horizontal motions only (v = 0) to further simplify the presentation and interpretation of these empirical equations.

II.4 LOW FREQUENCY EXTENSION

Two separate cases will be considered. In the first case, the recording site is so close to the earthquake source, that the ground will experience permanent static displacement after an earthquake. This will occur when the site is close to the fault surface, at a distance smaller than the characteristic source dimension. One can refer to this case as the "near-field" ground motion. In the second case, the recording station is far from the source, so that the contributions from the static displacement are negligible, that is, all near and intermediate field terms (Haskell, 1969), which attenuate as R^{-4} and R^{-2}, have become negligible, and only the body waves (attenuating like R^{-1}) and surface waves (attenuating like $R^{-1/2}$), where R is the source to station distance, will contribute to the strong motion amplitudes.

Near-Field Displacements

Following Brune (1970), we represent the near field displacement, $d_{NF}(t)$, by

$$d_{NF}(t) = d_p(1 - e^{-t/\tau}) \tag{8}$$

where d_p is the static displacement at the station (on ground surface) following the earthquake, t is the time, and τ is characteristic time, which will be related to the duration of the faulting. The real details of ground motion, of course, are more complicated. When the observation point is on the fault surface, the average of d_p can be described by

$$\bar{d} = \frac{1}{2} C_0 \frac{\sigma r}{\mu} \tag{9}$$

where σ is the effective stress drop, r is the equivalent (radius) dimension of the source area and μ is the rigidity in the source region (typically in the range from 1 to 5×10^{11} dynes/cm^2). C_0 is a "constant" which depends on the type of faulting and is in the range from .4 to 1.6 (Table III). The factor of 1/2 in Eq. (9) relates the displacement of a point (d_p) with the average source dislocation amplitude $\bar{u}$, which for symmetric faulting is $2\bar{d}$. The bars on u and d designate the average values. For a vertical strike slip fault of considerable length, L, the width, W, will be equal to ξW_* (where $0 \leq \xi \leq 1$ for a fault

Table III

$$\overline{u} = C_0 \sigma r/\mu, \quad \overline{u} = 2\overline{d}$$

Type of faulting and fault geometry	C_0	r represents
Dip-slip displacement along an infinitely long narrow strip in a uniform shear field[1]	$\frac{3\pi}{16}$	Fault width
Infinitely long vertical surface fault with strike slip displacement[2]	$\frac{\pi}{2}^*$ to $\frac{\pi}{4}^{**}$	Fault width
Circular fault plane in a infinite medium[3]	$\frac{8}{7\pi}^+$	Diameter of circular dislocation (Fault width)

(1) A.T. Star, Slip in a crystal and rupture in a solid due to shear, Cambridge Phil. Society Proc. 24, 489-500, (1928).

(2) L. Knopoff, Energy release in earthquakes, Geophys. J. 1, 44-52, (1958).

(3) V.I. Keilis-Borok, On estimation of the displacement in an earthquake source and of source dimensions, Annali Geofizica, 12, 205-214, (1959).

* Surface fault.

** Deep fault.

\+ Poisson ratio, $\nu = 0.25$.

Note: To model the assumed "continuous" changes of the faulting type and geometry, for the body of strong motion data studied here, I will define $C_0^* = .4$, .5, .65, .85, 1.6 and 1.6 for earthquake magnitudes M = 3,4,5,6,7 and 8. $C_0^* = .4$ is representative of small "circular" faults, while $C_0^* = 1.6$ will represent long surface faults.

rupturing the surface, and W_* is the fault width of a deep buried fault which does not break the ground surface). When $\xi = 1$, we can represent the dislocation amplitudes by $u = u_{\max}\left(\frac{4x}{W_*} - \frac{4x^2}{W_*^2}\right)$. Then, the average dislocation is $\overline{u}(\xi) = \left(2\xi - \frac{4}{3}\xi^2\right) u_{\max}$, where x is pointing up and is normal to the ground surface ($x = 0$ is at the bottom edge of the fault, ξW_* below ground surface). When $\xi = 1$ or when $\xi = 1/2$, $\overline{u} = \frac{2}{3}u_{\max}$. When $\xi = 3/4$, $\overline{u} = \frac{3}{4}u_{\max}$. On the ground surface, the peak dislocation amplitude, $2d_p$, and the peak particle displacement, d_p, are described by $d_p = \frac{1-\xi}{\frac{1}{2}-\frac{\xi}{3}}\left(\frac{u_{\max}}{2}\right)$. For $\xi \sim 0$, $\overline{d} = \overline{u}$, and for $\xi = 1$, $\overline{d} = 0$.

As the area of the fault surface, LW (L is fault length, and $W = \xi W_*$), increases with increasing magnitude, W becomes larger and $u_{\max}$ is located at progressively greater depths. Detailed source mechanism studies in California for the earthquakes which have contributed to the strong motion data base used here, suggest that the largest dislocation amplitudes do not occur near the ground surface (Archuleta, 1982; Harzell and Heaton, 1983; Harzell and Helmberger, 1982; Olson and Apsel, 1982; Trifunac, 1972a,b; 1974). During the Parkfield earthquake of 1966, the dislocation apparently occurred at depth (Trifunac and Udwadia, 1974) and its eventual surface expression grew through creep for about one year following the earthquake. For the purposes of this analysis, we need d_p (on ground surface), and since sufficient data is not available on the average displacement, $\overline{d}$, versus magnitude, faulting mechanisms, fault types and on the distribution of rigidities and stresses on the two sides of the fault (Scholz, 1982), we assume that the average of d_p occurs for $3/4 \leq \xi \leq 1$, and approximate it by

$$\overline{d} \sim \frac{3}{4}\frac{\overline{u}}{2}. \tag{10}$$

The Fourier amplitude spectrum of $d_{NF}(t)$ in Eq. (8) is

$$\Omega_{NF}(\omega) = \frac{d_p}{\tau\omega}\frac{1}{(\omega^2 + \tau^{-2})^{1/2}}. \tag{11}$$

When $\omega \to 0$, $\Omega_{NF}(\omega) \to d_p/\omega$. Using the approximate relationship between d_p and $\overline{u}$ in Eq. (10), this implies that

$$\overline{\Omega}_{\substack{NF \\ \omega\to 0}} \to\approx \frac{3}{8}\frac{\overline{u}}{\omega}. \tag{12}$$

The fluctuations of d_p on the ground surface are considerable, and will depend on the relative position of the observation point with respect to the fault surface and the three-dimensional properties of the geologic medium surrounding the fault. Since we are dealing here with empirical scaling of Fourier spectrum amplitudes, and because our model equation (e.g., Eq. (1)) represents the average trends for many observations, it will suffice for the purposes of this analysis to deal with the average trends of d_p as in the above equations.

For Fourier amplitude spectra of strong motion acceleration in the near field, $FS_{NF}(\omega)$, Eq. (11) gives

$$FS_{NF}(\omega) = \frac{\omega d_p}{[(\omega\tau)^2 + 1]^{1/2}} \tag{13}$$

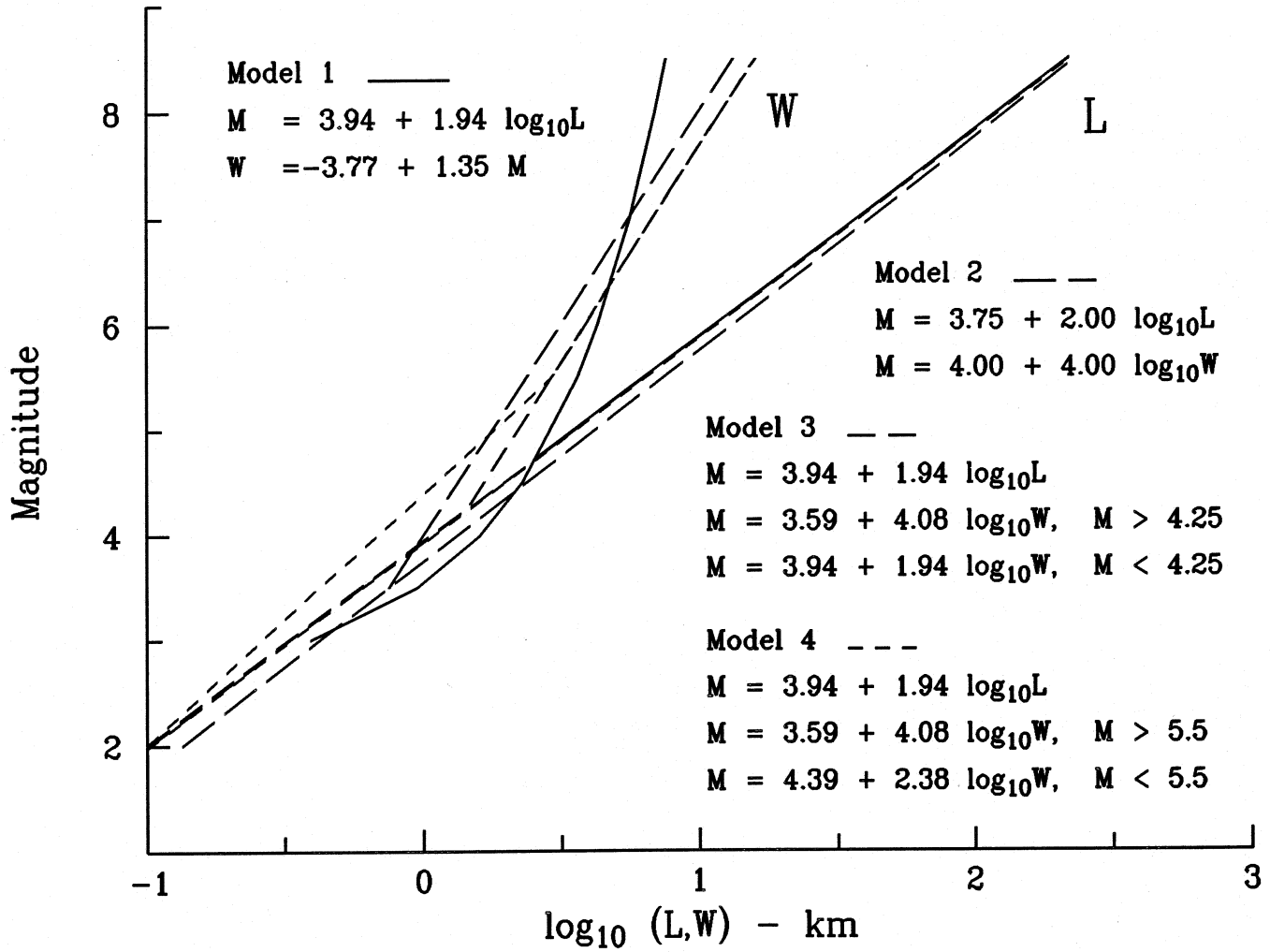

Fig. 2 Fault length (L) and width (W) versus earthquake magnitude for models 1, 2, 3 and 4.

where τ can be approximated by $\tau \sim r/\beta$ (β is the velocity of shear waves) when $r < W/2$. When $L >> W$, $\tau \approx \frac{L}{v} + T_0$, where v is the average velocity with which the dislocation propagates along the fault length, and T_0 is the dislocation rise time (Haskell, 1969). For $\frac{L}{v} >> T_0$, the corner frequency $f_1 = \frac{\omega_1}{2\pi} \rightarrow \frac{v}{L}$. For intermediate frequencies, $f_1 = \left[\frac{L}{v} + T_0\right]^{-1}$, with typical value of $v = 2.2$ km/sec, $T_0 \sim \frac{W}{2\beta}$, and $\beta \sim 3.0$ km/sec. Here, it may be assumed that for typical strike slip faulting in California, the dislocation grows more or less as a circular dislocation up to $r \leq W/2$. When the size of W has been reached, we assume that the fault surface grows in terms of L only. Thus, we approximate $\omega\tau$ in Eq. (13) by

$$\omega\tau \approx \frac{2\pi}{T}\left(\frac{L}{2.2} + \frac{W}{6}\right). \tag{14}$$

For intra-plate earthquakes, the estimates of the fault width, W, suggest growth of $\log_{10} W$ versus magnitude, up to $W \approx 5$ to 10 km and for $M \approx 6$. For larger magnitude events, W seems to become independent of magnitude (Chinnery, 1969). Correlations of the fault length, L, and magnitude show large fluctuations (for $3 \leq M \leq 8$), but most estimates tend to fall between

$$L_{\min} \approx a \times 10^{bM} \tag{15a}$$

and

$$L_{\max} \approx 0.20 \times 10^{.40M} \tag{15b}$$

where L is measured in kilometers (Jovanovich et al., 1974a,b).

The fault width W can be approximated by

$$W = c \times 10^{dM} \tag{16a}$$

or by

$$W = e + fM. \tag{16b}$$

Table IV presents the coefficients a through f for the four cases (referred to as fault models 1 through 4) used as examples in this study (Fig. 2). As will be seen from the following, it is remarkable that both L and W can be approximated with so simple functional forms and for such a broad range of magnitudes. Furthermore, various constraints on the spectral amplitudes limit the permissible fluctuations of L and W to a relatively narrow range, making fault models 1 through 4 very similar, and thus controlling the possible range of the coefficients a,b,c,d,e and f, which were chosen here by trial and error.

In Eq. (14) we choose $L = a \times 10^{bM}$, which corresponds to $L_{\min}$ already mentioned in Eq. (15) and for a and b as given in Table IV. We also choose $W_{\min} = W$ (as in Eq. (16)). As will be clear from the following, $L_{\min}$ and $W_{\min}$ correspond to the smallest fault dimensions for unilateral faulting. For bilateral symmetric faulting $L \sim 2L_{\min}$ and $W \sim 2W_{\min}$.

Table IV

Coefficients a and b in $L_{\min} = a \times 10^{bM}$ and c and d in $W = c \times 10^{dM}$

	fault length $L_{\min}$: (km)			fault width W: (km)		
Model[1]	a	b	conditions			
1	.0936	.514	$M > 4.77^*$	$W = \begin{cases} -3.77 + 1.347M \\ .131M \end{cases}$		$M > 3.1^*$ $M < 3.1$
				c	d	
2	.0133	.50		.1 $W = L$	.25 for	$M > 3.5^*$ $M < 3.5$
3	.00931	.515		.132 $W = L$	.245 for	$M > 4.25^*$ $M < 4.25$
4	.00931	.515		.132 .0145	.245 .419	$M > 5.5^*$ $M < 5.5$

* in the text these magnitudes are designated by M_*

[1] Fault models 1 through 4 have been chosen to illustrate the plausible variations in W and L (allowed by the data), and the consequences of these variations on other characteristics of the models.

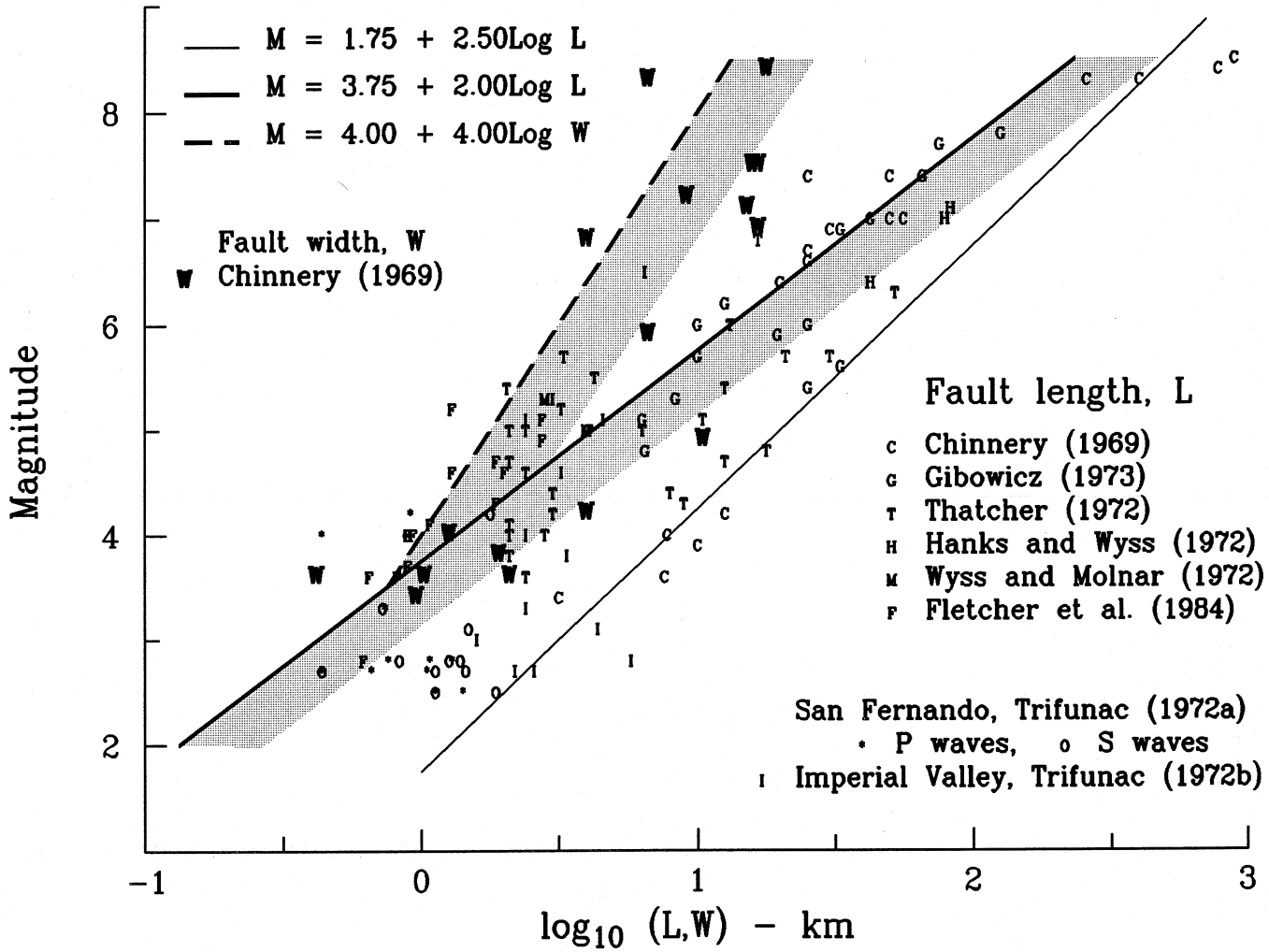

Fig. 3 Field and instrumental estimates of the fault width (W) and the fault length (L) versus magnitude M. $L_{\min}$ and $W_{\min}$ (e.g. for Model 2), assuming unilateral propagation of the dislocation, are shown by heavy continuous (L) and broken lines (W). Symmetrically bilateral faults would result in two times larger fault dimensions. All other faulting falls between these two estimates and is shown by shaded zones in this figure.

Comparison with Other Estimates of L and W

For small intra-plate sources (e.g. $M < 4$ to 5), the fault length, L, and width, W, are about the same. For larger earthquakes, the fault continues to grow mainly through L, while W may only continue to increase slowly until it reaches the width of the seismogenic zone. A range of models describing W in terms of M has been considered in this report. This analysis showed that the permissible variations of W versus magnitude are controlled well by the available data and suggested typical models with $W = L$ for $M < M_*$ and $W = c \times 10^{dM}$ for $M > M_*$ (Table IV). This dependence of L and W on magnitude is in good agreement with the data on the field estimates of L and W (Fig. 3) and with the data on a corner frequency, f_2, which is seen in the far-field spectra of shear waves (f_2 in Papageorgiou, 1988), which can be approximated by $2.2/W$, as will be discussed later.

In Fig. 3, the shaded zone to the right of $L_{\min}$ and $W_{\min}$ (see Eq. (15a) and (16)) outlines the range $L_{\min} < L < 2L_{\min}$, and $W_{\min} < W < 2W_{\min}$ in this example for the fault model 2. In $\tau = \frac{L}{v} + \frac{W}{2\beta}$, it is implicitly assumed that $L >> W$, and, so, τ is defined by a dislocation propagating unilaterally $L_{\min}$ kilometers from the focus at one end of the fault, towards the other end of the fault. Since it is the duration of faulting which is constrained by $\omega\tau$ and is fitted to the strong motion spectral amplitudes, it is seen that, for bilateral faulting, our scaling implies that the fault length $L = 2L_{\min}$. Thus, all field observations of fault length falling between $L_{\min}$ and $2L_{\min}$ would be in agreement with our interpretation of near-field strong motion data, assuming some distribution of events in the range between unilateral and bilateral faulting. Detailed comparison of our estimates (exemplified by the fault models 1 through 4) with field and seismological estimates of fault length and width (Fig. 3) indicates fair agreement (e.g. Jovanovitch et al., 1974a,b).

Permanent Displacements

By computing Fourier spectrum amplitudes (in the near field) for $T \to \infty$, it is possible to evaluate the average dislocation $\overline{u}$ (in cm) implied by the G4RM models and by the choices for L and W (Table IV). For this, we first equate Eqs. (1) and (13) at $\omega_c = 2\pi/T_c$, assuming that $\omega\tau$ is given by Eq. (14) (L and W are computed from Eqs. (15) and (16) for given M) and compute d_p. Then, letting $\omega \to 0$ in Eq. (11), and multiplying d_p by 2 we obtain $\overline{u}$. The result can be compared with other independent estimates of $\overline{u}$. For continuity with the previous studies (Trifunac, 1976b), and to focus on earthquakes which contributed to this data base, we use the data on $\overline{u}$, as shown in Fig. 4. The shaded regions correspond to $\overline{u}$ estimated from the G4RM, for probabilities $p(\varepsilon, T)$ of exceedance (Eq. (7)) equal to 0.1, 0.5 and 0.9, and for the fault model 3 as an example. It is seen that the trends of $\overline{u}$ associated with the G4RM are in excellent agreement with our estimates of $\overline{u}$ using strong motion data, but are larger than the estimates of Thatcher and Hanks (1973), which are based on distant seismological recordings.

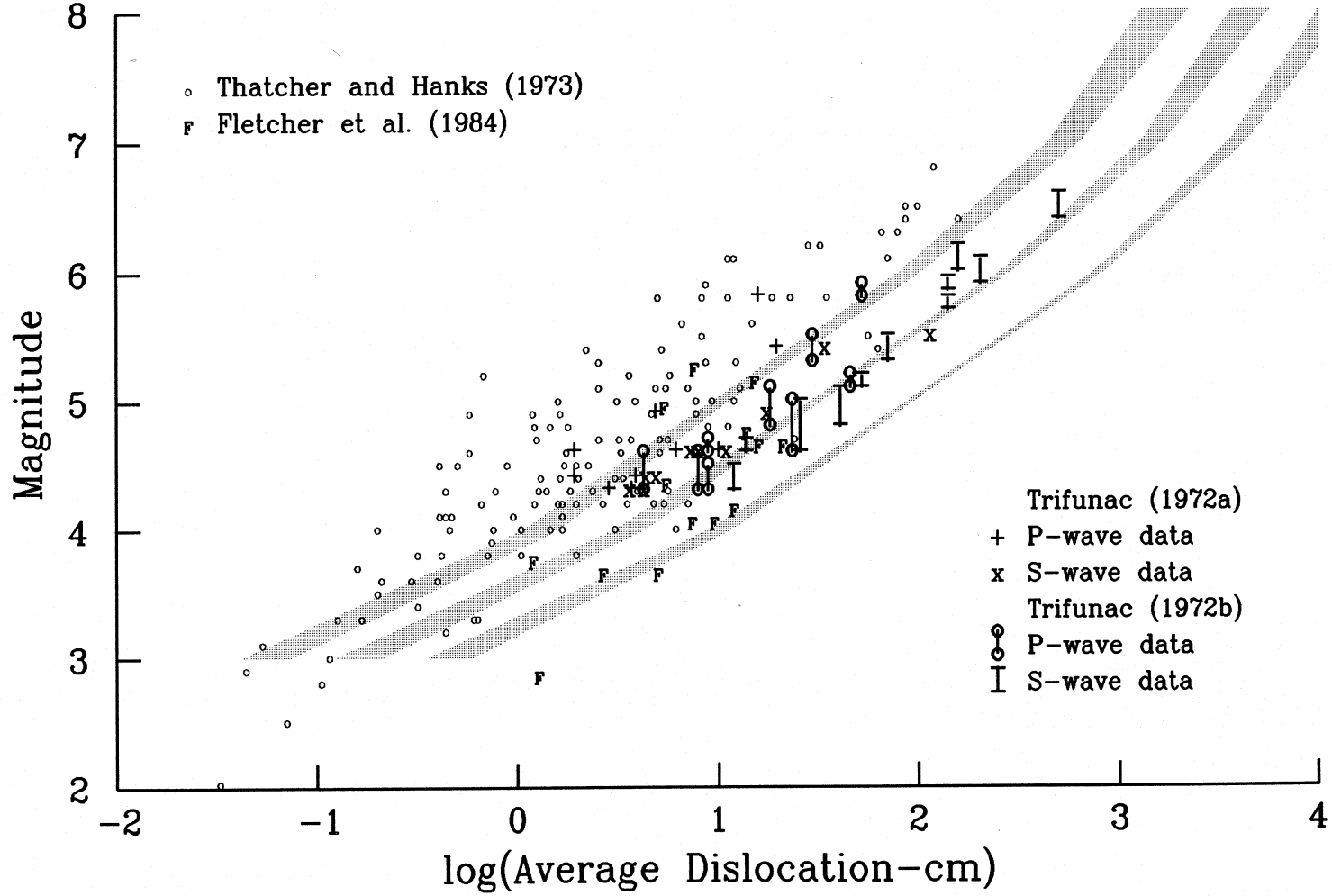

Fig. 4 Comparison of seismically measured (Thatcher and Hanks, 1973; Fletcher et al., 1984; and Trifunac 1972a,b) and calculated (using G4RM) average dislocation, $\overline{u}$, versus magnitude, M. The three shaded bands show the range of $\overline{u}$ for probabilities of exceedance equal to .1, .5 and .9. The variations within each band show the fluctuations and differences among the four scaling models (1. MAG-SITE, 2. MAG-DEPTH, 3. MAG-SITE-SOIL and 4. MAG-DEPTH-SOIL) and for the fault model 3 representation of L and W (see Table IV).

Careful analysis of the accuracy of $\overline{u}$ will reveal that considerable simplifications are required to obtain the data shown in Fig. 4. Likewise, the above extrapolation of $FS(T \rightarrow \infty)$, using Eq. (13), to evaluate $FS(T)$ for $T > T(N_c)$ depends on the proper choice of $\omega\tau$ versus M (i.e. choice of L versus M) and on selection of N_c in $T(N_c)$. Yet, the agreement of the estimated $\overline{u}$ (using Eq. (1) and (13) at ω_c), with the independent estimates in Fig. 4 suggests that the empirical spectral amplitudes of $FS(T)$ contain most of the relevant information, up to and including $T = T(N_c)$, to define the average $FS_{NF}(T)$ for $T >> T(N_c)$.

Far-Field Displacements

As the observation point moves away from the source, the permanent offset (d_p) goes to zero and the ground displacement experiences only a "transient pulse" which could be characterized by the Brune's (1970) pulse,

$$d_{FF}(t) \approx \frac{r}{R}\frac{\sigma\beta}{\mu} t' e^{-\alpha t'} \quad , t' \geq 0 \tag{17}$$

where $t' = t - R/\beta$ (r is the source dimension, σ = Brune's effective stress drop, β = shear wave velocity, R = source to station distance, and μ = rigidity). The Fourier amplitude spectrum of d_{FF} in Eq. (17) is

$$\Omega_{FF}(\omega) \approx \frac{r}{R}\frac{\sigma\beta}{\mu}\frac{1}{\omega^2 + \alpha^2} \tag{18}$$

and the strong motion acceleration spectrum is

$$FS_{FF}(\omega) \approx \frac{r}{R}\frac{\sigma\beta}{\mu}\frac{1}{1 + \left(\frac{\alpha}{\omega}\right)^2}. \tag{19}$$

Since $\alpha \approx 2.34\beta/r$ (Brune, 1970), and assuming that $r \sim L/2$ ($r \sim W/2$), for $\beta \approx 3$ km/sec, $\alpha/\omega \sim 2.23T/L$. As $T \rightarrow \infty$, Eq. (19) implies that $FS(T)_{FF} \sim 1/T^2$. Also, since

$$\Omega_{\substack{FF \\ \omega \rightarrow 0}}(\omega) \rightarrow M_0(4\pi\rho R\beta^3)^{-1}, \tag{20}$$

$$FS_{\substack{FF \\ \omega \rightarrow 0}}(T) \rightarrow \frac{\pi M_0}{\rho R\beta^3 T^2}, \tag{21}$$

where $\rho = \mu/\beta^2$ and M_0 is the seismic moment defined by

$$M_0 = \mu\overline{u}A. \tag{22}$$

$\overline{u}$ is the dislocation amplitude ($\overline{u} \sim 2\overline{d}$) averaged over the fault surface A.

Using the Haskell's (1969) representation in the far-field, for S waves, it is possible to compute the Fourier amplitude spectra of the ground displacement, if the dislocation

function is specified on the fault surface. Assuming that this dislocation grows linearly during time T_0, until the final dislocation amplitude is reached, and that this dislocation propagates along the fault of length L, with constant velocity v, it can be shown that

$$|\Omega_{FF}| \sim \left| \frac{\sin \frac{\omega L}{2v}}{\frac{\omega L}{2v}} \right| \cdot \left| \frac{\sin \frac{\omega T_0}{2}}{\frac{\omega T_0}{2}} \right| . \tag{23}$$

Eq. (23) is characterized by two corner frequencies, one, f_1, associated with the duration of faulting (L/v) and the other, f_2, with the duration of the dislocation rise time T_0. As $\omega \to \infty$, like Eq. (18), Eq. (23) implies $\Omega_{FF} \sim 1/\omega^2$.

If one assumes a dislocation buildup function of the form $1 - \exp(-t/T_0)$, for $t > 0$, then (Savage, 1972)

$$|\Omega_{FF}| \sim \frac{\sin \frac{\omega L}{2v}}{\frac{\omega L}{2v}} \cdot \frac{1}{(1+\omega^2 T_0^2)^{1/2}}, \tag{24}$$

If it is assumed that the duration of the slip is controlled by the narrow dimension of the fault W, then the displacement rise time is $T_0 \sim W/2v$. Assuming that this time should roughly correspond to 90% of the maximum dislocation, gives $2.3T_0 = W/2v$ (Savage, 1972) and the second corner frequency

$$\omega_2 = 4.6\ v/W\ . \tag{25}$$

For $v \approx 3$ km/sec, $f_2 = 2.2/W$. The other corner frequency, $\omega_1 \approx 2\pi v/L$, depends on the duration of faulting L/v.

Guided by the above results, we chose to approximate Ω_{FF} by

$$\Omega_{FF}(T) = C_s \frac{1}{\left[1 + \left(\frac{W}{2.2T}\right)^2\right]^{1/2}} \cdot \frac{1}{1 + \frac{\tau}{T}} \tag{26}$$

where the constant C_s can be computed from

$$C_s = FS_{FF}(\omega_c)\omega_c^{-2} \left[1 + \left(\frac{W}{2.2T_c}\right)^2\right]^{1/2} \left(1 + \frac{\tau}{T_c}\right) \tag{27}$$

with $\omega_c = 2\pi/T_c$ and $T_c \equiv T(N_c)$ (see Table II), and where $FS_{FF}(\omega_c)$ is set equal to the spectral amplitude computed from Eq. (1) or its equivalent for one of the four models (G4RM).

The empirical estimates of the spectral amplitudes in Eq. (1), for $\Delta = 0$, first decrease with T approaching T_c and then begin to curve up near $T = T_c$ and for $T > T_c$. In part, this is due to the decreasing signal to noise ratio in the recorded accelerograms (Lee et al., 1982; Lee and Trifunac, 1990), but we also assume that it results from the

gradual transition of the empirically computed spectral amplitudes to the slopes which are analogous to those defined by Eq. (13), for $\omega < 2\pi/T(N_c)$. In this work, we chose first N_c so that $T(N_c)$ is near such turning points. Then, as it will become clear from the following, by trial and error, we selected the final values of N_c (see Table II) to obtain the "best fit" with various data and known constraints. In the end, for the far-field strong motion amplitudes, we use Eq. (1) to predict $FS(T)$ for $T < T(N_c)$ and $\omega^2\Omega_{FF}$, with Ω_{FF} given by Eq. (26), and C_s computed from Eq. (27).

Comparison of M_0 Determined from Strong Motion Accelerograms with Other Estimates

Eqs. (23), (24) and (27) result from a simplified consideration of the shear wave spectra only, while $FS(T)$ estimated from Eq. (1), via one of the G4RM, represent the Fourier amplitudes of the complete strong motion signal including all the waves. In our recent work on local magnitude scale computed from strong motion accelerograms, M_L^{SM} (Trifunac, 1991), we found that using the complete time history of strong motion near a source leads to systematically larger estimates, when compared with more distant seismological estimates of M_L. This difference $D\left(\overline{M}_L^{SM}\right) = M_L^{SM} - M_p$ (where M_p is the published magnitude), for the strong motion data in the Western U.S., is summarized in Table V. It can be used to adjust the moment M_0^{SM}, computed from Eqs. (21) and (27), to agree with the distant (say further than 200 km) estimates of the moment M_0

$$\log_{10} M_0 \approx \log_{10} M_0^{SM} - \mathrm{k}D(\overline{M}_L^{SM}). \tag{28}$$

In Eq. (28), the factor k is the empirical slope of $\log_{10} M_0$ versus M (e.g. Wyss and Brune, 1968), and M_0^{SM} is the seismic moment computed from Eqs. (20), (26) and (27) using the strong motion data in terms of the G4RM. We used k = 1 for $M < 4.5$, k = 1.25 for $4.5 \leq M < 5$, k = 1.5 for $5 \leq M < 7$, and k = 1.3 for $M \geq 7$, in Eq. (28).

Eq. (28) can be used then to evaluate M_0 from M_0^{SM}, and to compare it with other independent distant (> 200 km) estimates. This is shown in Fig. 5, where the three shaded zones, for probabilities of exceedance equal to 0.1, 0.5 and 0.9, show $\log_{10} M_0$ versus magnitude. In this calculation, we used the variable value of $\mu\beta$ as follows. The typical shear wave velocity in the source region was assumed to increase linearly from 0.5 km/sec at the surface to 4 km/sec at depth of 10 km. The material density was also assumed to increase linearly, from 2 gr/cm^2 at the surface to 3 gr/cm^3 at depth of 10 km. The fault surface was assumed to be vertical with the lower long edge (along L) at $H = 10$ km, and with the top edge at $H - W$ (km). μ and ρ were calculated at depth $H - W/2$, for W specified by one of the four fault models (see Fig. 2 and Table IV). The resulting $\mu\beta$ ranged from 4.7×10^{16} dyne/cm/sec (for $M = 8$) to 18.12×10^{16} dyne/cm/sec (for $M = 3$). The straight line given by $\log_{10} M_0 = 1.5M_0 + 16$, and some data on field and seismic estimates of the moment M_0 using body wave spectra and using strong motion data are also shown in Fig. 5. It is seen that the agreement between our

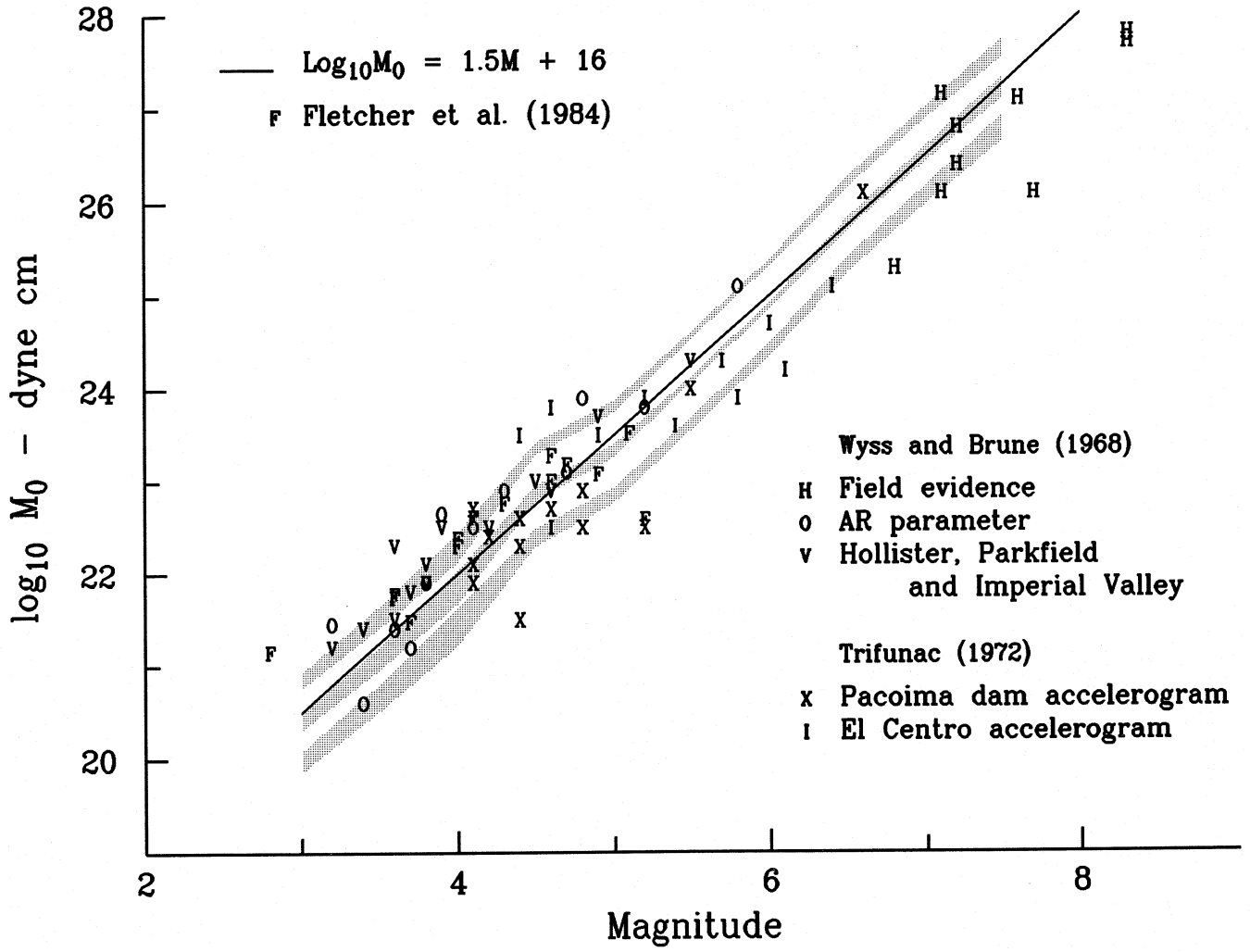

Fig. 5 M_0 versus M for selected teleseismic (Wyss and Brune, 1968) and strong motion estimates (Fletcher et al., 1984; and Trifunac 1972a,b) of M_0. The three shaded regions show the range of estimates for three probabilities of exceedance (0.1, 0.5 and 0.9), computed for the G4RM.

Table V*

$D\left(\overline{M}_L^{SM}\right) = \overline{M}_L^{SM**} - M_p^{***}$ versus M_p

M_p	$D\left(\overline{M}_L^{SM}\right)$	M_p	$D\left(\overline{M}_L^{SM}\right)$
3.1	1.30[1](1.70)*	6.4	0.27(0.29)
3.5	1.24(1.60)	6.8	0.03
4.0	1.15(1.45)	7.0	-0.11
4.5	1.05(1.26)	7.4	-0.40
5.0	0.9(1.05)	7.7	-0.63
5.5	0.72(0.81)	8.0	-0.87
6.0	0.47(0.53)		

* from Trifunac (1991a)

** $\overline{M}_L^{SM}$, local magnitude estimated from computed response of Wood-Anderson seismograph excited by the recorded strong motion acceleration.

*** M_p is the published earthquake magnitude typicaly corresponding to M_L for $M_p \leq 6.5$.

[1] $D(\overline{M}_L^{SM})$ as used in this study is based on the subjective manual fit of the data (Trifunac, 1991b) in the low magnitude range, typically $M < 5$. The values shown inside brackets represent the smooth parabolic fit to all data as in Trifunac (1991a).

estimates based on Eq. (20) and the above procedure, and the results from the previous studies is good.

A trend of departure of the data points on $\log_{10} M_0$ versus magnitude from a straight line (with the slope k $\sim$ 1.5) near $M = 4$ has been observed for several data sets in California and elsewhere (Hasegawa, 1983; Nuttli, 1983). Its explanation has been sought in terms of different stress drops for some $M < 4$ events, resulting in systematically higher corner frequencies (Bakun, 1984). Also this change occurs for events whose corner frequencies are close to the corner frequency of the Wood-Anderson seismometer (Boore, 1983; Fletcher et al., 1984). The physical considerations of the source mechanism, for most earthquakes (with rupture time longer than 5 to 10 seconds, and with rise time shorter than $\sim$ 5 sec), lead to $\log_{10} M_0 \sim 1.5M$. For small earthquakes (with magnitudes less than $\sim$ 4 to 5), having smaller dimensions and shorter rise time, $\log_{10} M_0 \sim M$ (Kanamori and Anderson, 1975; Vidal and Munguia, 1991).

Using the equation $\log_{10} E_S = 1.5M_s + 11.8$ to relate the surface wave magnitude, M_S, and the total energy of seismic waves, E_S (Gutenberg and Richter, 1956), and the equation $E_S = \eta\overline{\sigma}M_0/\mu$, where $\eta\overline{\sigma}$ is the apparent stress, leads to $\log_{10} M_0 = 1.5\ M_S + 11.8 - \log_{10} \frac{\eta\overline{\sigma}}{\mu}$. For $\eta\overline{\sigma} = 10$ bars, and equating M_S with M_L for magnitudes smaller than about 7, gives $\log_{10} M_0 = 1.5M + 16.1$. In Fig. 5, showing the trends for the G4RM and the four fault models (Table IV), it is seen that the average trend of $\log_{10} M_0$ versus M is close to $\eta\overline{\sigma} = 10$ to 20 bars.

For completeness of this discussion, we note that since $M_0 = \mu\overline{u}A$ and $A \approx ac \times 10^{(b+d)M}$ (see Table IV), and $\overline{u} = C_0^*\sigma W/\mu$ (Table III), one can write $\log_{10} M_0 = \log_{10}(C_0^*\sigma ac^2) + (b+2d)M$. For $M < M_*$, $b + 2d \sim 1.5$, and for $M > M_*$, $b + 2d \sim 1.1$. Also, for $M \leq 4$, $\log_{10}\sigma \sim -.75 + \frac{M}{2}$, for $4 < M < 6$, $\log_{10}\sigma \sim \frac{1}{3}M$, and for $7 < M < 8$, $\log_{10}\sigma \sim 1.4 + (1/9)M$. Thus, when $M < 4$, the G4RM imply $\log_{10} M_0 \sim 2M$, for $4 < M < 6$ $\log_{10} M_0 \sim 1.5M$, and for $M > 7$, $\log_{10} M_0 \sim 1.3M$. However, for $M < 4$, f_1 and f_2 become comparable to, and for small M, exceed f_p (Fig. 1), and, so, our estimates of W and L (via f_1 and f_2) may not be reliable, and are probably too large for this magnitude range. The larger estimates of $\log_{10} M_0$ than the linear trend implied by 1.5 M + 16 in Fig. 5, for $M < 4$, may not be real, but merely a consequence of the natural low-pass filtering the spectra of recorded motions by low Q. Many small magnitude ($M < 3.5$) strong motion accelerograms must be recorded near or at the source (e.g. $\Delta < 10$ km) to interpret the trends of $\log_{10} M_0$, f_1 and f_2 versus M in this magnitude range.

Eqs. (21) and (27) imply that $C_s \sim 1/R$, while the amplitudes of FS_{FF}, computed from $FS(T)$ at $T(N_c)$, attenuate like $\Delta^{A_0(T)}$ (see Eq. 2). However, C_s is computed from Eq. (22) at different cut-off periods $T(N_c)$, and so it depends on magnitude directly through $FS(T)$ and indirectly through W and L (i.e. τ). To verify that $C_s \sim 1/R$ and that Eq. (21) indeed results in M_0 which is independent of R, we computed $\log_{10} M_0$ versus M for R in the range from 0 to 200 km. For $50 < R < 150$ km, the results were insensitive to R. For the cases considered, near $R = 200$ km, Eq. (28) underestimated

$\log_{10} M_0$ by about .2 moment units on the logarithmic scale. For $R < 50$ km, $FS(T)$ in Eq. (1) begins to be sensitive to the near-field effects, and Eq. (28) ceases to apply.

Transition Between Near Field and Far-Field Spectra

To provide a continuous transition between $\Omega_{NF}(\omega)$ and $\Omega_{FF}(\omega)$ and complete a representation for use in engineering applications, we use the results of Jovanovich et al. (1974a,b). They show that the error in representing the static displacement field by a point source is typically less than 5 percent at distances greater than $4L$, where L is the source length. We define the distance S_1, between the station and the "top" of the vertical fault with "dimension" S (see Eqs. (3) and (4), and Gusev, 1983) and at depth H as

$$S_1 = \begin{cases} [R^2 + (H - S)^2]^{1/2} & , \quad H \geq S \\ R & , \quad H < S \end{cases} \tag{29}$$

We use $S = .01 \times 10^{.5M}$ when $S \leq 30$ km, and $S = 30$ km for larger events, and then combine $FS_{NF}(T)$ and $FS_{FF}(T)$ as follows

$$FS(T) = FS_{NF}(T) e^{-\left(\frac{3S_1}{4S}\right)} + FS_{FF}(T) \left(1 - e^{-\left(\frac{3S_1}{4S}\right)}\right), \quad T > T(N_c). \tag{30}$$

In the above expression, 3/4 is used to scale S_1/S so that when $S_1/S = 4$, the exponent is equal to 3, (so that $e^{-3} \sim 0.05$), in agreement with the recommendation of Jovanovich et al. (1974a,b). For $T < T(N_c)$ (see Table II), we use equations of the type illustrated by Eq. (1), depending on which of the G4RM is used.

For $f < f_{co} (= 1/T(N_c))$, Fig. 1 (the heavy solid lines) shows $FS(T)$ computed from Eq. (30). For $R = 10$ km, $H = 0$ and $M = 4$ (bottom heavy solid line), since S_1 and Δ are both greater than $4S$, $FS_{FF}(T)$ contributes mainly to $FS(T)$, and so $FS(T) \sim 1/T^2$. For $M > 7$, S_1 and Δ are smaller than $4S$, and the amplitudes of $FS(T)$ shown in Fig. 1 are dominated by the flat portion of $FS(T) \sim d_p/\tau$ (see Eq. (13)), for T near and longer than $1/f_1$. For $M = 5$ and 6, the spectra, $FS(T)$, display progressively changing slope for $f < f_1$. With increasing M (increasing S), this slope decreases from -2 towards 0, as M goes from 4 to 7 and 8, in the period range shown in Fig. 1.

II.5 COMPARISON OF VARIOUS SOURCE PARAMETERS WITH PREVIOUS DATA AND INTERPRETATION

The selection of $T(N_c)$, where the empirical (Eq. (1)) and extrapolation equations (Eq. (30)) meet, and the assumed dependence of W and L on magnitude define the near-field and the far-field long period Fourier spectral amplitudes of strong motion as outlined in the above Eqs. (13) and (26). These equations, in turn, imply a number of other source characteristics, which can be compared with other independent estimates and with other observations. In the following, we show some of these comparisons, to

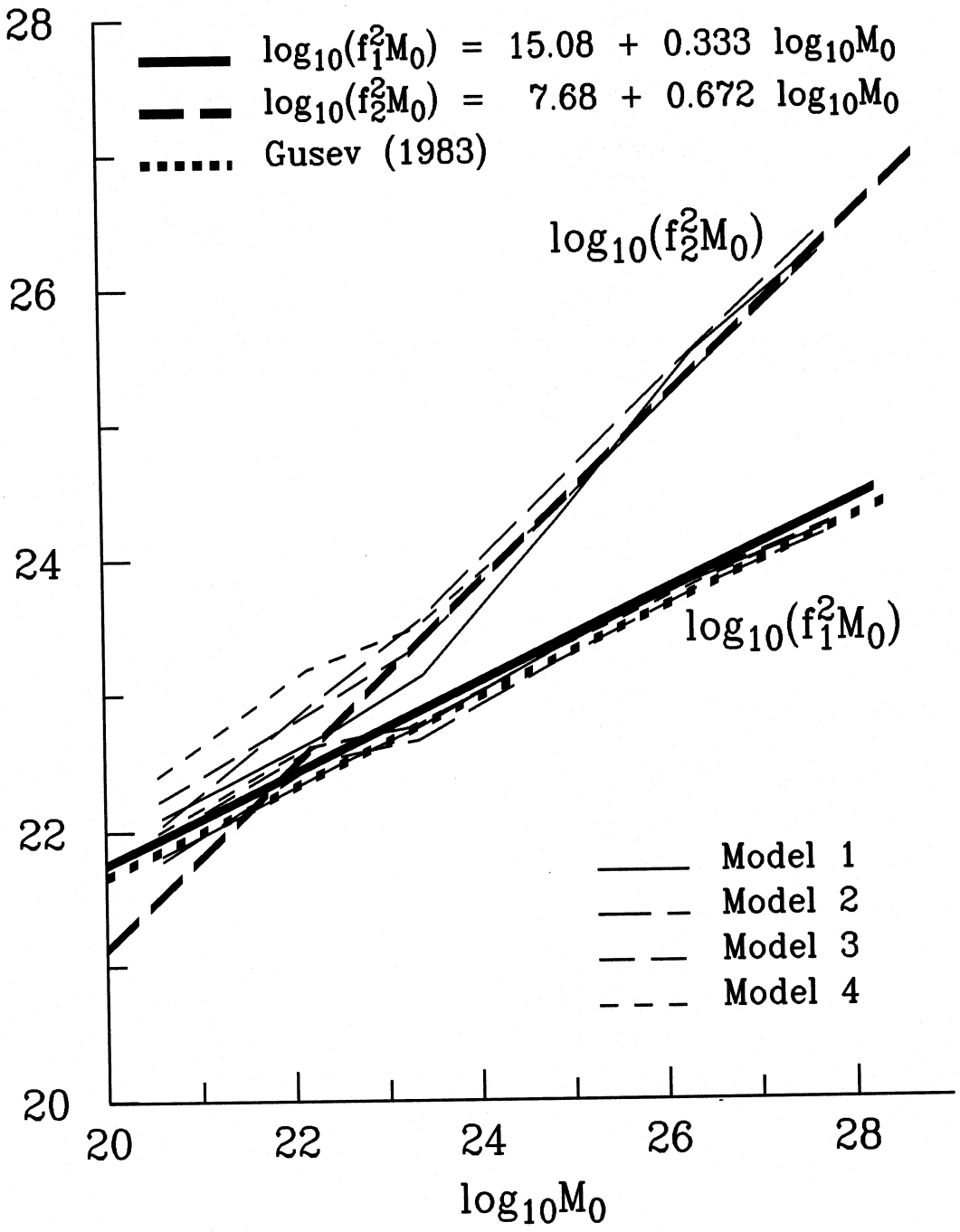

Fig. 6 $\log_{10} f_1^2 M_0$ and $\log_{10} f_2^2 M_0$ versus $\log_{10} M_0$.

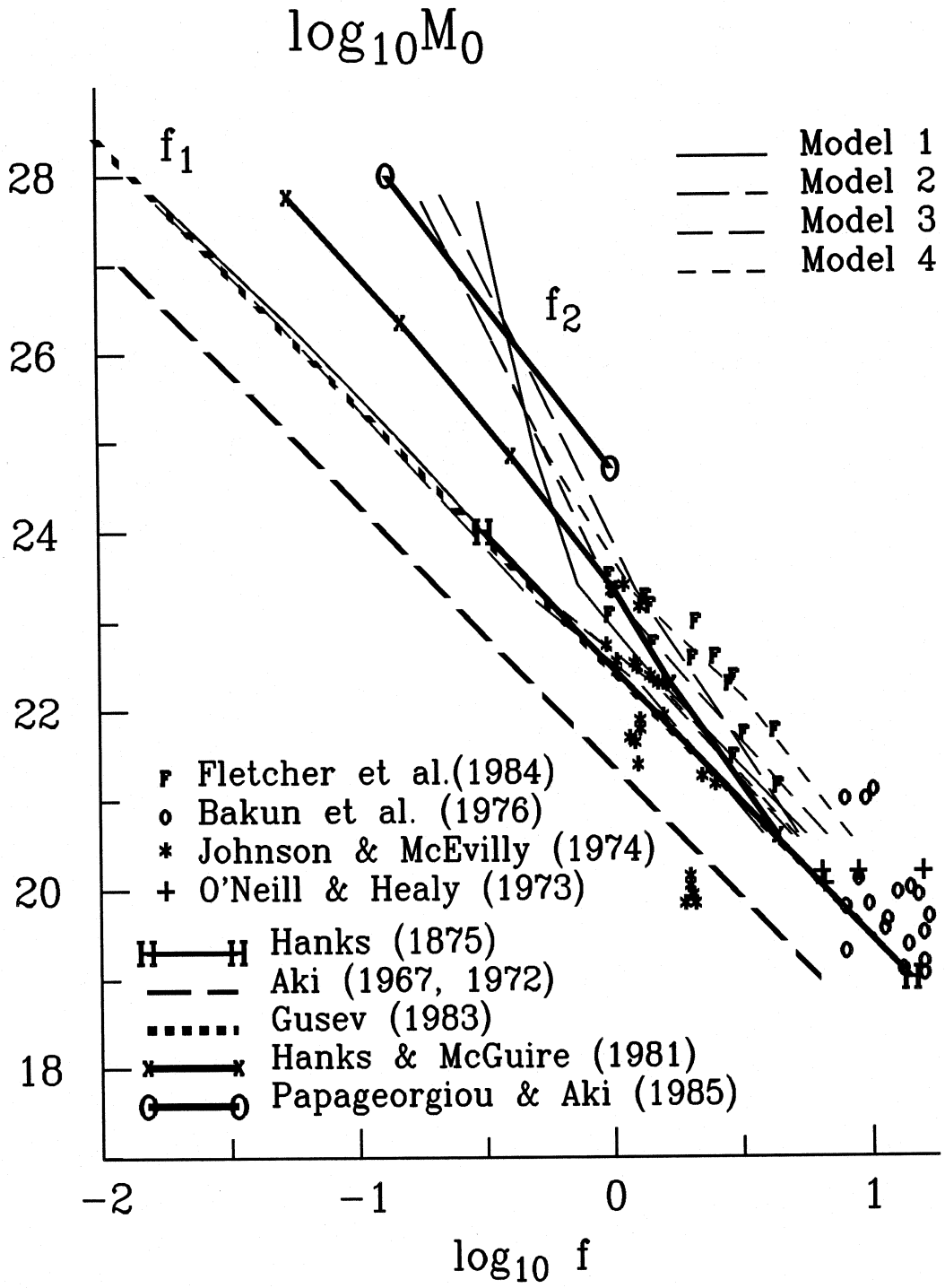

Fig. 7 $\log_{10} M_0$ versus $\log_{10} f_1$ and $\log_{10} f_2$ (after Chouet et al. 1978).

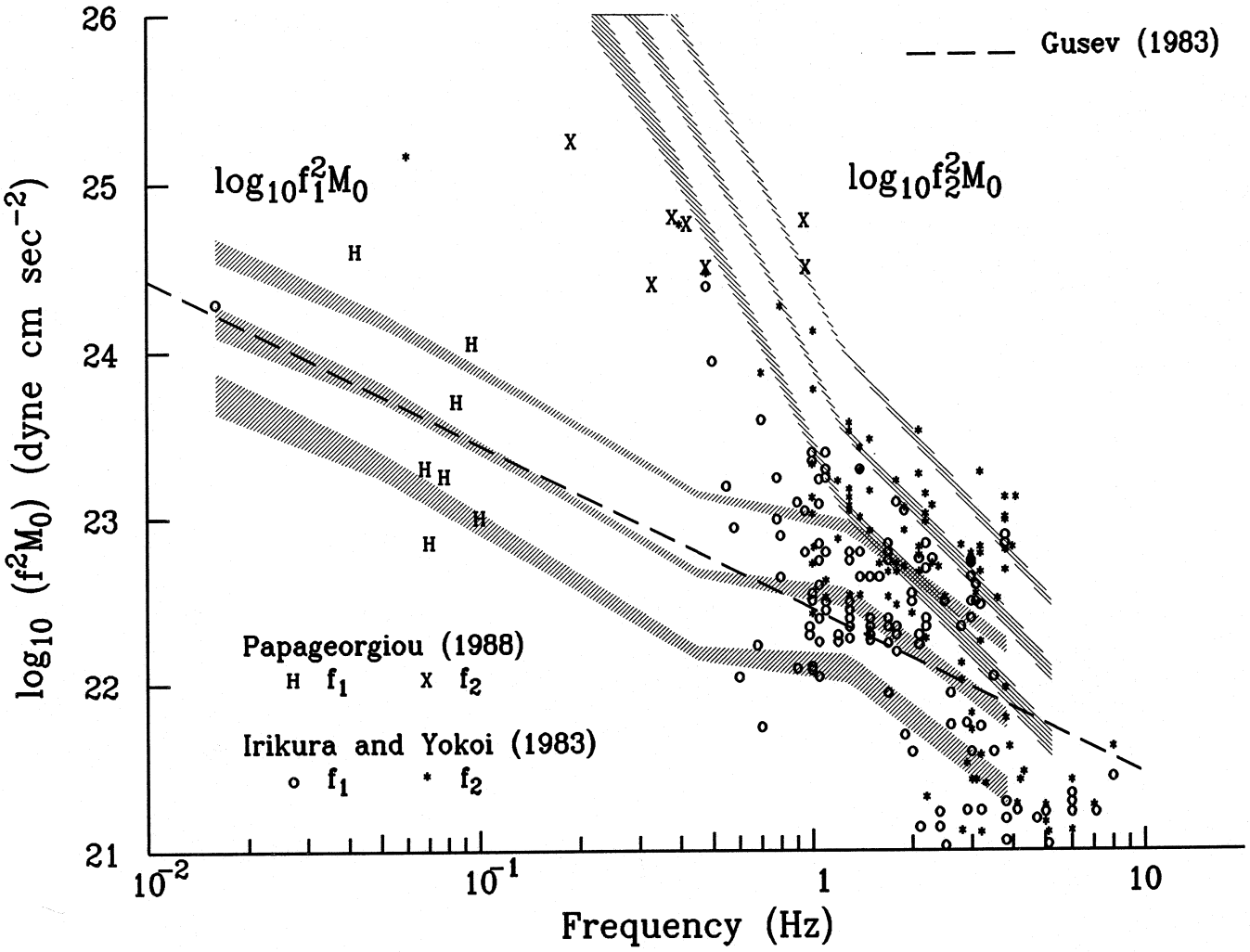

Fig. 8 $\log_{10} f^2 M_0$ versus f with data from Papageorgiou (1988) and Model 1 (Table IV). The three shaded bands correspond to probabilities of exceedance equal to 0.1, 0.5 and 0.9 and for the G4RM.

test the suitability of the chosen functional forms of the Eqs. (13) and (26), of their scaling parameters, and of our overall extrapolation method.

Corner Frequencies f_1 and f_2

Fig. 6 shows $\log_{10} f_1^2 M_0$ and $\log_{10} f_2^2 M_0$ plotted versus $\log_{10} M_0$ for the four fault models. Those can be approximated by the linear trends

$$\log_{10} f_1^2 M_0 = 15.1 + \frac{1}{3} \log_{10} M_0 \tag{31}$$

$$\log_{10} f_2^2 M_0 = 7.7 + \frac{2}{3} \log_{10} M_0, \qquad \log_{10} M_0 > 23. \tag{32}$$

For small M_0, f_1 and f_2 are nearly the same. Near $\log_{10} M_0 \sim 20$, f_2 slowly becomes larger than f_1, and after a transition region, $20 < \log_{10} M_0 < 23$, $\log_{10} f_2^2 M_0$ attains its own trend as in the above Eq. (32). The trend of $\log_{10} f_1^2 M_0$ as used by Gusev (1983) is also shown, and agrees well with our results.

In terms of L, W, f_1 and f_2 for the four fault models in Table IV, and recalling that $\log_{10} M_0 \sim 1.5 M_s + 11.8 - \log_{10}(\eta\bar{\sigma}/\mu)$, and that $\eta\bar{\sigma}$ is the apparent stress, it can be shown that our results imply $\eta\bar{\sigma} = 10$ to 20 bars for the average trends, and for $\log_{10} M_0 > 23$.

Fig. 7 compares our results on $\log_{10} M_0$ versus $\log_{10} f_1$ and $\log_{10} f_2$ with the analysis of Chouet et al. (1978). It is seen that our curves for the extrapolation models 1 through 4, for f_2 and f_1 agree well with the observed corner frequencies, with the corresponding trends for f_1 of Hanks (1975) and Gusev (1983), and with f_2 from Papageorgiou and Aki (1985). For $\log_{10} M_0 < 19$, the observed corner frequencies in Fig. 24 of Chouet et al. (1978) cease to increase with frequency, apparently due to the low-pass filtering effects of the attenuation. The corner frequency of Hanks and McGuire (1981) is close to our $\log_{10} f_2$ for $\log_{10} M_0 < 25$, and then is roughly in the middle between our $\log_{10} f_1$ and $\log_{10} f_2$ for $\log_{10} M_0 > 25$.

Another way of combining the data on f_1, f_2 and M_0 is to plot $\log_{10} f^2 M_0$ versus f. Fig. 8 shows an example (fault model 1 in Table IV) of our estimates of $f_1^2 M_0$ and $f_2^2 M_0$ versus f, and compares those with the data used by Papageorgiou (1988). In making this comparison, we do not attempt to establish what is the physical meaning of f_2. We only recognize that such a corner frequency is observed by some investigators (Irikura and Yokoi, 1983; Papageorgiou and Aki 1983) and that it is not difficult to associate it with $f_2 \sim 2.2/W$. The fault models 2, 3 and 4 result in very similar trends, and agree equally well with the data on f_1, f_2 and M_0.

Similarity

For similarity to exist among different earthquake events, the dimensional analysis of the static and of the dynamic parameters, describing the gross features of source mechanism and of the static field after an earthquake require that: 1) $W/L = \text{const.}$, 2) $\overline{u}/W = \text{const.}$, and 3) $v/\beta = \text{const.}$ For constant stress drop, and if conditions 1) and 2) hold, then 3) is equivalent to $vT_0/L = \text{const.}$ For a set of earthquakes occurring in very different tectonic environments, Geller (1976) has found W/L to be relatively stable, with value near 0.5. Works of Thatcher and Hanks (1973) and Kanamori and Anderson (1975) imply that the strain drop (i.e. $\overline{u}/W$) is relatively stable, and, with typical values of stress drop between 30 and 50 bars, imply strain drop of the order to 10^{-4}. Though only a small number of detailed source mechanism studies can be used to determine v/β (Archuleta, 1982; Harzel and Helmberger, 1982; Harzel and Heaton, 1983; Jordanovski et al., 1986; Olson and Apsel, 1982; Trifunac, 1974; Trifunac and Udwadia, 1974), this ratio is near 0.6. Gusev (1983) interprets these observations to imply that the similarity hypothesis can be accepted for large earthquakes. We note however, that both Geller (1976) and Kanamori and Anderson (1975) treat a very broad collection of sources from different parts of the world and including both intra-plate and inter-plate events.

In earthquake engineering applications, one is interested in the similarity aspect in a more localized and regional sense, to the extent that it may influence the estimation of strong shaking from the sources typically not further than 200 - 300 km from the site. Thus, unless one is dealing with a site which is close both to a large subduction zone and to the local shallow thrust and strike slip faults simultaneously (e.g. Alaska, east coast of Japan e.t.c.), it may be appropriate to consider only a more restricted subset of contributing events, for example strike slip and thrust faults in southern California. In this paper, we can consider such events only because the strong motion data used to develop the G4RM is all recorded in this area. Therefore, in the following, we address the question of the source similarity for such events only.

Figs. 9 and 10 show the variation of W/L and of $\log_{10}(\overline{u}/L)$ plotted versus magnitude for the four fault models (Table IV). The nature of the assumed dependence of L and of W on M, for these four models, obviously does not satisfy the first two similarity requirements. Fig. 11, which considers 2.2 T_0/L, shows minor fluctuations of this ratio for the three fault models and nearly a constant value for Model 1.

Assuming that the dislocation grows linearly with time as in $\frac{\sigma\beta}{\mu}t$ (Brune, 1970), until it reaches the final dislocation $\overline{u} = 2\overline{d}$, we can assume that the rise time T_0 is

$$T_0 \sim \frac{\overline{u}\mu}{\sigma\beta}. \tag{33}$$

Also,

$$\overline{u} = C_0\frac{r\sigma}{\mu}, \tag{34}$$

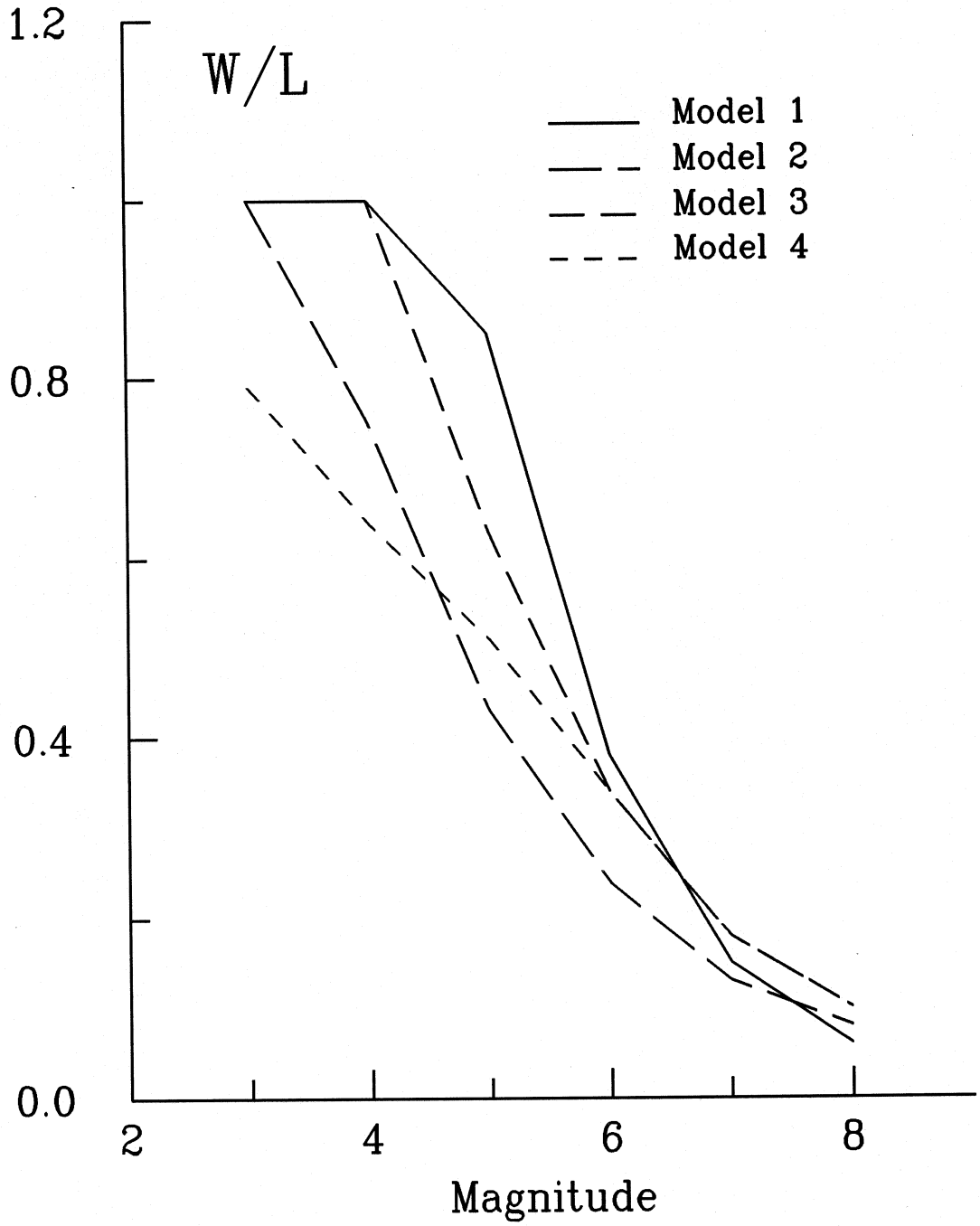

Fig. 9 W/L (fault width/fault length) versus magnitude for Models 1 through 4 (Table IV).

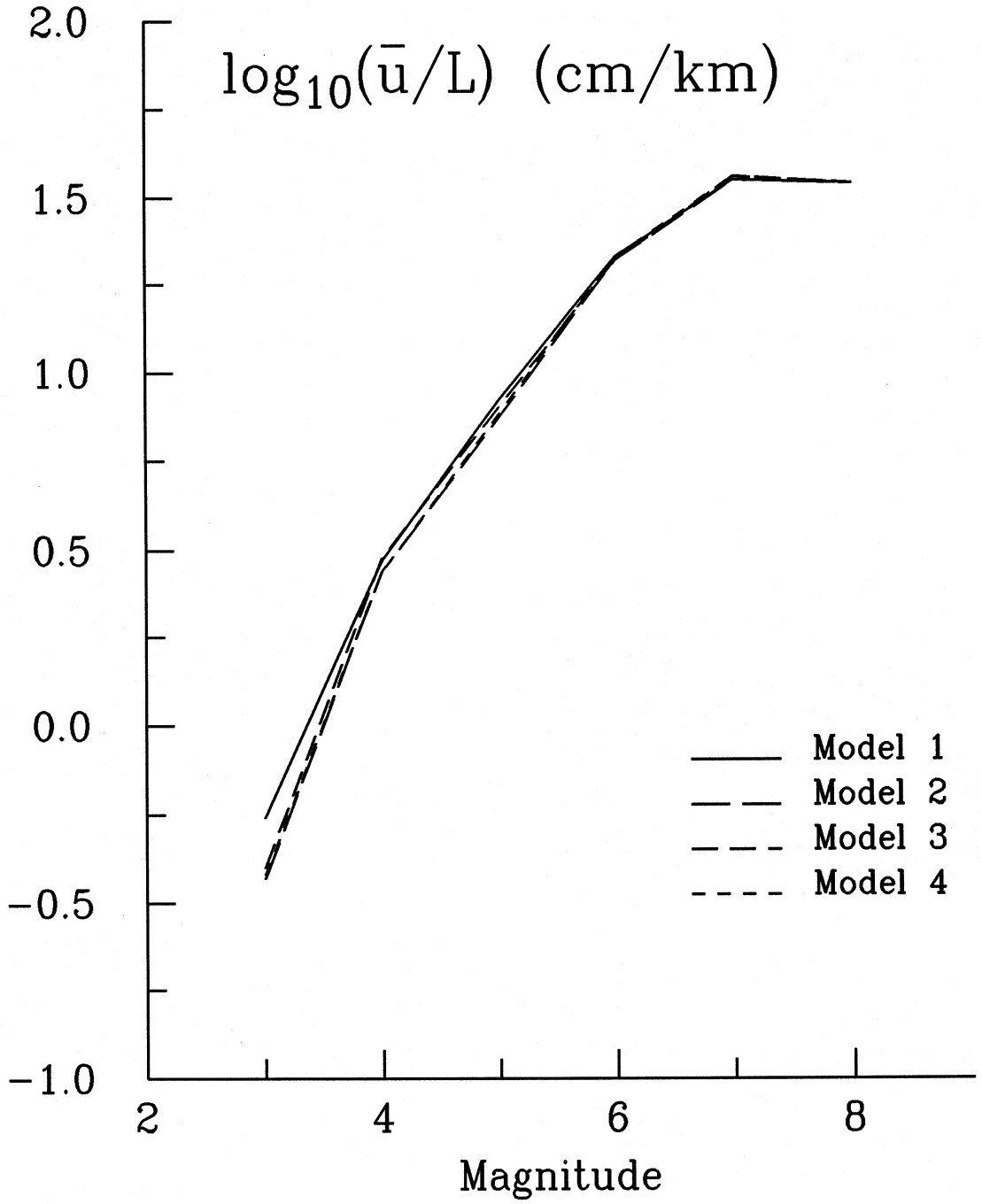

Fig. 10 $\log_{10}(\overline{u}/L)$ (average dislocation/fault length) versus magnitude for Models 1 through 4 (Table IV).

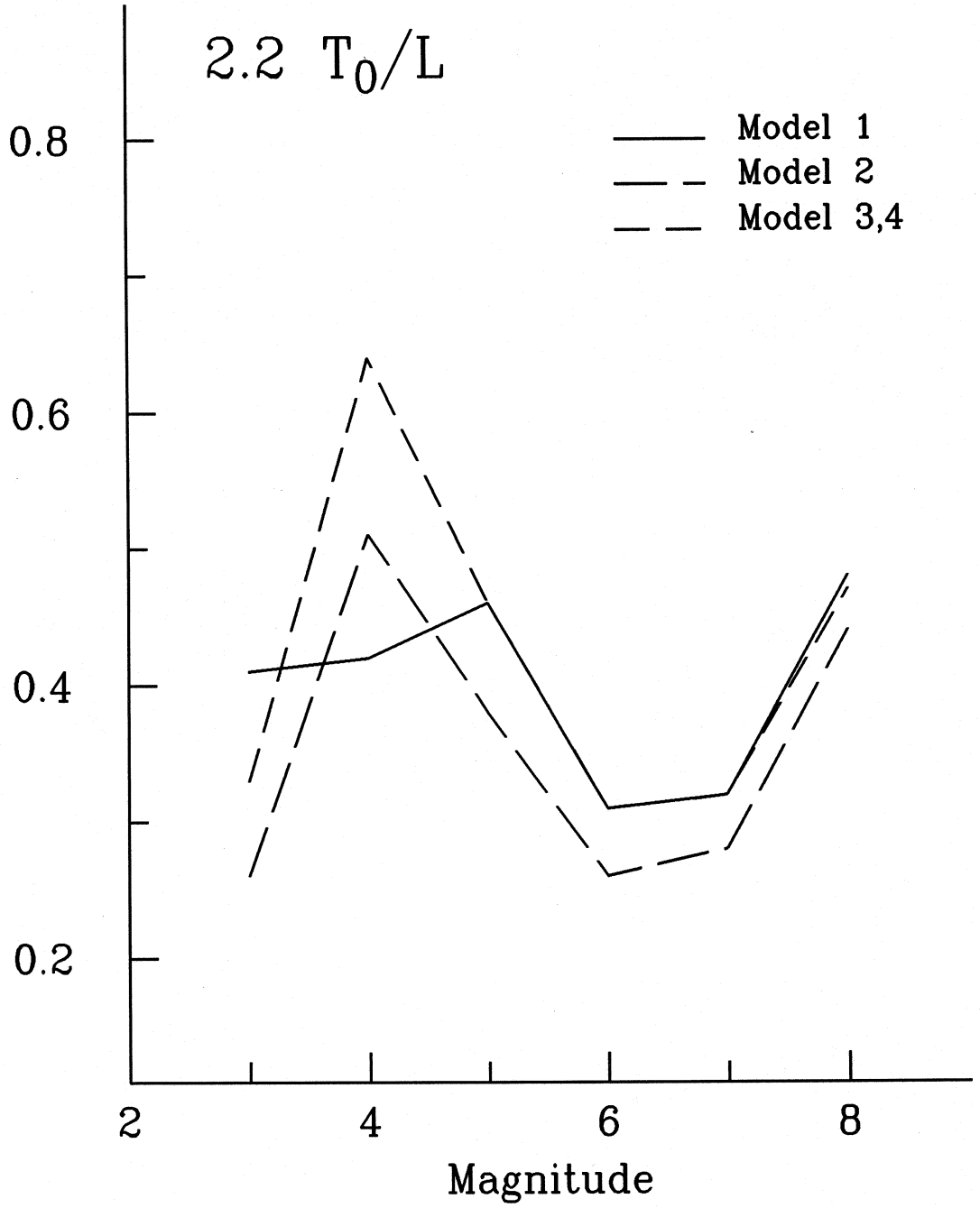

Fig. 11 2.2 T_0/L versus magnitude (T_0 is the dislocation rise time and L is the fault length).

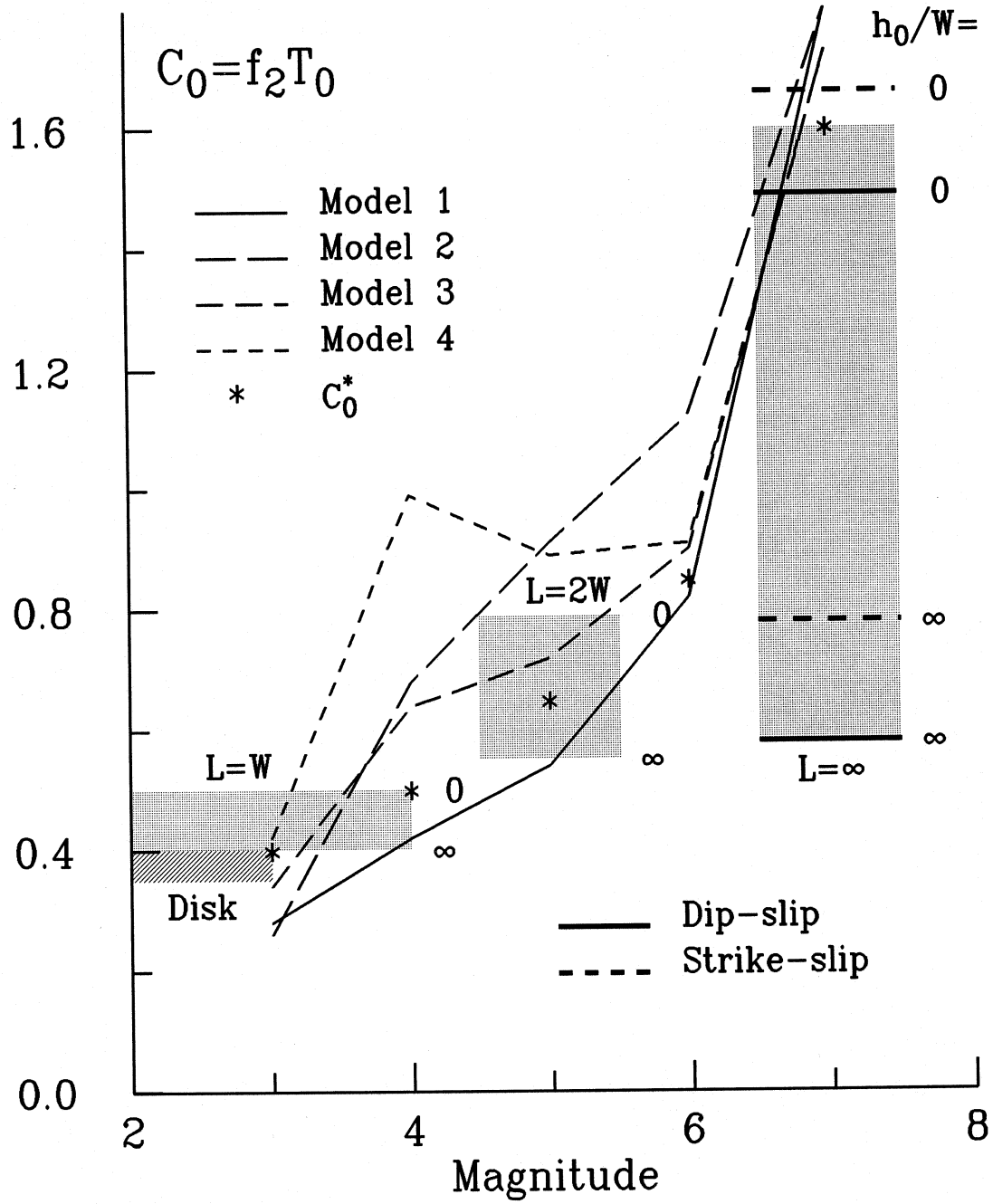

Fig. 12 f_2T_0 versus magnitude for Models 1 through 4. Shaded areas illustrate the range of C_0 derived from analytical (disk) and numerical analyses of static displacements around a rectangular fault (W = width, L = length) and at depth h_0 ($h_0 = 0$ for a surface fault, $h_0 = \infty$ for a fault in elastic full space). C_0 from theoretical solution for infinitely long faults are shown with solid and dashed lines. C_0^* represents the smoothed trend through the data and the numerical and analytical analyses (Table III).

where C_0 and r are given in Table III, for different fault geometries. Since $u_{max} \sim \frac{3}{4}\overline{u}$ on ground surface,

$$T_0 \sim \frac{4}{3} C_0 \frac{r}{\beta} \sim C_0 \frac{r}{v}. \tag{35}$$

From Table III, $r \sim W$ (assuming unilateral faults) and, since we assume $f_2 \sim 2.2/W$, it follows that

$$f_2 T_0 \sim C_0. \tag{36}$$

Fig. 12 shows $C_0 = f_2 T_0$ plotted versus magnitude for the four extrapolation models. Here we used the average T_0 computed from the average of the G4RM, for 50 percent probability of exceedance and for $\mu/\beta \sim .3 \times 10^{16}$ dyne sec /cm^3. For small magnitudes (small faults), C_0 computed from Eq. (36) is very close to C_0 from Table III for circular (and for elliptic) faults. With increasing magnitude, C_0 increases, and for $6 < M < 7$, is in the range $\frac{3}{4} < C_0 < 2$. The limits of this range correspond to dip-slip and to strike-slip faulting on "long" faults (Table III). For $M > 7$, Eq. (36) predicts $C_0 > 2$. This is outside the range for which strong motion data is currently available, and where the multiplicity of sources and other complications contribute to the erratic behavior of v, so that our simplified representation may cease to apply there. Between magnitudes 3 and 7, the average trend of C_0 can be represented by C_0^* (Table VI), which is also plotted in Fig. 12.

Fig. 12 suggests that our data and the models are consistent with more or less "circular" faults for M smaller than about 4, gradually changing to thrust and dip-slip faulting as L and $W \rightarrow 5$ to 10 km, and as L begins to exceed W. Then, as W becomes constrained by the width of the seismogenic zone, our typical event "looks" like a strike-slip fault for which $C_0 \geq 1.6$. This continuously changing C_0^* thus implies that the dynamic similarity requirement, expressed via W ($vT_0/W \sim f_2 T_0 = \text{const.}$) is not satisfied.

Fig. 13 shows $f_1 T_0$ plotted versus magnitude. Fig. 11 showed 2.2 T_0/L, versus magnitude. It is seen that both results could be interpreted to imply that $f_1 T_0 \sim$ const., and 2.2 $T_0/v \sim$ const. Since the strong motion accelerographs can sample only local aspects of strong motion, becoming less sensitive to distant (say > 100 km) contributions from large dislocation amplitudes and stress drops (faulting on very long faults with large M and small f_1), it is not possible to extrapolate the above results and consider that this will apply also and directly to teleseismic observations. More detailed interpretation of the "high-pass" filtering of the observed strong motion in long periods, by the whole process of strong motion recording and analysis, must be performed before deciding how much and how this contributes towards apparent similarity ($f_1 T_0 \sim$ const.) of large earthquakes, and above which wave length resolution this may apply.

Characteristic Source Durations T_0 and τ

Assuming that the time rate of growth of the dislocation amplitudes is proportional to the effective stress drop (Brune, 1970), and that the multiple events are excluded from

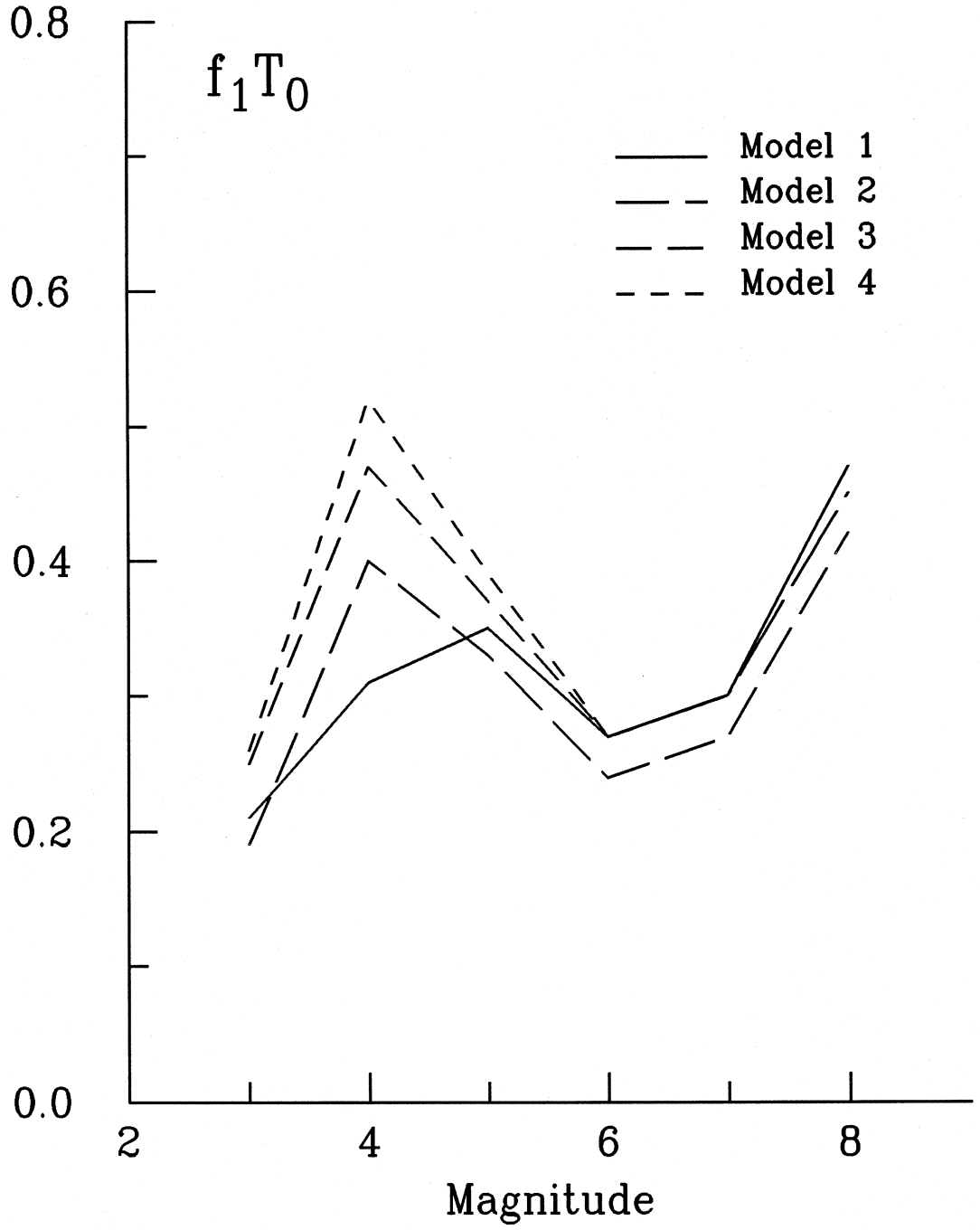

Fig. 13 f_1T_0 versus magnitude for Models 1 through 4.

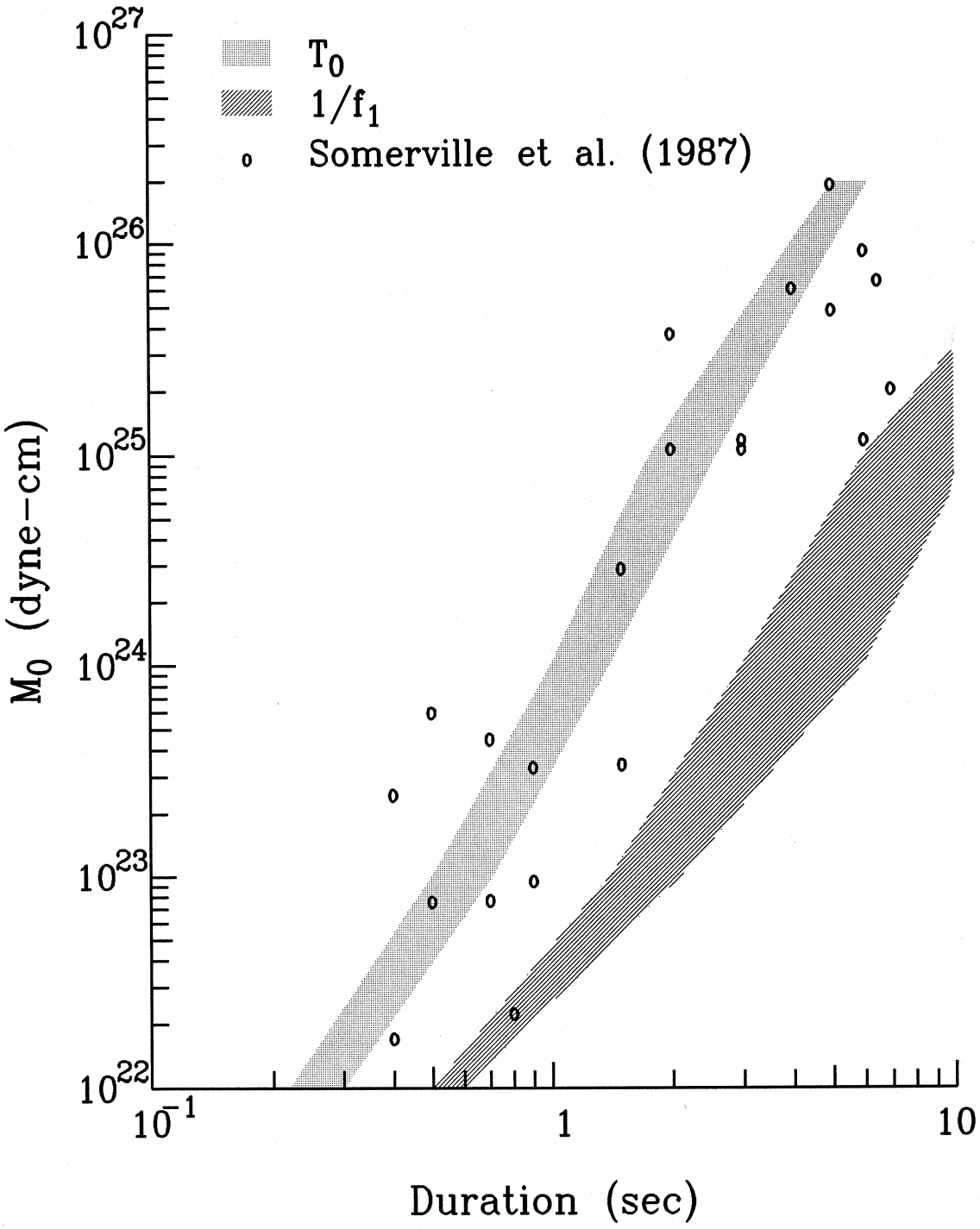

Fig. 14 Comparison of T_0 (the dislocation rise time) and $\tau = 1/f_1$ (the duration of faulting) with the teleseismic estimates of source duration by Somerville et al. (1987). The two gray zones for T_0 and $\tau = 1/f_1$ illustrate the range of values for the four faulting models and for the G4RM.

this consideration, the dislocation rise time T_0 can be estimated from Eq. (33). This should also be related to the time it takes for the dislocation to propagate through the full fault width W, and since $W \sim 1/f_2$, $f_2 T_0$ should be nearly constant (Eq. 36), perhaps only slowly changing with magnitude (i.e. the fault geometry, Fig. 12). Thus, in terms of the overall source duration characteristics (integrating over the high frequency pulses that may result from asperities and fault barriers), T_0 can be viewed as the shortest overall characteristic duration of the source. On the other hand, $\tau = \frac{L}{v} + T_0$ can be viewed as the longest characteristic source duration, where v can be chosen so that it incorporates the delays between the multiple rupture events, when those do occur in the corresponding frequency and wave length domains.

Fig. 14 shows the trends of the durations T_0 and $\tau = 1/f_1$ versus seismic moment M_0 for the G4RM studied here. For comparison, it shows also the data on source duration compiled by Somerville et al. (1987). Their source durations were estimated from the duration of triangular or trapezoidal source functions, which provided the best fit to the teleseismic long and short period body waves. Their data contains 22 events which were recorded in California between 1933 and 1983 and which coincide with most of the events contributing to our strong motion data base used in this work. The method of Somerville et al. (1987) should give reasonable estimates of source duration for simple events (corresponding to T_0), but it will underestimate the source duration for multiple rupture or multiple plane events. This seems to be confirmed in Fig. 14 where most points fall around T_0 and between T_0 and $\tau = 1/f_1$, but in most cases do not reach τ.

Fault Area

The fault area, A, is directly related to the estimates of f_1 and f_2, since $W \sim v/f_2$ and $L \sim v/\left[f_1\left(1 + \frac{W}{2.7L}\right)\right]$, giving

$$A = [v^2/(f_1 f_2)]\left(1 + \frac{W}{2.7L}\right)^{-1}. \tag{37}$$

Using the approximations for $L = a10^{bM}$ and $W = c10^{dM}$ gives

$$A = ac10^{(b+d)M} \tag{38}$$

Then, from Table IV, $ac \sim .001$ to $.0017$ and $(b+d) \sim .74$ to $.77$. For large events ($M > M_*$), Table IV thus implies

$$\log_{10} A \approx \frac{1}{2}\log_{10} M_0 - 11 \quad , \quad M_0 > 10^{23} \tag{39}$$

assuming that $\log_{10} M_0 \sim 1.45M + 16$ (Wyss and Brune, 1968), and that $M_0 > 10^{23}$. For $M < M_*$, $ac \sim .0001$ and $b + d \sim 1$, giving

$$\log_{10} A \approx \frac{2}{3}\log_{10} M_0 - 14.8 \quad , \quad M_0 < 10^{23}. \tag{40}$$

Table VI

Average rise time T_0^* in seconds and average C_0^*, versus magnitude

M	T_0(sec)	C_0^*
3	.05	.4
4	.31	.5
5	.73	.65
6	1.6	.85
7	5.4	1.6
8	(26.4)	(1.6)

* $\mu/\beta = .3 \times 10^6$ dyne sec/cm^3

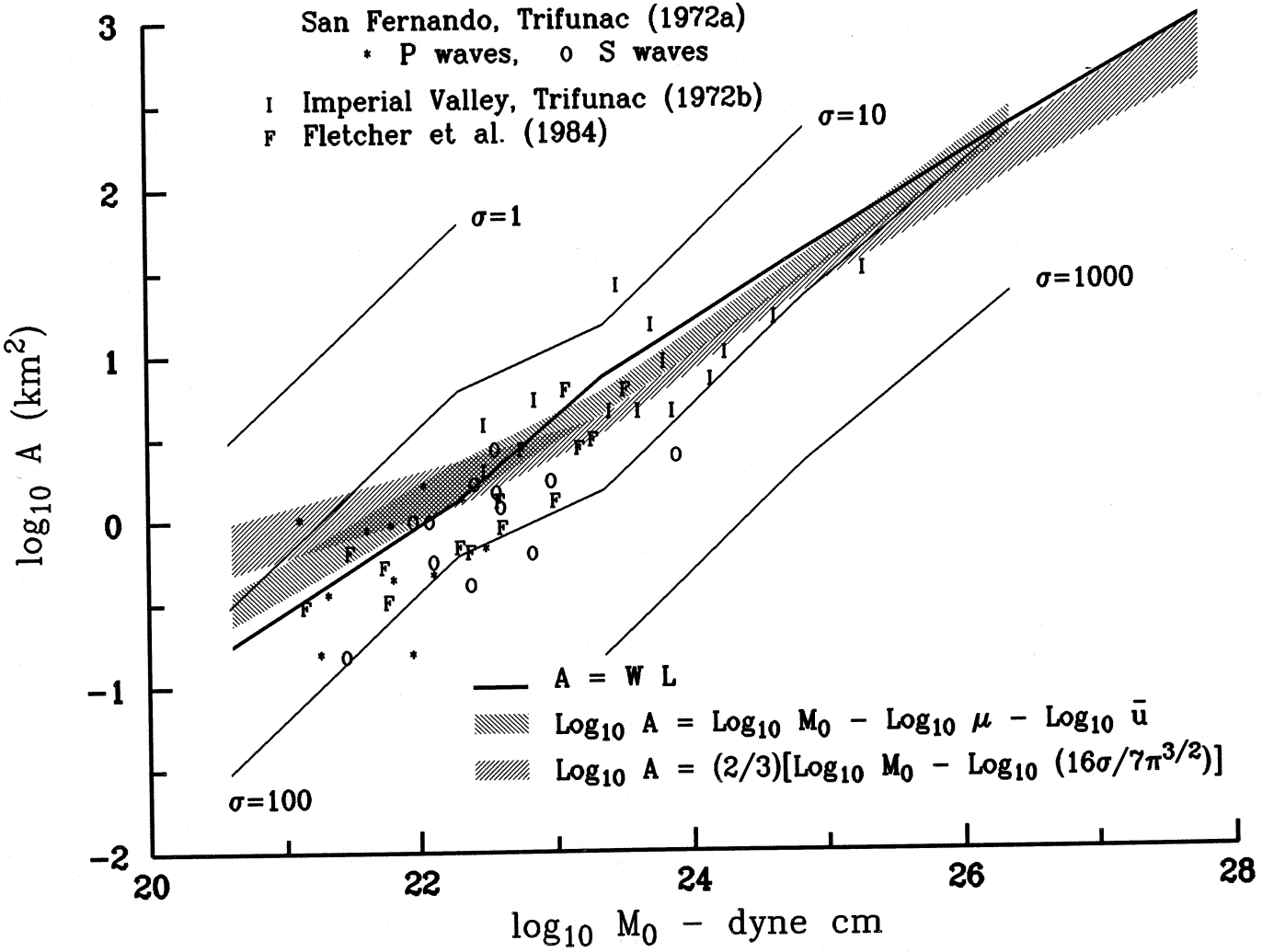

Fig. 15 $\log_{10} A$ versus $\log_{10} M_0$, comparing the estimates of $\log_{10} A$ using Eqs. (38), (42) and (41), and selected estimates based on spectra of strong motion acceleration. $\log_{10} A_0$ for constant stress drop (σ = 1, 10, 100 and 1000 bars) using Eq. (43) are also shown.

Thus, our four fault models result in slope of $\log_{10} A$ versus $\log_{10} M_0$ equal to $\sim 2/3$ for $M < M_*$, and to $\sim 1/2$ for $M > M_*$. We note that the equation $\log_{10} M_0 = \frac{3}{2} \log_{10} A + 22.25$, for $10^{25} < M_0 < 10^{30}$, used by Purcaru and Berckhemer (1982) would be identical to Eq. (40) if extrapolated to $M < 10^{25}$. This remarkably constant slope, equal to 2/3, for the entire range $10^{21} < M < 10^{30}$ implies $\log_{10} \mu\overline{u} \sim$ constant.

Starting with the definition of seismic moment $M_0 = \mu A \overline{u}$ and representing $\overline{u} \sim C_0^* \frac{W\sigma}{\mu}$ gives

$$\log_{10} A = \log_{10} M_0 - \log_{10} C_0^* W \sigma. \tag{41}$$

An advantage of this expression is that it eliminates μ and can be used to test the internal consistency of various estimates when μ is not known. Using averages from the four fault models to compute C_0^* (Table VI), $\overline{\log_{10} W}$ and $\overline{\log_{10} M_0}$, a family of curves representing Eq. (41) can be shown in Fig. 15, for $\sigma = 1$, 10, 100 and 1000 bars. More directly, $M_0 = \mu \overline{u} A$ gives

$$\log_{10} A = \log_{10} M_0 - \log_{10} \mu - \log_{10} \overline{u}. \tag{42}$$

In Eq. (42), $\log_{10} \overline{u}$ can be computed from the long period estimates of spectral amplitudes (Eq. (13) and Fig. 4) in the near field, and $\log_{10} M_0$ can be determined from the long period spectra of the far field motion (Eq. (21) and Fig. 5). For the fault model 2 as an example, and for the range of amplitudes computed from the G4RM, Eq. (42) is shown in Fig. 15 by one of the shaded zones.

For a circular fault and known stress drop, $\log_{10} A$ can also be written as

$$\log_{10} A = \frac{2}{3} \left[\log_{10} M_0 - \log_{10} \frac{16}{7\pi^{3/2}} \sigma \right]. \tag{43}$$

Using the average stress drop for the G4RM results in the second shaded region shown in Fig. 15. The slope of this equation, 2/3, is consistent with that of Eq. (40) for $M < M_*$, while $W \sim L$ for the four fault models (Table IV). This slope is apparently maintained as long as W and L are approximately the same, even for the largest faults on the subduction zones (e.g. Chile, Alaska, Kanamori and Anderson, 1975). In contrast, for the strong motion data in California, where W is limited by the width of the seismogenic zone, for magnitudes near M_*, this slope reduces to 1/2.

Fig. 15 presents also examples of $\log_{10} A$, assuming circular dislocation and based on the spectral analysis of strong motion accelerograms (Trifunac 1972a,b; Fletcher et al., 1984). It is seen that $A = WL$ (the solid continuous curve in Fig. 15) is close to this data, but may overestimate A for $M < 10^{23}$. For $M_0 < 10^{23}$, the data points are also in agreement with $\log_{10} A = .83 \log_{10} M_0 - 18.4$, which is equivalent to $\log_{10} A = 1.21 M_s - 5.05$ in Båth and Duda (1964).

II.6. DISCUSSION AND CONCLUSIONS

This work is based on a simplified description of shear wave spectra. This representation does not evolve from a solution of some specific source slip, but can be thought of as an intuitive collection of relevant parameters and functional relationships based on simple dimensional analysis, which result in a coherent picture of the main features of strong ground motion. The remarkable outcome of this exercise is that the various comparisons of our model with the independent estimates of seismic moment, and average dislocation lead to good agreement, and to resolution and scatter which are consistent with other independent estimates.

The largest uncertainties in our extrapolation exist near $T(N_c)$, where the empirical scaling models approach the recording and processing noise. The tests performed so far suggest that the resulting $FS(T)$ are probably very realistic for $3.5 < M < 7$ and for horizontal ground motion. The slopes and amplitudes of empirically computed $FS(T)$ for vertical motions suggest that near $T = T(N_c)$ our empirical models may not be reliable for $M > 6.5$. To understand these amplitudes, we need more recorded accelerograms for $M > 7$ and, so, we must patiently wait for this data to become available.

Extrapolation of $FS(T)$ on $\log - \log$ scale by Eqs. (13), (26) and (30), from $T(N_c)$ towards $T \rightarrow \infty$ sec appears reasonable and agrees favorably with the known trends of the seismic moment, M_0, and of the average dislocation amplitudes, $\overline{u}$, versus earthquake magnitude. Since the corner frequency, $1/\tau$, in the near field ground motion is $\sim v/r$, where v is the dislocation velocity (typically between 2 and 3 km/sec), and r is the representative source dimension, it is seen that τ can be larger than $T(N_c)$. This is so assuming that, for the frequencies considered here the rupture occurs as a "smooth" process. Many studies have suggested that the fault slips irregularly, with large dislocations distributed at several or at many "hot" spots, with large dislocation amplitudes, making larger events look like a sequence of smaller events. While this faulting behavior can affect τ appreciably, we do not have at present, reliable data to identify such behavior in our analysis.

The highly "local" nature of strong motion recordings, local in the sense of the proximity to the fault (less than say 100 km), and the fact that it is $\overline{u}$ and not the overall source magnitude or moment and the long source dimensions (L) that govern the near field strong motion amplitudes, all agree with the observed trends of strong motion amplitudes predicted by the G4RM.

Numerous further tests and studies of the relationships analogous to Eqs. (13), (26), (30) and (33) (and of the associated amplitudes, corner frequencies and scaling parameters) are possible. Also the empirical equations exemplified by Eq. (1) can be used to investigate the high frequency attenuation and the trends implied by the peaks of spectral amplitudes for frequencies less than 25 Hz. Some of these studies have been completed and are presented in this report, in the following chapters. The picture which emerges from this work is that of detailed internal consistency and agreement with near

strong ground motion and distant seismological inferences on one hand, and with the simplified theoretical source representations on the other.

II.7. REFERENCES

Aki, K. (1967). Scaling Law of Seismic Spectrum, *J. Geoph. Res.*, **72**(4), 1217-1231.

Aki, K. (1972). Scaling Law of Earthquake Source Time Function, *Geophys. J.*, **31**, 3-25.

Amini, A., V.W. Lee and M.D. Trifunac (1982). Noise in Earthquake Accelerograms, *ASCE, EMD*, **108**, 1121-1129.

Anderson, J.G. (1991). Strong Motion Seismology, in Contributions in Seismology, AGU, Washington, D.C.

Archuleta, R.J. (1982). Analysis of Near-Source Static and Dynamic Measurement from the 1979 Imperial Valley Earthquake, *Bull. Seism. Soc. Amer.*, **72**, 1927-1956.

Bakun, W.H. (1984). Seismic Moments, Local Magnitudes, and Coda-Duration Magnitudes for Earthquakes in Central California, *Bull Seism. Soc. Amer.*, **74**(2), 439-458.

Bakun, W.H., C.G. Fuge and R.M. Stewart (1976). Body-Wave Spectra of Central California Earthquakes, *Bull. Seism. Soc. Amer.*, **66**, 363-384.

Båth, M. and S.J. Duda (1964). Earthquake Volume, Fault Plane Area Seismic Energy, Strain, Deformation and Related Quantities, *Ann. Geofis.* (Rome), **17**, 353-368.

Boatwright, J. (1988). The Seismic Radiation from Composite Models of Faulting, *Bull. Seism. Soc. Amer.*, **78**(2), 489-508.

Boore, D.M. (1983). Stochastic Simulation of High-Frequency Ground Motions Based on Seismological Models of the Radiated Spectra, *Bull. Seism. Soc. Amer.*, **73**(6), 1865-1894.

Brune, J.N. (1970). Tectonic Stress and the Spectra of Seismic Shear Waves, *J. Geophys. Res.*, **75**, 4997-5009.

Chinnery, M.A. (1969). Earthquake Magnitude and Source Parameters, *Bull. Seism. Soc. Amer.*, **59**(3), 1969-1982.

Geller, R.J. (1976). Scaling Relations for Earthquake Source Parameters and Magnitudes, *Bull. Seism. Soc. Amer.*, **66**, 1501-1523.

Chouet, B., K. Aki and M. Tsujiura (1978). Regional Variation of the Scalinf Law of Earthquake Source Spectra, *Bull. Seism. Soc. Amer.*, **68**, 49-79.

Fletcher, J., J. Boatwright, L. Haar, T. Hanks and A. McGarr (1984). Source Parameters for Aftershocks of the Oroville, California, Earthquake, *Bull. Seism. Soc. Amer.*, **74**, 1101-1123.

Gusev, A.A. (1983). Descriptive Statistical Model of Earthquake Source Radiation and its Application to an Estimation of Short-Period Strong Motion, *Geophy. J.R. Astr. Soc.*, **74**, 787-808.

Gutenberg, B. and C.F. Richter (1956). Earthquake Magnitude, Intensity, Energy and Acceleration, *Bull. Seism. Soc. Amer.*, **46**, 105-145.

Hanks, T.C. (1982). $f_{\max}$, *Bull. Seism. Soc. Amer.*, **72**(6), 1867-1879.

Hanks, T.C. (1975). Observations and Estimation of Long-Period Strong Ground Motion in the Los Angeles Basin, preprint.

Hanks, T.C. and R.K. McGuire (1981). The Character of High Frequency Strong Ground Motion, *Bull. Seism. Soc. Amer.*, **71**, 2071-2095.

Hasegawa, H.S. (1983). *Lg* Spectra of Local Earthquakes Recorded by the Eastern Canadian Telemetered Network and Spectral Analysis, *Bull. Seism. Soc. Amer.*, **73**(4), 1041-1062.

Haskell, N.A. (1964). Total Energy and Energy Spectral Density of Elastic Wave Radiation from Propagating Faults, *Bull. Seism. Soc. Amer.*, **56**, 1811-1842.

Haskell, N.A. (1969). Elastic Displacement in the Near Field of a Propagating Fault, *Bull. Seism. Soc. Amer.*, **59**(2), 965-980.

Hartzell, S. and D. Helmberger (1982). Strong-Motion Modeling of the Imperial Valley Earthquake of 1979, *Bull. Seism. Soc. Amer.*, **72**(2), 571-596 .

Hartzell, S. and T. Heaton (1983). Inversion of Strong Ground Motion and Teleseismic Wave Form Data for the Fault Rupture History of the 1979 Imperial Valley, California Earthquake, *Bull. Seism. Soc. Amer.*, **73**(6), 1553-1584.

Irikura, K. and T. Yokoi (1984). Scaling Law of Seismic Source Spectra for the After shocks of 1983 Central-Japan-Sea Earthquake, *Abstracts of the Seismological Society of Japan*, No. 1.

Johnson, L.R. and T.V. McErilly (1974). Near Field Observations and Source Parameters of Central California Earthquakes, *Bull. Seism. Soc. Amer.*, **64**, 1855-1886.

Jovanovich, D., M.I. Husseini and M.A. Chinnery (1974a). Elastic Dislocations in a Layered Half Space - I. Basic Theory and Numerical Methods, *Geoph. J.R. Astr. Soc.*, **39**, 205-217.

Jovanovich, D., M.I. Husseini and M.A. Chinnery (1974b). Elastic Dislocation in a Layered Half Space - II. Point Source, *Geoph. J. R. Astr. Soc.*, **39**, 219-239.

Jordanovski, L,R., M.D. Trifunac and V.W. Lee (1986). Investigation of Numerical Methods in Inversion of Earthquake Source Mechanism, Dept. of Civil Eng. Dep. No. 86-02, Univ. of Southern California, Los Angeles, California.

Joyner, W.B. (1984). A Scaling Law for the Spectra of Larger Earthquakes, *Bull. Seism. Soc. Amer.*, **74**(4), 1167-1188.

Kanamori, H. and D.L. Anderson (1975). Theoretical Basis of Some Empirical Relations in Seismology, *Bull. Seism. Soc. Amer.*, **65**, 1073-1095.

Kashefi, I. and M.D. Trifunac (1986). Investigation of Earthquake Response of Simple Bridge Structures, Dept. of Civil Eng. Rep. 86-02, Univ. Southern California, Los Angeles, California.

Keilis-Borok, V.I. (1960). Investigation of the Mechanism of Earthquakes, Sov. Res. Geophys. 4, (Transl. Tr. Geofiz. Inst. 40) Am. Geophys. U. Consultants Bureau, New York.

Kojić, S. and M.D. Trifunac (1991a). Earthquake Stresses in Arch Dams: I - Theory and Antiplane Excitation, *ASCE, EMD*, **117**(3), 535-552.

Kojić, S. and M.D. Trifunac (1991a). Earthquake Stresses in Arch Dams: Excitation by SV,P and Rayleigh Waves, *ASCE, EMD*, **117**(3), 553-574.

Lee, V.W., A. Amini and M.D. Trifunac (1982). Noise in Earthquake Accelerograms, *ASCE, EMD*, **108**, 1121-1129.

Lee, V.W. and M.D. Trifunac (1990). Automatic Digitization and Processing of Accelerograms Using PC, Dept. of Civil Eng., Report No. 90-03, Univ. Southern California, Los Angeles, California.

Nuttli, O.W. (1983). Average Seismic Source Parameter Relation for Mid-Plate Earthquakes, *Bull. Seism. Soc. Amer.*, **73**(2), 519-536.

Olson, A. and R. Apsel (1982). Finite Faults and Inverse Theory with Applications to the 1979 Imperial Valley Earthquake,*Bull. Seism. Soc. Amer.*, **72**, 1969-2002.

O'Neill, M.E., and J.H. Healy (1973). Determination of Source Parameters of Small Earthquakes from P Wave Rise Time, *Bull. Seism. Soc. Amer.*, **63**, 101-104.

Papageorgiou, A.S. (1988). On Two Characteristic Frequencies of Acceleration Spectra: Patch Corner Frequency and $f_{\max}$, *Bull. Seism. Soc. Amer.*, **78**(2), 509-529.

Papageorgiou, A.S. and K. Aki (1983). A Specific Barrier Model for the Quantitative Description of Inhomogeneous Faulting and the Prediction of Strong ground Motion I. Description of the Model, *Bull. Seism. Soc. Amer.*, **73**(3), 693-722.

Papageorgiou, A.S. and K. Aki (1985). Scaling Law of Far-Field Spectra Based on Observed Parameters of the Specific Barrier Model, *Pageoph*, **123**, 353-374.

Purcaru, G. and H. Berckhemer (1982). Quantitative Relations of Seismic Source Parameters and a Classification of Earthquakes, *Tectonophysics*, **84**, 57-128.

Richter, C.F. (1958). Elementary Seismology, Freeman and Co. S. Francisco.

Savage, J.C. (1972). Relation of Corner Frequency to Fault Dimensions, *J. Geoph. Res.*, **77**(20), 3788-3795.

Scholz, C.H. (1982). Scaling Laws for Large Earthquakes: Consequences for Physical Models, *Bull. Seismol. Soc. Amer.*, **72**, 1-14.

Seed, H.G. C. Ugas and J. Lysmer (1976). Site Dependent Spectra for Earthquake Resistant Design, *Bull. Seism. Soc. Amer.*, **66**, 221-243.

Somerville, P.G., J.P. McLaren, L.V. LeFerre, R.W. Burger and D.V. Helmberger (1987), Comparison of Source Scaling Relations of Eastern and Western North American Earthquakes, *Bull. Seism. Soc. Amer.*, **77**, 322-346.

Thatcher, W., and T.C. Hanks (1973). Source Parameters of Southern California Earthquakes, *J. Geoph. Res.*, **78**, 8547-8576.

Trifunac, M.D. (1971). Zero Baseline Correction of Strong-Motion Accelerograms, *Bull. Seism. Soc. Amer.*, **61**, 1201-1211.

Trifunac, M.D. (1972a). Stress Estimates for San Fernando, California Earthquake of February 9, 1971: Main Event and Thirteen Aftershocks, *Bull. Seism. Soc. Amer.*, **62**, 721-750.

Trifunac, M.D. (1972b). Tectonic Stress and Source Mechanism of the Imperial Valley, California Earthquake of 1940, *Bull. Seism. Soc. Amer.*, **62**, 1283-1302.

Trifunac, M.D. (1972c). A Note on Correction of Strong-Motion Accelerograms for Instrument Response, *Bull. Seism. Soc. Amer.*, **62**, 401-409.

Trifunac, M.D. (1973). Analysis of Strong Earthquake Ground Motion for Prediction of Response Spectra, *Int. J. of Earthquake Eng. and Struct. Dynam.*, **2**(1), 59-69.

Trifunac, M.D. (1974). A Three-Dimensional Dislocation Model for the San Fernando, California, Earthquake of February 9, 1971, *Bull. Seism. Soc. Amer.*, **64**, 149-172.

Trifunac, M.D. (1976a). Preliminary Empirical Model for Scaling Fourier Amplitude Spectra of Strong Ground Acceleration in Terms of Earthquake Magnitude, Source to Station Distance and Recording Site Conditions, *Bull. Seism. Soc. Amer.*, **66**, 1343-1373.

Trifunac, M.D. (1976b). Preliminary Analysis of the Peaks of Strong Earthquake Ground Motion-Dependence of Peaks on Earthquake Magnitude, Epicentral Distance and the Recording Site Conditions, *Bull. Seism. Soc. Amer.*, **66**, 189-219.

Trifunac, M.D. (1989a). Dependence of Fourier spectrum Amplitudes of Recorded Strong Earthquake Accelerations on Magnitude, Local Soil Conditions and On Depth of Sediments, *Int. J. Earthquake Eng. and Struct. Dynam.*, **18**, 999-1016.

Trifunac, M.D. (1989b). Empirical Scaling of fourier Spectrum Amplitudes of Recorded Strong Earthquake Accelerations in Terms of Magnitude and Local Soil and Geologic Conditions, *Earthquake Eng. and Eng. Vibration*, **9**(2), 23-44.

Trifunac, M.D. (1990). How to Model Amplification of Strong Earthquake Motions by Local Soil and Geologic Site Conditions, *Int. J. Earthquake Eng. and Struct. Dynam.*, **19**(6), 833-846.

Trifunac, M.D. (1991a). M_L^{SM}, *Int. J. Soil Dyn. and Earthquake Eng.*, **10**(1), 17-25.

Trifunac, M.D. (1991b). A Note on the Differences in Magnitudes Estimated from Strong Motion Data and from Wood-Anderson Seismometer, *Int. J. Soil Dynamics and Earthquake Eng.*, **10**(8), 423-428.

Trifunac, M.D. and A.G. Brady (1975). On the Correlation of Seismic Intensity Scales with the Peaks of Recorded Strong Ground Motion, *Bull. Seism. Soc. Amer.*, **65**, 139-162.

Trifunac, M.D. and D.E. Hudson (1970). Laboratory Evaluation and Instrument Corrections of Strong Motion Accelerographs, Earthquake Engineering Research Laboratory, EERL 70-04, California Institute of Technology, Pasadena.

Trifunac, M.D. and V.W. Lee (1985). Preliminary Empirical Model for Scaling Fourier Amplitude Spectra of Strong Ground Acceleration in Terms of Earthquake Magnitude Source to Station Distance, Site Intensity and Recording Site Conditions,

Department of Civil Engineering, Report No. 85-03. University of Southern Calif., Los Angeles, California.

Trifunac, M.D. and V.W. Lee (1987). Direct Empirical scaling of Response Spectral Amplitudes from Various Site and Earthquake Parameters, U.S. Nuclear Regulatory Commission, Report NUREG/CR-4903, Vol 1.

Trifunac, M.D. and V.W. Lee (1989). Empirical Models for Scaling Fourier Amplitude Spectra of Strong Ground Acceleration in Terms of Earthquake Magnitude, Source to Station Distance, Site Intensity and Recording Site Conditions, *Int. J. Soil Dynam. and Earthquake Eng.*, **8**(3), 110-125.

Trifunac, M.D. and V.W. Lee (1990). Frequency Dependent Attenuation of Strong Earthquake Ground Motion, *Int. J. Soil Dynam. and Earthquake Eng.*, **9**(1), 3-15.

Trifunac, M.D. and F.E. Udwadia (1974). Parkfield, California, Earthquake of June 27, 1966: A Three-Dimensional Moving Dislocation, *Bull. Seism. Soc. Amer.*, **64**, 511-533.

Vidal, A. and L. Munguia (1991). Local Magnitude and Source Parameters for Earthquakes in the Peniusular Ranges of Baja California, *Bull. Seism. Soc. Amer.*, **81**((6), 2254-2267.

Wald, D., D.V. Helmberger, and T.H. Heaton (1991). Rupture Model of the 1989 Loma Prieta Earthquake from the Inversion of Strong Motion and Broad Band Teleseismic Data, *Bull. Seism. Soc. Amer.*, **81**, 1540-1572.

Wyss, M. and J.N. Brune (1968). Seismic Moment, Stress and Source Dimensions for Earthquakes in California – Nevada Region, *J. Geophys. Res.*, **73**, 4681-4694.

III STRESSES AND INTERMEDIATE FREQUENCIES OF STRONG MOTION ACCELERATION

In this chapter, we examine the peaks of Fourier amplitude spectra of strong earthquake acceleration, again using a dimensional analysis. We find that the results may be interpreted to imply simple (one patch events) earthquakes for $M \lesssim 5$ and multiple patch events for $M \gtrsim 5$ (~ 10 near $M = 6.5$ and ~ 100 for $M = 8^+$). We also find that the root mean square of peak stress drop on the fault appears to increase with magnitude for $M \lesssim 6$ and then becomes constant, near 100 bars, for $M \gtrsim 6$. For $M > 6$, peak of the Fourier spectral amplitudes then appears to grow because of the greater number of the peaks (patches) from which the sample is taken (~ 100 for $M = 8^+$), i.e. not from the increasing mean of stress amplitudes.

III.1 INTRODUCTION

The study of the Fourier amplitude spectra of strong motion acceleration can be divided into three frequency bands: 1) long period spectral amplitudes, for frequencies below those of the corner frequency $f_1 \sim v/L$ (v is the dislocation velocity and L is the fault length), 2) high frequency spectral amplitudes, for $f > f_H = \frac{Q\beta}{5\Delta}$ (Q is the quality factor, β the shear wave velocity and Δ the hypocentral distance) and 3) intermediate frequency range for $f_1 < f < f_H$. The long period spectral amplitudes are governed by the permanent fault offset $\overline{u}$ in the near field, by the seismic moment M_0 in the far field, and by the fault geometry (fault width W and length L). In the intermediate frequency range and close to f_H, the spectral amplitudes are determined by the stresses on the fault (Brune, 1970). At high frequencies, $f > f_H$, the spectral amplitudes continue to be determined by the stress drop, but the spectral slope is determined by the attenuation and the scattering properties of the geological environment surrounding and between the source an the recording station. Since 1970's, many studies have investigated these frequency bands (Anderson, 1991).

Recently, a family of empirical scaling equations has been presented (Trifunac 1989a,b; Trifunac and Lee, 1989) describing the Fourier spectrum amplitudes for $\sim .1 < f < 25$ Hz. These scaling equations, representing the average trends of strong motion amplitudes near the source (e.g., hypocentral distance $\Delta < 100$ km), offer new and independent basis to compare with and to calibrate other results which are usually based on intermediate and teleseismic distances. The proximity to the source and the high frequency characteristics of strong motion accelerographs offer advantages in the data quality and in the simplicity of propagation modeling, which can be exploited to learn more about the earthquake sources. The purpose of this chapter is to investigate the intermediate frequency Fourier amplitude spectra ($f_1 < f \leq f_H$), and to focus on those aspects of scaling the strong motion amplitudes, which are related to stress drop on the fault plane.

In what follows, we will study these spectral amplitudes for intermediate frequencies near the peak amplitudes of $FS(T)$ at f_p (Fig. 1). Also, all spectra and analyses will be

based on the estimates of strong ground motion at basement rock ($s = 2$, or $h = 0$) and on "rock" soil site ($s_L = 0$). This will eliminate complications introduced by the local site conditions (Trifunac, 1990) and will allow more direct comparison with seismological studies and observations. Finally, we will discuss the results of Eq. (1) for horizontal motions only (v = 0) to further simplify the interpretation of these empirical equations.

III.2 LOW FREQUENCY EXTENSION

To define spectral amplitudes $FS(T)$ for periods longer than $T(N_c)$, we will extrapolate $FS(T)$ in the near field by an equation of the form,

$$FS_{NF}(T) = \frac{\frac{2\pi}{T}\bar{d}}{\left[\left(\frac{2\pi\tau}{T}\right)^2 + 1\right]^{1/2}}, \tag{44}$$

where $\bar{d}$ is the average permanent ground displacement, $\bar{d} = \bar{u}/2$, at the fault, on the ground surface. $\bar{u}$ is the dislocation amplitude averaged over the fault surface A, and τ is the characteristic source time ($\tau = 1/f_1$). We will approximate τ by

$$\tau \sim \left(\frac{L}{v} + \frac{W}{6}\right) \tag{45}$$

where v is the dislocation velocity ($\sim$ 2.2 km/sec), and will choose $\bar{d}$ such that $FS_{NF}(T)$ is equal to $FS(T)$ computed from Eq. (1) for G4RM at $T(N_c)$ (Table II). This will result in estimates of $\bar{u}$ versus earthquake magnitude which will be used throughout this chapter, typically for $p = 0.5$ (in Eq. (7)).

In the far field, we will extrapolate $FS(T)$ for $T > T(N_c)$ by

$$FS_{FF}(T) = C_s \left(\frac{2\pi}{T}\right)^2 \frac{1}{\left[1 + \left(\frac{W}{2.2T}\right)^2\right]^{1/2}} \cdot \frac{1}{1 + \frac{\tau}{T}} \tag{46}$$

where C_s will be computed such that $FS_{FF}(T(N_c))$ is equal to the spectral amplitudes computed from Eq. (1) at $T = T(N_c)$.

In Eqs. (44) and (46), the fault length, L, and width, W, can be defined by

$$L = a10^{bM} \tag{47}$$

and

$$W = c10^{dM} \tag{48a}$$

or

$$W = e + fM \tag{48b}$$

Table VII

Selected source parameters which are associated with the "four fault models." *

	M	MODEL 1	MODEL 2	MODEL 3	MODEL 4
$\log_{10} \overline{u}$ (cm)	3	-.95 -.71	-.92 -.68	-1.00 .76	-1.02 -.78
	4	.60 .75	.49 .64	.43 .58	.39 .54
	5	1.44 1.49	1.46 1.51	1.41 1.46	1.40 1.45
	6	2.36 2.42	2.41 2.46	2.36 2.41	2.37 2.41
	7	3.05 3.18	3.11 3.23	3.06 3.19	3.05 3.19
	8	3.52 3.71	3.57 3.76	3.54 3.72	3.54 3.72
$\log_{10} A$ (km^2)	3	-.81	-.75	-.95	-1.07
	4	.42	.12	.06	-.13
	5	1.01	.87	.89	.80
	6	1.69	1.63	1.65	1.65
	7	2.32	2.37	2.41	2.41
	8	2.93	3.12	3.17	3.17
$\log_{10} M_0$ (dyne-cm)	3	20.30 20.42	20.37 20.48	20.32 20.44	20.31 20.42
	4	21.91 22.03	21.79 21.92	21.77 21.89	21.67 21.80
	5	23.35 23.40	23.30 23.35	23.29 23.34	23.26 23.31
	6	24.86 24.92	24.86 24.92	24.85 24.90	24.85 24.90
	7	26.43 26.55	26.47 26.59	26.46 26.58	26.46 26.58
	8	27.68 27.87	27.75 27.94	27.75 27.94	27.75 27.93
$f_1(Hz)$	3	4.10	3.82	4.93	5.21
	4	1.0	1.29	1.51	1.67
	5	.48	.45	.51	.53
	6	.17	.15	.17	.17
	7	.056	.050	.055	.055
	8	.018	.016	.017	.017
$f_2(Hz)$	3	5.60	5.22	6.47	8.40
	4	1.36	2.20	2.06	3.20
	5	.74	1.24	.99	1.22
	6	.51	.70	.56	.57
	7	.39	.39	.32	.32
	8	.31	.22	.18	.18

* See table IV for description of fault length, (L) and widths (W) corresponding to these four fault models.

The fault area $A = WL$ and the two corner frequencies $f_1 = 1/\left(\frac{L}{2.2} + \frac{W}{6}\right)$ and $f_2 = \frac{2.2}{W}$ are direct functions of W and L and are thus uniquely defined for the four fault models in terms of a,b,c and d in Table IV. $\overline{u}$ and M_0 are computed for the G4RM (see Eq. (13), and (21)) and thus result in the range of values, as shown.

where, the constants a through f are specified in Table IV for Models 1 through 4. These four models have been chosen to illustrate variations in the definitions of W and L, and all fit the data and many other constraints on the source parameters (see Chapter II). In the following, we will refer to these models again as "four fault models". Table VII summarizes selected source parameter which are associated with these four fault models. In this table M_0 is the seismic moment, $f_2 = v/W$, and $A = WL$.

III.3 EFFECTIVE AND APPARENT STRESS

The stress $\sigma = \sigma_0 - \sigma_f$ will be referred to as effective stress (Brune, 1970). It could represent the difference between the stress on the fault before the earthquake, σ_0, and the frictional stress, σ_f, opposing the dislocation. For simplicity, in this work, unless otherwise stated, we will assume that σ equals the stress drop ($\varepsilon = 1$ in Brune, 1970).

The stress $\sigma_a = \eta \frac{\sigma_0 + \sigma_1}{2}$ will be called apparent stress (Wyss and Brune, 1968), where σ_1 is the stress on fault surface A after the earthquake, and η is the seismic efficiency.

III.4 PEAK AMPLITUDES OF $FS(T)$

It can be shown that the Fourier amplitude spectrum of strong motion acceleration, for frequency $f > f_c$ (corner frequency), is proportional to

$$FS(T)_{\max} \approx \sigma\beta/\mu \tag{49}$$

where $FS(T)_{\max}$ would be the high frequency spectral asymptote in an ideal medium, without attenuation. The corner frequency, f_c, depends on the wave type and the source to station distance for stations near the source, but can be approximated by $f_c \sim \max[f_1,\ f_2]$, with $f_1 \sim [L/v + T_0]^{-1}$ and $f_2 \sim v/W$, where T_0 is the dislocation rise time.

As the frequency increases, the attenuation and scattering diminish the spectral amplitude by $\exp\left(-\frac{\omega\Delta}{2Q\beta}\right)$. This attenuation becomes pronounced near $f_H = \frac{Q\beta}{5\Delta}$, and begins to dominate the shape of the spectral amplitudes for $f > f_H$ (Trifunac, 1973). For small earthquakes (Fig. 1), f_c may be close to or higher than f_H, so that the constant plateau $\sigma\beta/\mu$ in Eq. (49) may not be attained. In those instances, the peak spectral amplitudes will be smaller than $\sigma\beta/\mu$ and can serve only as lower bound estimates of σ. The peaks of $FS(T)$ occur near $T = .2$ sec ($f_p = 5$ Hz, Fig. 15) for $M = 3$ and move towards $T = 1$ sec ($f_p = 1$ Hz) for $M = 8$.

In this chapter, σ will designate the effective stress drop, and the partial stress drop ($\varepsilon < 1$, as defined by Brune, 1970) will not be considered. The empirical scaling Eq. (1) for the G4RM then can be used to evaluated the peak amplitudes of $FS(T)$ for $\Delta = 0$.

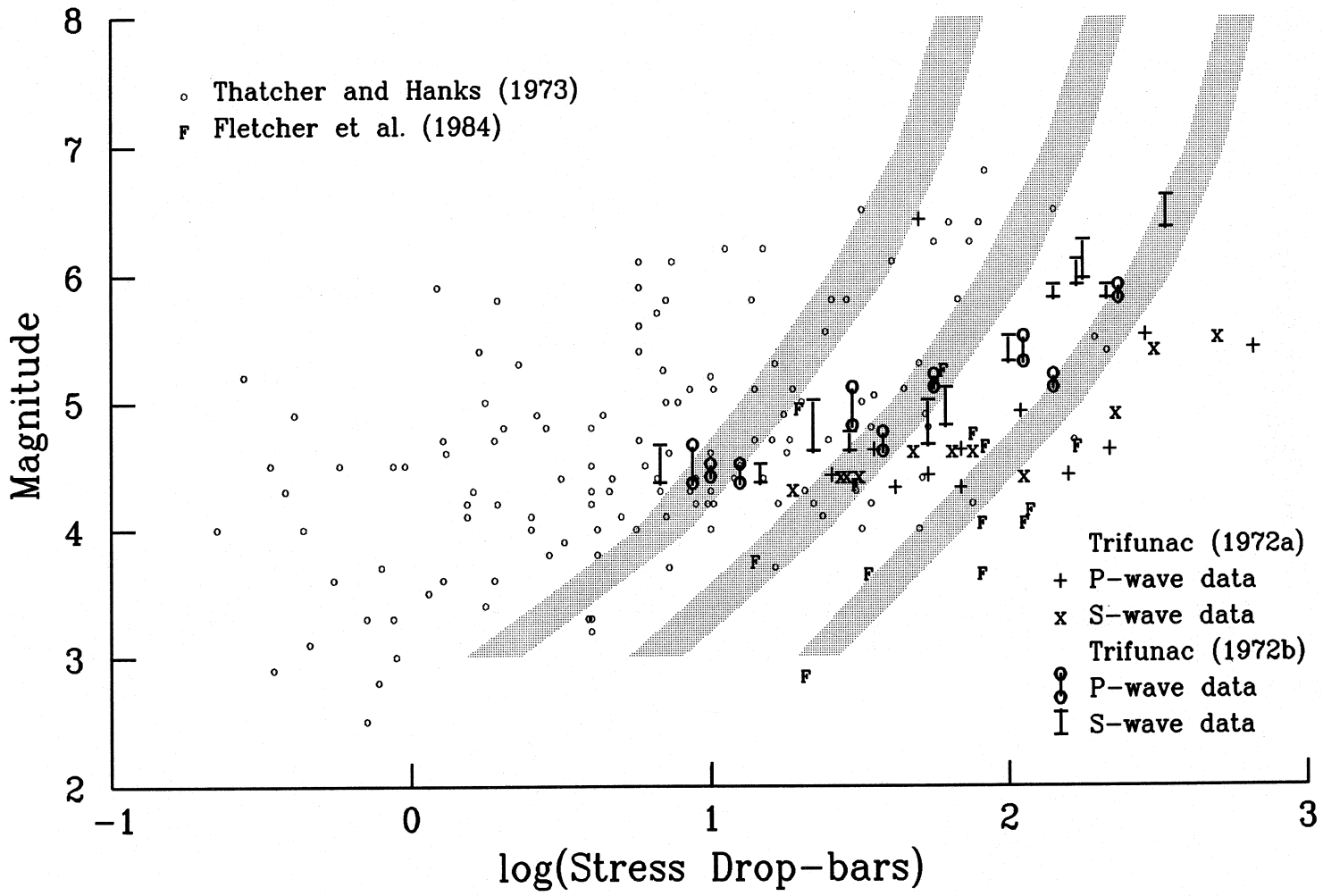

Fig. 16 Estimates of stress drop versus magnitude, with examples from distant (e.g. Thatcher and Hanks, 1973) and near source recordings (Trifunac, 1972; Fletcher et al., 1984). The three shaded zones represent the range of stresses for the G4RM and for probabilities of exceedance equal to 0.1, 0.5 and 0.9.

Taking $\beta \sim 3.5$ km/sec and $\mu \sim 1.3 \times 10^{11}$ dynes /cm^2 then gives $\sigma \sim FS_{\max}(T)$ (in bars if $FS(T)$ is measured in in/sec).

In Fig. 16, this estimate of σ is compared with the results of several studies on stress drop in the same area and for many of the same earthquakes which contributed to the strong motion data base used here. The three shaded areas in Fig. 16, for $p = 0.1$, 0.5 and 0.9, have been computed from G4RM and for $3 < M < 8$. It is seen that the overall agreement of the stress drop estimates is reasonable (relative to strong motion studies), but that the data from seismological (distant) source mechanism studies suggest larger variation with magnitude. This can be explained in part by the high frequency attenuation (low Q) which will progressively reduce the peak amplitudes of $FS(T)$ for decreasing earthquake magnitude.

III.5 STATIC STRESS DROP

The average dislocation amplitude, $\overline{u}$, the average static stress drop, σ, the source dimension, r (e.g. fault width W), and the rigidity of the surrounding rock, μ, can be combined into

$$\overline{u} = C_0 \frac{\sigma r}{\mu} \tag{50}$$

where C_0 is given in Table III and r is defined by the geometry of the source. Solving Eq. (50) for C_0 and taking $r = W$ gives

$$C_0 = \frac{\overline{u}\mu}{W\sigma}, \tag{51}$$

where $\overline{u}$ can be computed from the long period limit of the near field spectrum, using the G4RM and for say $p = 0.5$ in Eq. (7). To model the assumption that smaller events, most probably, occur near stress concentrations with higher μ, while large events, say with $M \geq 6$ and 7, result in large faults and are thus associated with average μ, I will assume that for $M = 3$, 4, 5, 6, and 7, one can take $\mu = (4, 3, 2, 1, \text{and } 1) \times 10^{11}$ dynes/cm^2. The fault width W can be computed from the example data in Table VII, while $\sigma \sim FS(T)_{\max}$. The four C_0 curves, thus computed for the four fault models, are plotted in Fig. 17. The result increases from $\sim .3$ to ~ 1.6 in going from $M = 3$ to $M = 7$. The average trends of C_0 are approximated by $C_0^* = .4$, .5, .65, .85 and 1.6 for $M = 3$, 4, 5, 6 and 7 (Table III and VI in Chapter II).

Starting with the definition of seismic moment $M_0 = \mu A \overline{u}$, and using $A = WL$ and $\overline{u} = C_0 W\sigma/\mu$ gives

$$M_0 = C_0 \sigma L W^2. \tag{52}$$

Computing M_0 for the four fault models, and with σ, L and W available, Eq. (52) can be solved for C_0. As Fig. 18 shows, this approach gives C_0 smaller than that calculated from Eq. (51). Recalling, however, that L and W in both equations are lower bounds (based on the assumption of unilateral faulting), and recognizing that some events in

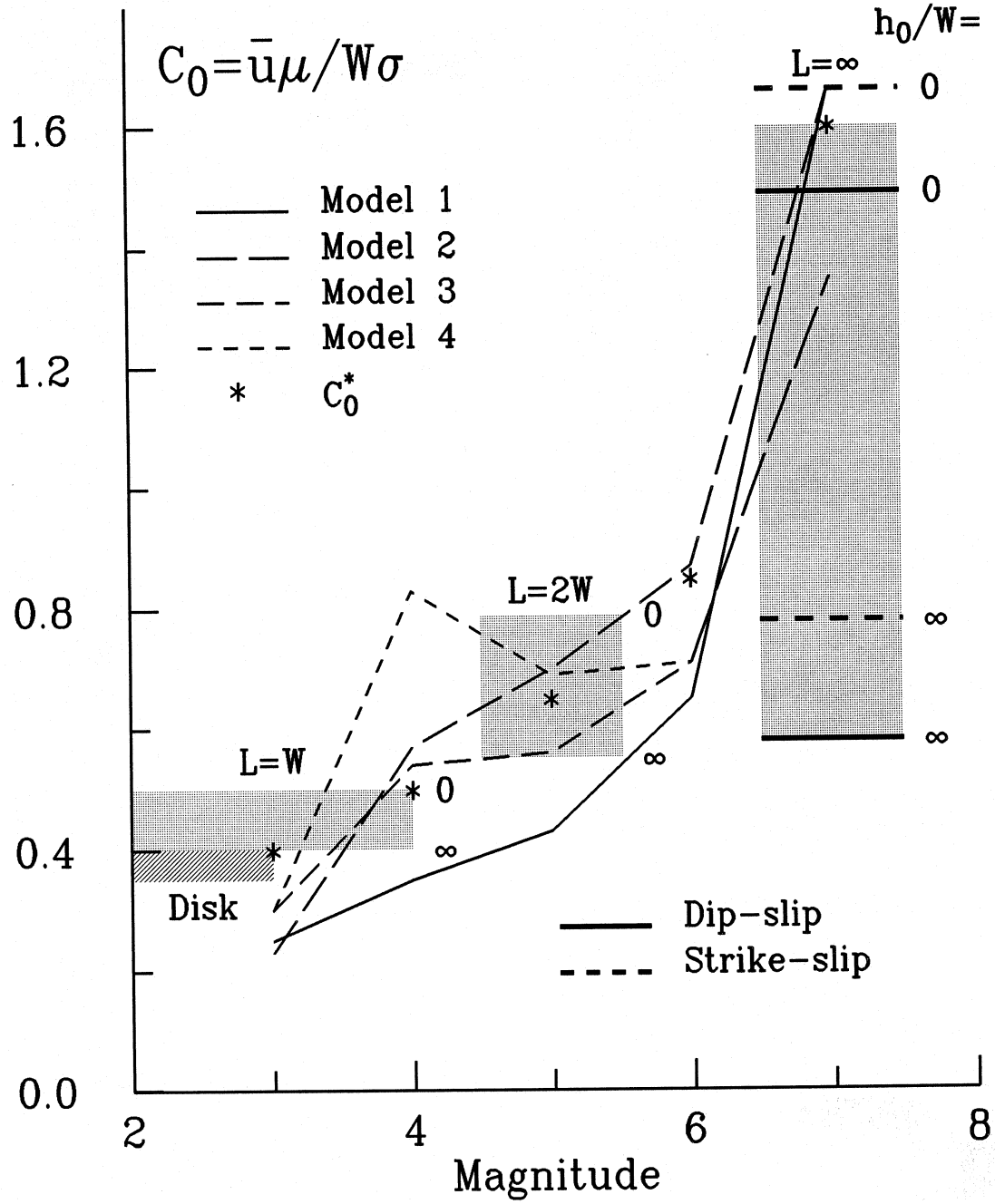

Fig. 17 $C_0 = \bar{u}\mu/(W\sigma)$ versus magnitude for the four fault models 1 through 4. The shaded areas show the range of C_0 derived from analytical (disk) and numerical analyses of static displacements surrounding a rectangular fault (W = width, L = length) and at depth h_0 ($h_0 = 0$ for surface faults, $h_0 = \infty$ for a fault in elastic full space). C_0 from theoretical solutions for infinitely long faults are shown with solid and dashed lines. C_0^* represents the smoothed trend through the data and the numerical and analytical analyses (Table III).

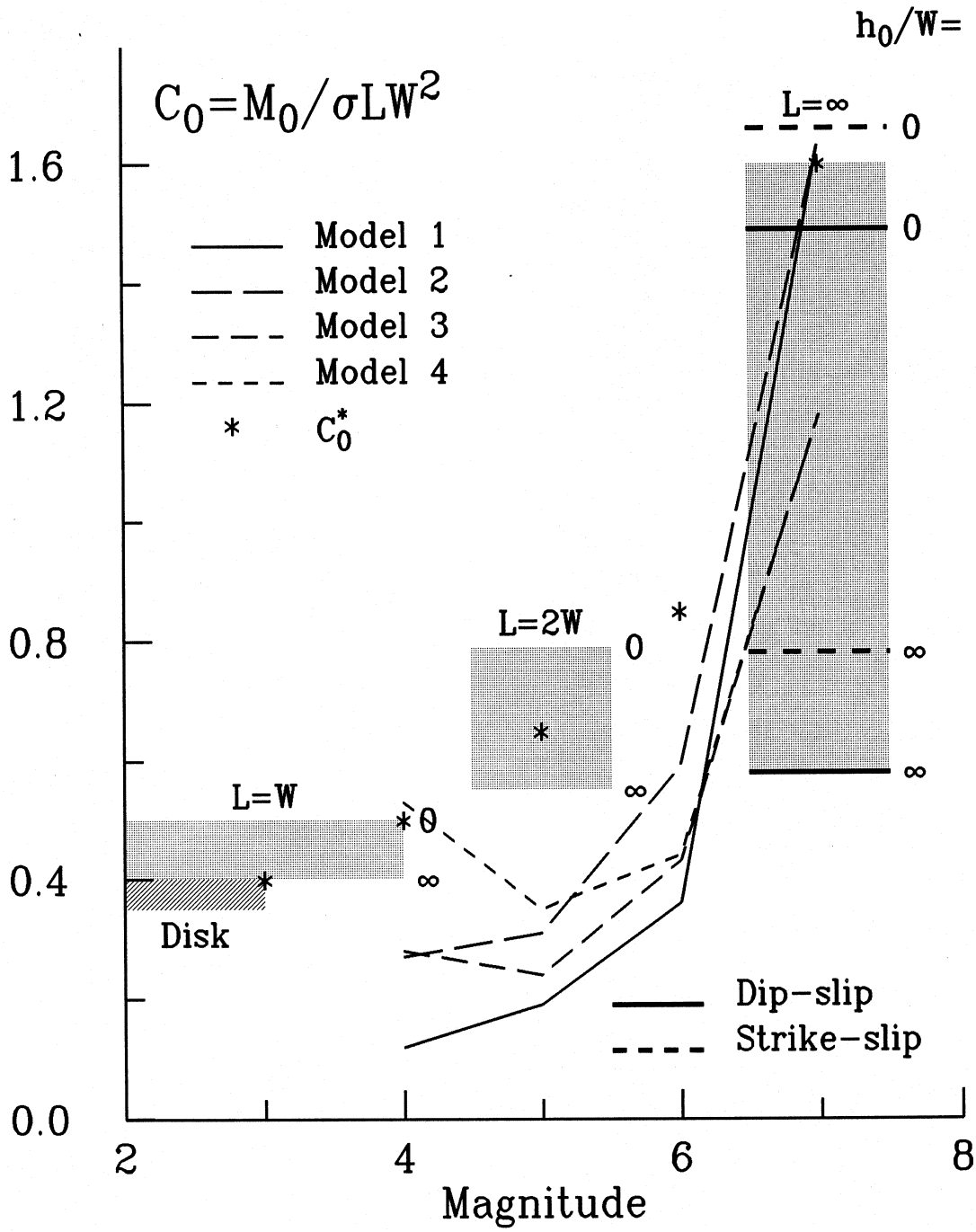

Fig. 18 $C_0 = M_0/(\sigma LW^2)$ versus magnitude for the four fault models 1 through 4. The shaded areas show the range of C_0 derived from analytical (disk) and numerical analyses of static displacements surrounding a rectangular fault (W = width, L = length) and at depth h_0 ($h_0 = 0$ for surface faults, $h_0 = \infty$ for a fault in elastic full space). C_0 from theoretical solutions for infinitely long faults are shown with solid and dashed lines. C_0^* represents the smoothed trend through the data and the numerical and analytical analyses (Table III).

our data base should be bi-lateral in L, would increase the estimates in Fig. 18 by a factor of about 1.5. For small events ($M = 3$ and 4), Eq. (52) appears to underestimate C_0. For those events $L \sim W$, and so the fault area is $\sim L^2$. An increase in the fault dimensions by about 30%, a decrease of the moment estimates by a factor less than 2, or a combination of these effects would modify C_0 in Fig. 18 to agree with that in Fig. 17.

It can be shown also that

$$C_0 \sim f_2 T_0 \tag{53}$$

where $f_2 = v/W$ and T_0 is the dislocation rise time assuming Haskell (1969) type dislocation. Fig. 12 (in Chapter II) shows C_0 computed in this way for the four fault models. Again, we observe very good agreement with the average trend of C_0^*, with essentially "circular" dislocation regime for small events and the transition to dip-slip and strike-slip mechanism for the larger events.

Eqs. (51) (52) and (53) are not independent, but show how different combinations of source parameters can be used to evaluate C_0 and C_0^*. Since these parameters are derived from the long period ($\overline{u}, M_0, L$ via f_1), the intermediate (W via f_2, T_0) and the high frequency (σ) parts of the empirical spectra, and from the parameters which are based on the assumed extrapolated nature of the spectral amplitudes ($\overline{u}, L$), and parameters which are more directly estimated from strong motion data (M_0, W via f_2, T_0), Eqs. (51), (52) and (53) and Figs. 17, 18 and 12 also represent an internal consistency test for properly chosen scaling parameters. We conclude that these results indicate good internal consistency.

III.6 STRAIN DROP

The quantity σ/μ represents strain drop during an earthquake. It is equal to $\overline{u}/(WC_0^*)$. If the average (representative) μ is known, the stress drop can be computed from the high frequency amplitudes of $FS(T)$ (Eq. (49)). Then, evaluating the strain drop from $\overline{u}/(WC_0^*)$ represents intermediate (W) and long period ($\overline{u}$) estimate. Fig. 19 presents $\log_{10}\left(\frac{\overline{u}}{WC_0^*}\right)$ for our four fault models, plotted versus $\log_{10} M_0$. It shows a well defined linear growth which can be represented by

$$\log_{10}\frac{\sigma}{\mu} = \log_{10}\frac{\overline{u}}{WC_0^*} = -12.78 + .382\log_{10} M_0. \tag{54}$$

It also shows the related results by Izutani (1981) and by Papageorgiou and Aki (1985). The strain increases from $\sim 10^{-5}$ for $M = 3$ to $\sim 10^{-3}$ for $M = 7$.

It is reasonable to speculate that small earthquakes occur around high stress concentrations which are associated with "more rigid" geological environment, since in the inhomogeneous material more rigid components will tend to "attract" higher forces (stresses). Here, this hypothesis can be evaluated by computing σ from $FS(T)_{\max}$ and dividing the result by $\log_{10}\frac{\sigma}{\mu}$, computed from Eq. (54), with the assumed relationship

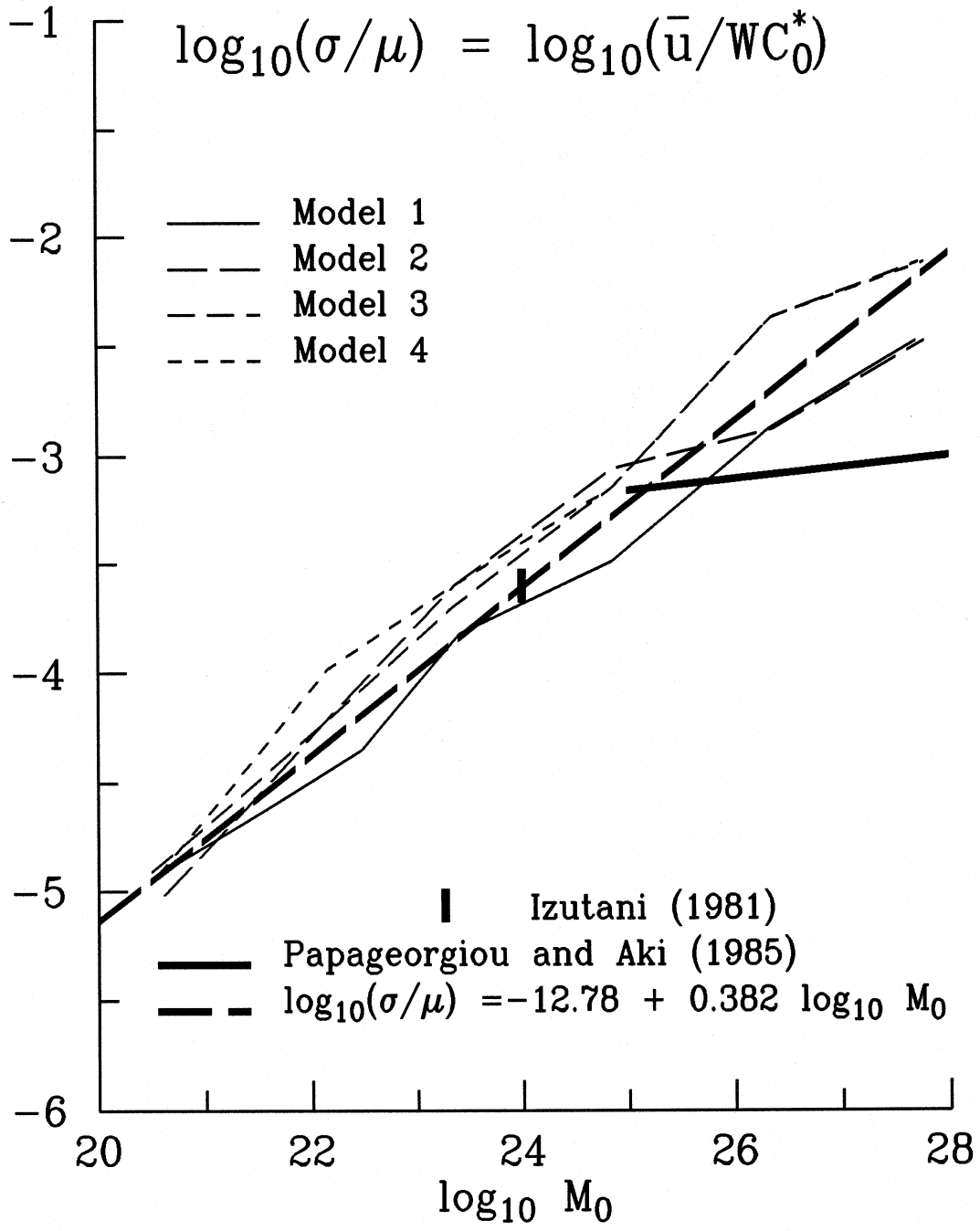

Fig. 19 Strain drop, $\log_{10}(\sigma/\mu) = \log_{10}[\overline{u}/(WC_0^*)]$ versus $\log_{10} M_0$.

$\log_{10} M_0 = 1.5M + 16$. Using the average stress drop shown in Fig. 16 gives $\mu \sim$ (5, 4, 3, 2 and 1) $\times 10^{11}$ dynes/cm^2 for $M = 3$, 4, 5, 6 and 7.

III.7 DYNAMIC STRESS DROP

Here we use again the Brune (1970) concept of the effective stress σ, which models the difference between the stress before the earthquake and the "frictional" stress operating during the earthquake. We also assume $\sigma \sim FS(T)_{\max}$, and ignore the possible low-pass filtering effects (resulting in smaller values of σ), caused by the attenuation quality factor Q, for small magnitude events, say $M \leq 4$. Then, referring to Fig. 16, we wish to explain the observed trends of σ.

Joyner (1984) suggests that high frequency spectral acceleration should be proportional to $A^{1/2}$ for all earthquakes. To test this hypothesis I plotted σ versus $(WL)^{1/2}$ for the four fault models. The results are shown in Fig. 20. If we accept the two assumptions: 1) that σ can be estimated by $FS(T)_{\max}$ at $\Delta = 0$, and 2) that the four fault models are representative, then this hypothesis by Joyner does not hold. As Fig. 20 shows, σ increases at a progressively slower rate as $(WL)^{1/2}$ increases. It appears that σ is not proportional to the linear dimension of the source.

Scholz (1982) finds that $\overline{u} \sim L$ and that $\overline{u} \not\sim W$, and presents alternatives to the common relations between σ and the fault width. Our models indicate that $\overline{u}$ is not related linearly to either L or to W (Figs. 21 and 22). If we plot $\overline{u}$ versus L, so that small dislocation amplitudes are compressed near the origin, then $\overline{u}$ for $M = 7$ and 8 suggest $\overline{u} \sim \alpha_0 L$, where $\alpha_0 = 37.5$. But, this falls in the range of amplitudes ($M = 7$ and 8) which are outside the range of the overall strong motion data and, so, this cannot be taken as a reliable support for the linear hypothesis $\overline{u} \sim L$. It is of interest to note that Sholtz (1982) finds 10 to 15 times smaller α_0 ($\alpha_0 = 1$ to 2 for strike slip and thrust earthquakes). For large intra plate earthquakes Matsuda et al. (1980), find $\alpha_0 \sim 10$. This "discrepancy" in α_0, of 2 to 20 times, can be eliminated by recognizing that our L represents a lower bound (assuming unilateral spreading of the dislocation). For bilateral faulting, this "discrepancy" would be reduced to 1 to 10. Furthermore, since some data on L comes from inferences based on the distribution of aftershocks, which often tend to overestimate the initial "dynamic" fault dimensions, it is seen that this discrepancy can further be reduced or eliminated.

We plotted σ versus $(L/W)^{1/2}$, $\log_{10}(L/W)$ and L/W and found that only the plot versus $\log_{10}(L/W)$ could be interpreted to lead to a simple "linear" trend, but with too large scatter to make a convincing case.

To analyze the observed high frequency spectral accelerations we consider the following model (Fig. 23). If x represents length, at some representative depth, along the seismogenic layer, say less than 20 km deep (in California), then the stress in the crust might be distributed as in Fig. 23b. For some strain rate, averaged over the thickness of

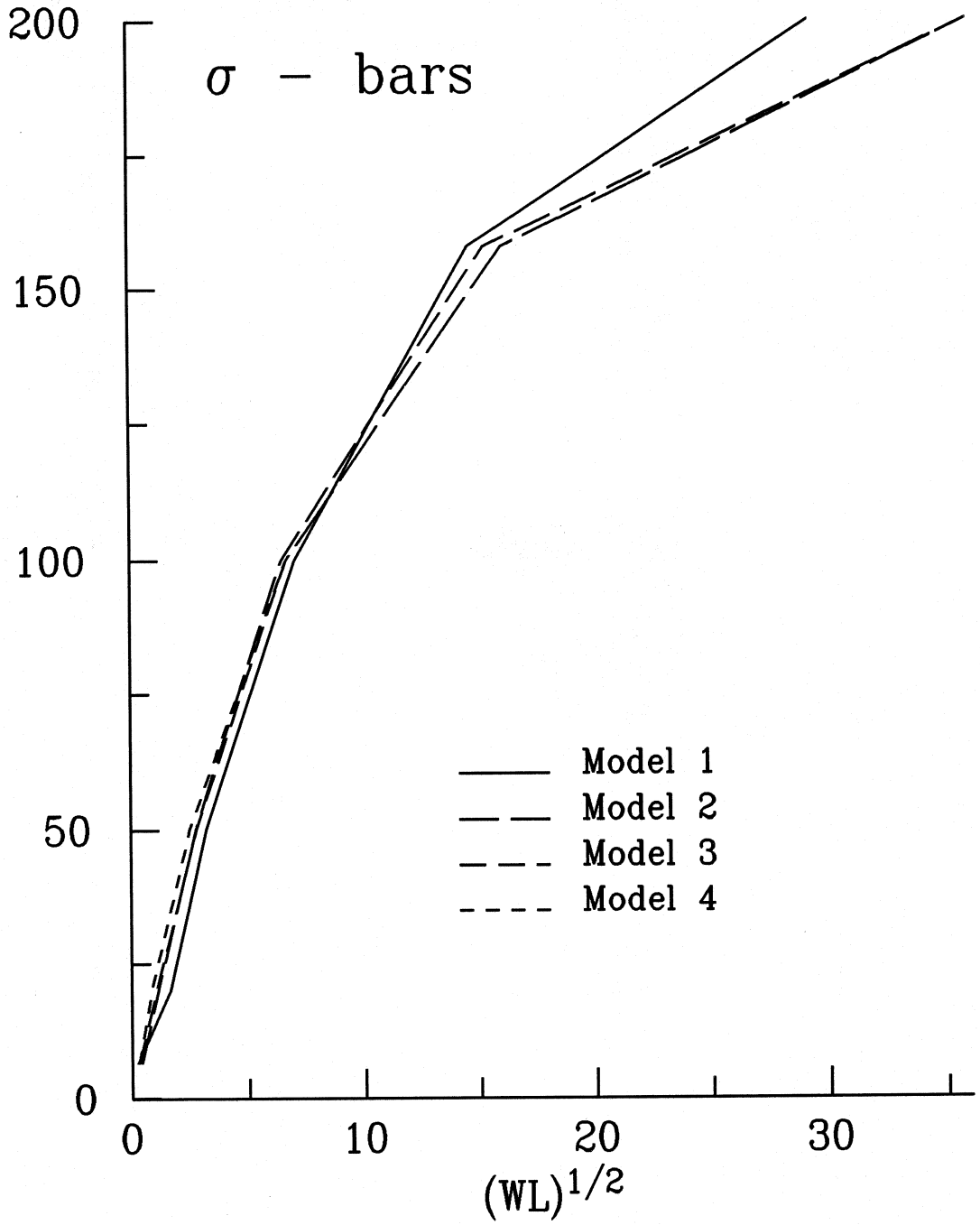

Fig. 20 Stress drop versus characteristic fault dimension $(WL)^{1/2}$.

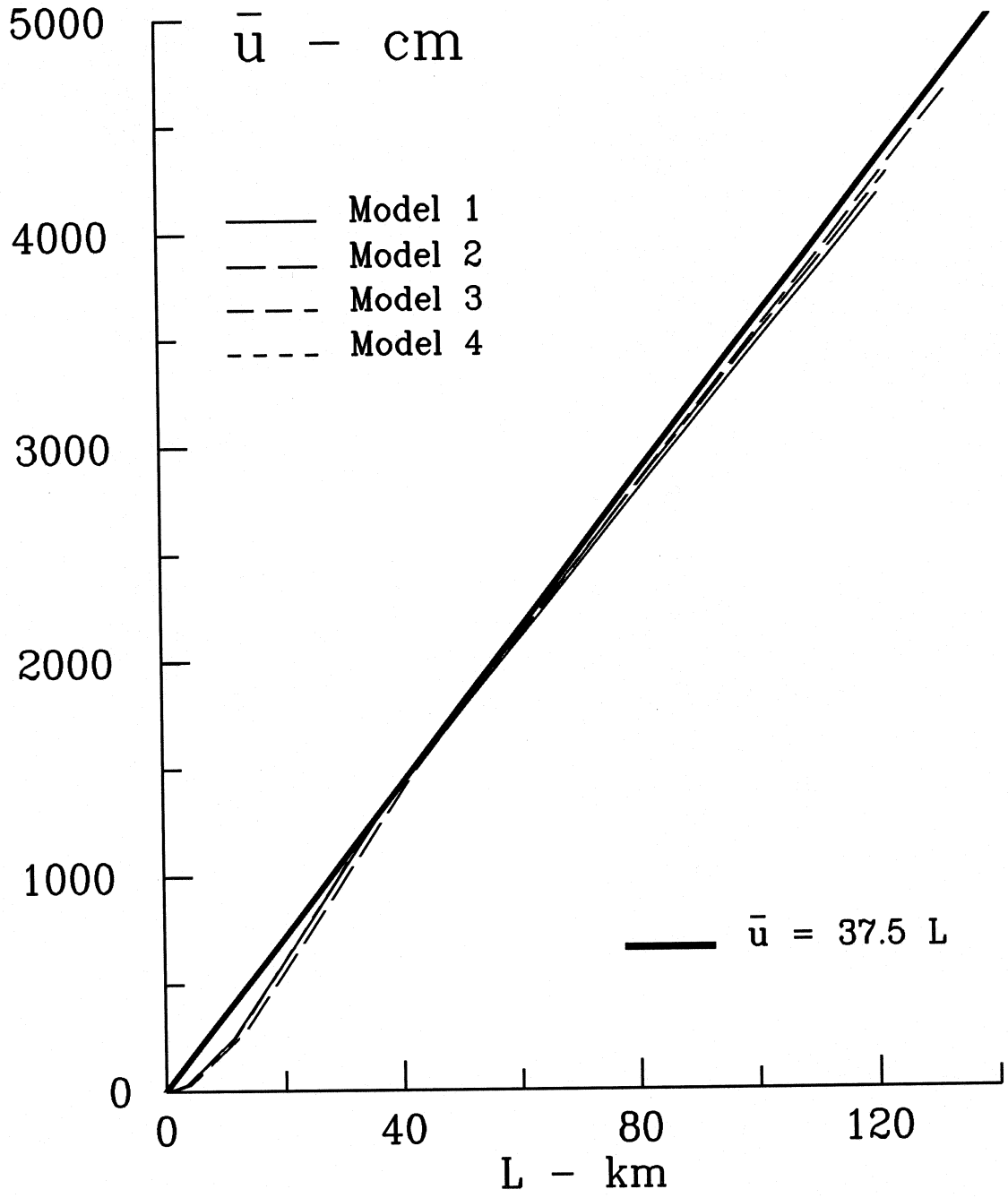

Fig. 21a Average dislocation amplitude versus fault length.

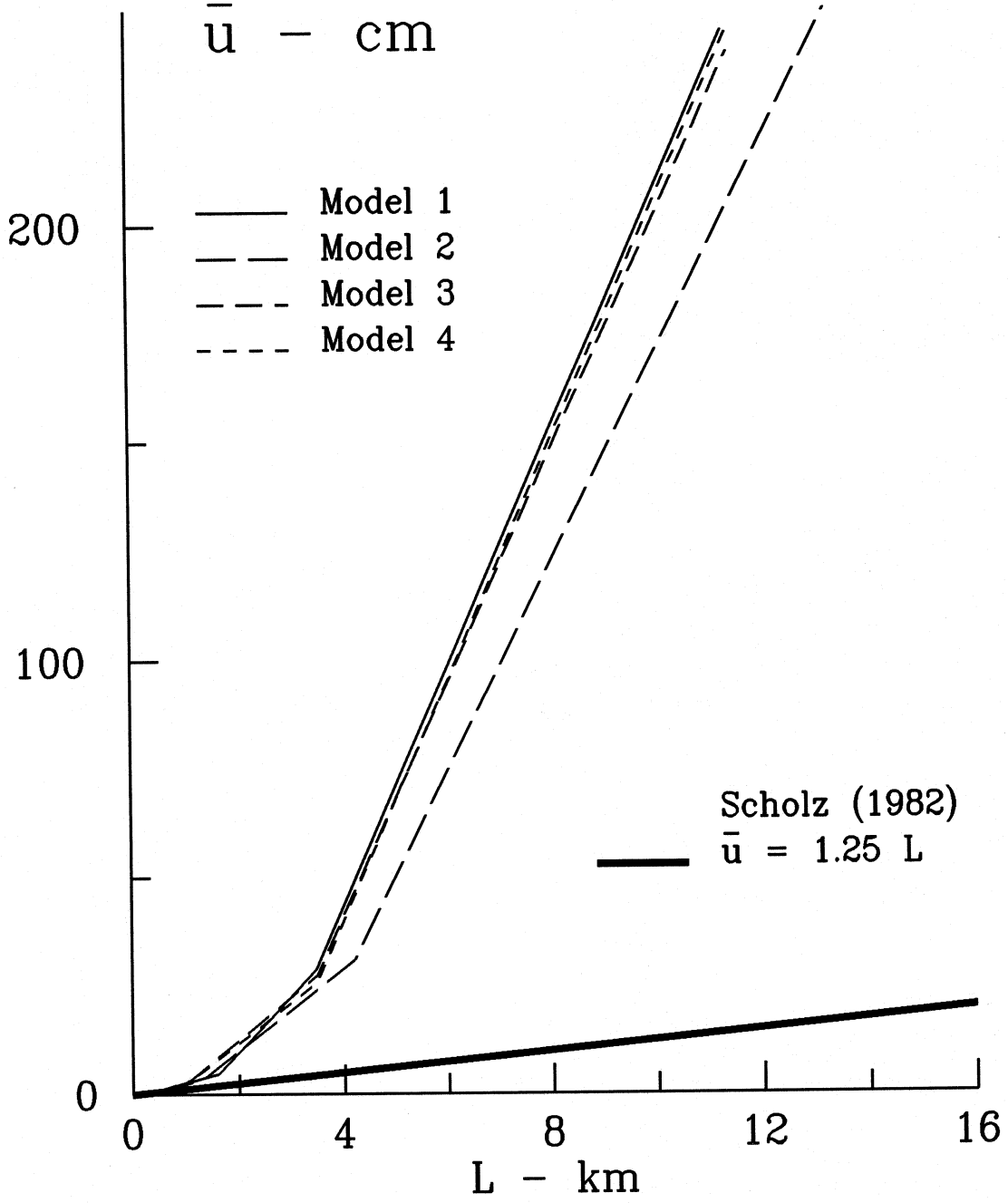

Fig. 21b Average dislocation amplitude versus fault length.

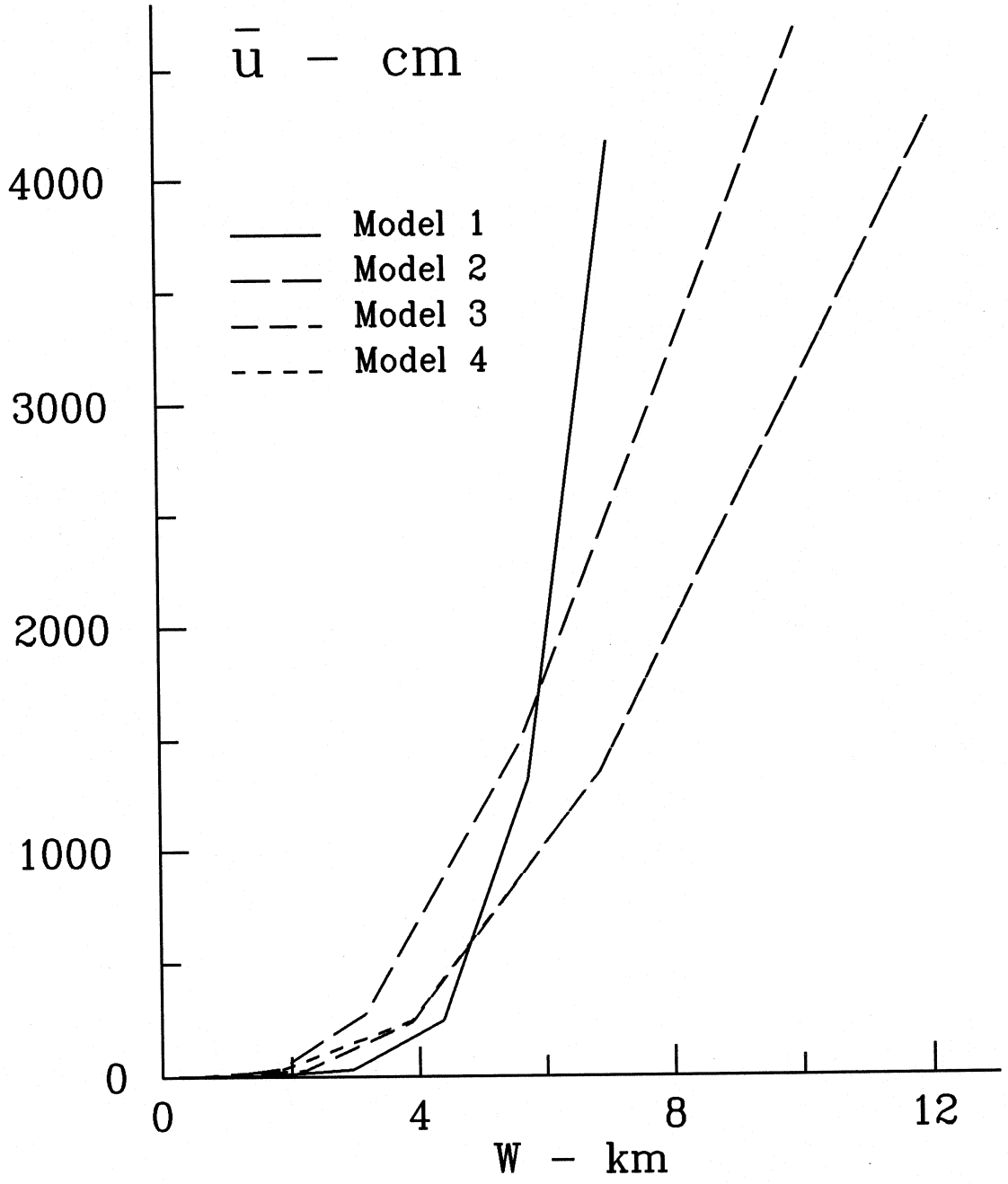

Fig. 22 Average dislocation amplitude versus fault width.

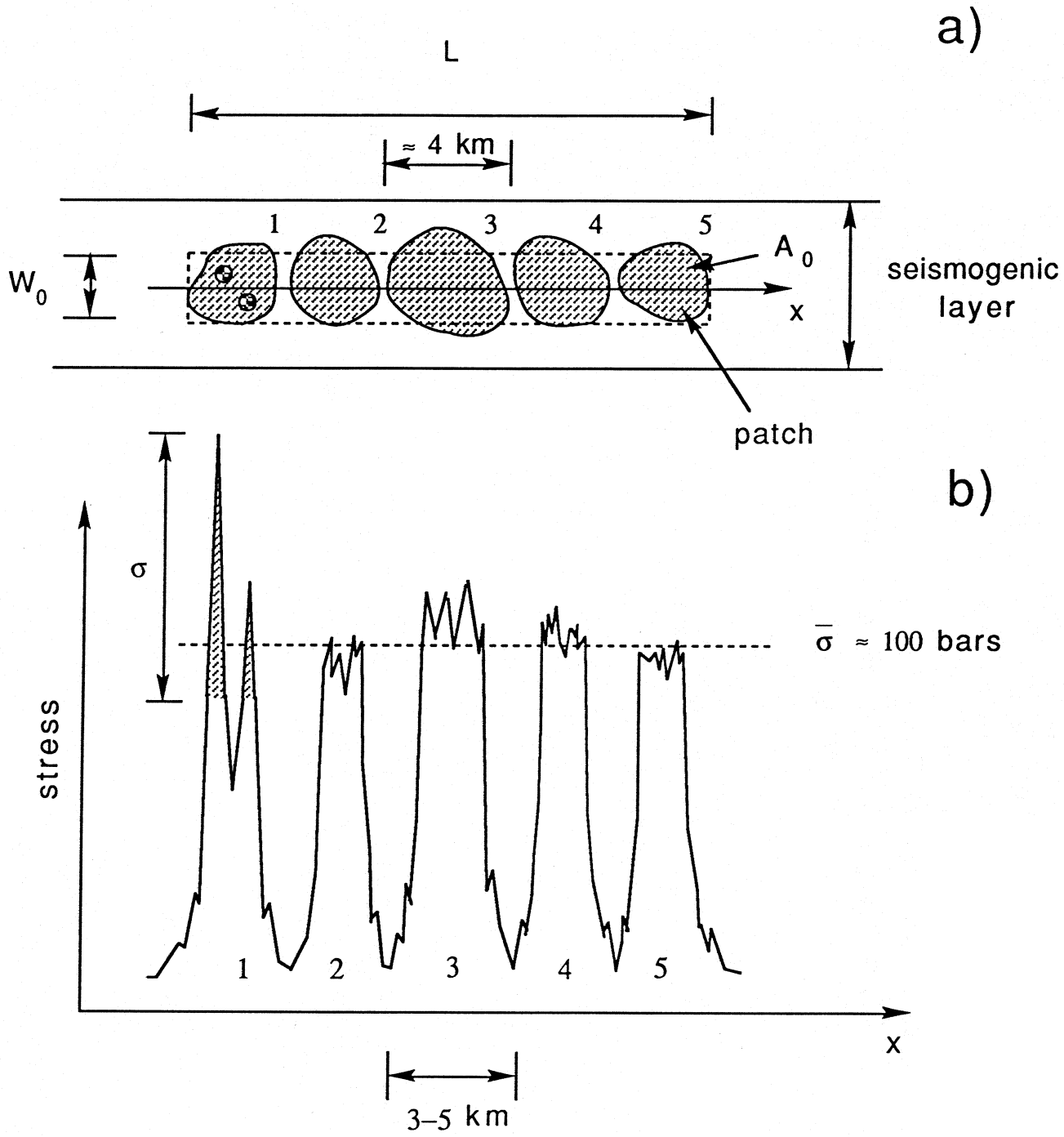

Fig. 23 a) Vertical cross-section through shallow crust showing a seismogenic layer and a fault with the "subevents". b) Distribution of stresses along the fault length L.

this seismogenic layer, the stress fluctuations can result from large scale fluctuations in the rigidity μ, can be caused by some parts of the fault plane being locked, while other parts are continuously slipping, can result from stress concentrations near those parts of the fault which remained locked during previous earthquakes or can be caused by a combination of these, for example. When a "small" earthquake occurs it will release high stresses over some area (the shaded peak in Fig. 23b and the small "disk" area in Fig. 23a). If this area of stress concentration is "small" and is surrounded by relatively low stresses, the outcome will be a "single event" earthquake of magnitude $M <\sim 5$. As this stress drop increases, and as it is released over progressively larger area, larger magnitude (moment) event will take place. As the event area becomes larger, it may release stress concentrations on nearby stress peaks. On the average, it may be expected that an oval fault slip area will be associated with an event as long as its fault dimensions are smaller than W_0 (Fig. 23a). For the purpose of this discussion we will assume $W_0 \sim 3 - 5$ km (for unilateral faulting) (e.g. see Archuleta, 1982; Harzell and Heaton, 1983; Harzell and Helmberger, 1982; Olson and Apsel, 1982; Trifunac, 1972a,b; 1974; Wald et al., 1991, in the references for Chapter II). As larger inertial forces are developed with progressively larger stress drop, accelerating the surrounding medium with progressively larger volume, the first initiating event will grow to the largest possible patch size A_0 (here assumed to be ~ 16 km^2) and the excess inertial energy will trigger release of stresses in the area of another, presumably nearby patch, triggering the second event there. Since the growth of the single fault area (patch) is limited by the width of the seismogenic zone (W_0), large earthquakes will have to occur on a sequence of patches, more or less extended and propagating along x in one or in two directions. The final fault area $A \sim WL$ will then consist of a number of patches, some smaller some larger, reflecting the nature of stress oscillations along x, but in no case will a patch size be much wider than W_0. Obviously, the size of W_0 will vary from one tectonic region to another, and will depend on the specific geometrical and physical properties of the area surrounding the fault.

In the above model, the peak spectral acceleration will be associated with the largest of the nearby peaks in the stress pattern when $M > 5$. In such cases the peaks of stresses plotted in Fig. 23b should be thought of as being low pass filtered below a suitable frequency (say ~ 1 Hz) to simulate the attenuation effects between the recording station and more distant contributing peaks. Since, for simplicity, we used $p = 0.5$ in selecting the $FS(T)_{\max}$ amplitudes, the high frequency spectral acceleration should be proportional to the expected value of the largest peaks of the stress patches contributing to the motions recorded. Assuming that the stress indeed fluctuates along x, as suggested by Fig. 23b, then the expected value of the effective stress is

$$E[\sigma] \sim \overline{\sigma}(\ln N_p)^{1/2} \tag{55}$$

where $E[\sigma] \sim FS(T)_{\max}$ for $p = 0.5$, $\overline{\sigma}$ is the root mean square of the stress peaks in Fig. 23b, and N_p is the number of peaks in the stress function after low-pass filtering the stress diagram to maintain only the "long period" stress fluctuations. Since $N_p \sim WL/A_0$, N_p can be determined if A_0 is known or assumed. We will assume that for a single patch $A_0 \sim WL$, but that both W, $L < 4$ km. Using definitions of L and W for

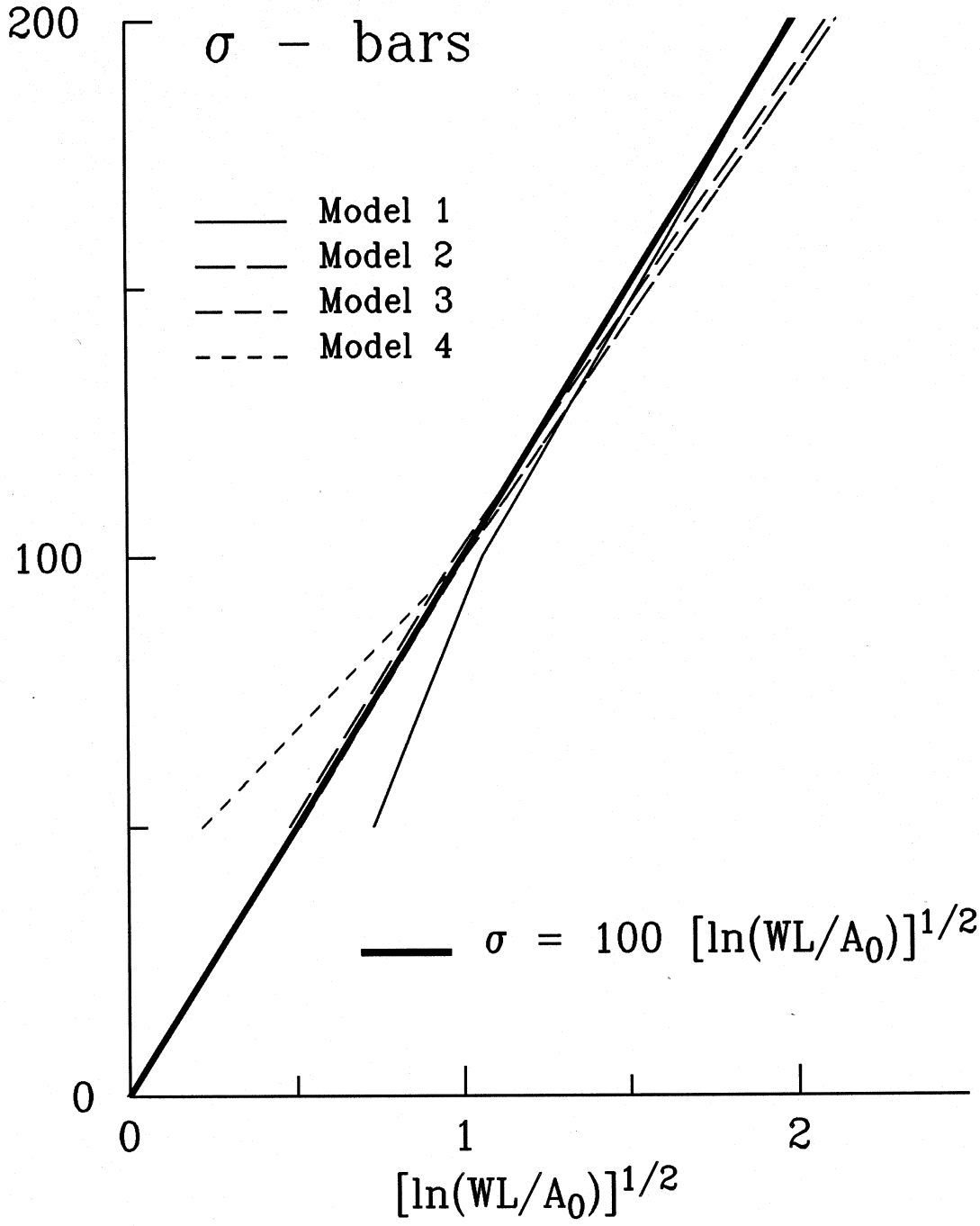

Fig. 24 Stress drop, σ, versus $\ln\left[\frac{WL}{A_0}\right]^{1/2}$ for fault models 1 through 4 and for $M \geq 5$.

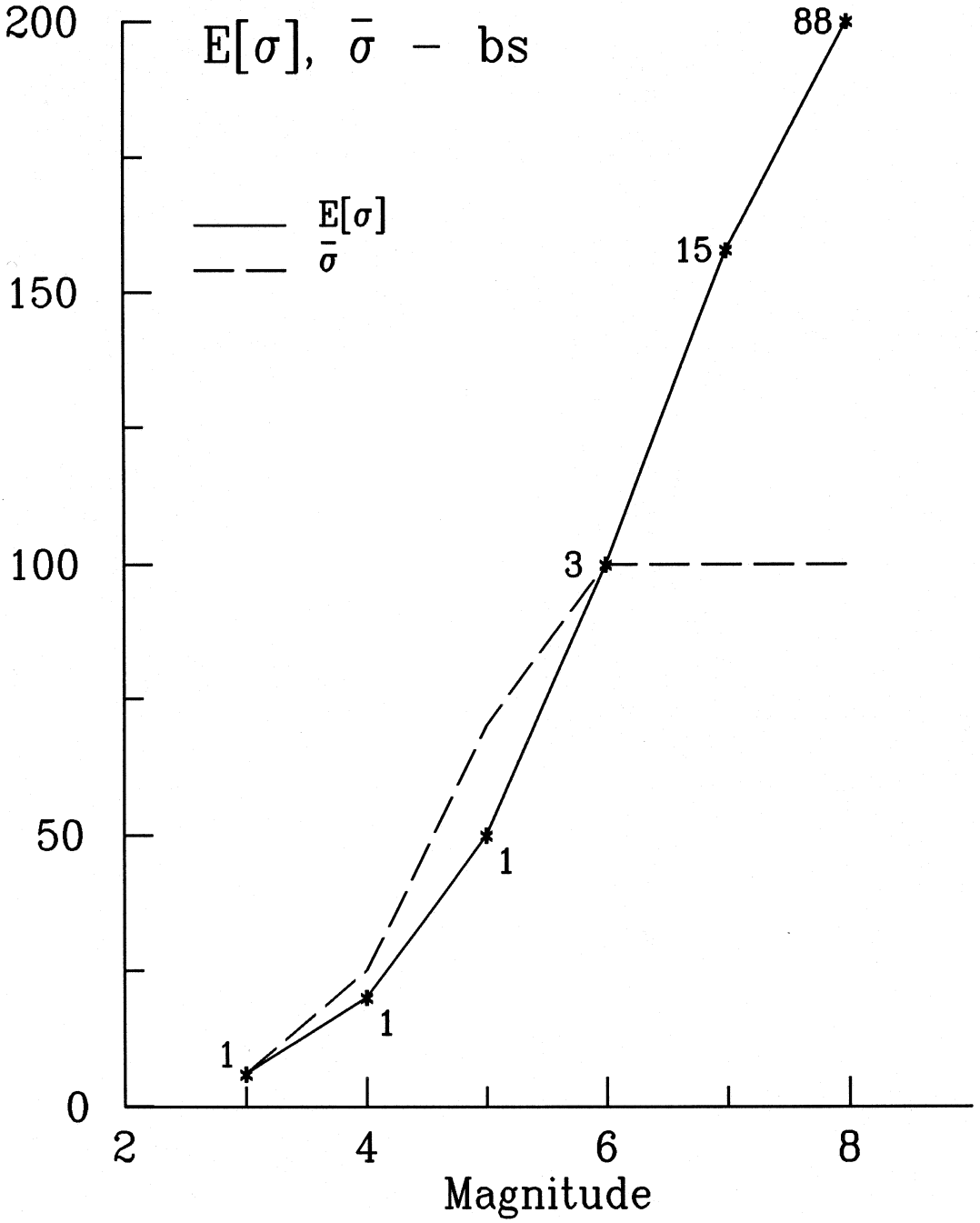

Fig. 25 The expected value of the effective stress (stress drop), $E[\sigma]$, and the root mean square of the stress peaks, $\overline{\sigma}$, versus magnitude. The number of subevents ($N_P = A/A_0$) in Eq. (55) is also shown at magnitudes 3, 4, 5, 6, 7 and 8.

the four models in Table IV, for $M = 4$, 5, 6, 7 and 8, the estimates of A_0 become $\sim$ 1, 6, 16, 16 and 16 km^2 respectively. For $M > 5$, this gives $E[\sigma] \approx 100 \left(\ln \frac{A}{A_0}\right)^{1/2}$, as shown in Fig. 24. Remarkably linear growth of $E[\sigma]$ versus $\left(\ln \frac{A}{A_0}\right)^{1/2}$ and small scatter of the results predicted for the four extrapolation models, suggest that this may be a useful model for further testing and verification. $\overline{\sigma} = 100$ bars is also in good agreement with numerous seismological and strong motion studies (Anderson, 1991) of stress drop inferred from the high frequency spectral amplitudes of recorded motion.

Within the frequency resolution of the shortest wave length data available today (say less than .5 km for $f < 2$ Hz), which are imposed by the limits associated with the distances at which the records are obtained, by Q and by the size of geological inhomogeneities along the wave path, and not by the recording instrumentation, the above suggests that we can think of an earthquake as becoming a multiple event for $M \geq 5$ (in California). Of course, there is no physical basis to assume that there are no multiple events for $M < 5$ also, but we just may not be able to "see" them with the frequency resolution characteristics in our current data.

For $M < 5$, the situation is different. Here $A < A_0$, and the dynamic stress is associated with stress release on one or two extreme stress peaks. The dislocation stops because the surrounding stress amplitudes are small, or because of material barriers or constraints. Some of these events may have very large dynamic stress drop (Trifunac 1972a,b), but this may occur at very high frequencies, whose amplitudes are low-pass filtered by scattering and by attenuation. As the fault dimensions increase, the stress drops further, until for a single patch, near say $M = 5$ to 6, it reaches "troughs" in the stress diagram (Fig. 23b). The average stress drop implied by $\sigma = FS(T)_{\max}$ (Fig. 16) is then almost same as $\overline{\sigma}$. Beyond $M \sim 6$, in this representation, the local stress drop does not grow because the large earthquake is associated with larger $\overline{\sigma}$, but because A/A_0 becomes large and, so, the probability of finding a larger peak increases. Fig. 25 summarizes this for $E[\sigma]$ and $\overline{\sigma}$, showing graphically this transition in the nature of the problem near $M = 6$.

Since $\frac{\sigma}{\mu} = \frac{\overline{u}}{WC_0^*}$, it is seen that $\overline{\sigma}/\mu = (100 \times 10^6 \text{ dynes/cm}^2)/ (1 \times 10^{11} \text{ dynes/cm}^2)$ $= 10^{-3}$. The trend of strain estimates $(\overline{u}/WC_0^*)$, based on the intermediate and long period estimates gives about 10^{-3} near $M = 6$ ($\overline{\sigma} = 100$ bars), and about 3×10^{-3} near $M = 8$ ($\sigma \sim 200$ bars).

III.8 MAGNITUDE VERSUS FREQUENCY OF OCCURRENCE

The above hypothetical model can be used as a basis to explore the possible implications for the magnitude frequency relationships in a region. Associating an earthquake event with a patch of stresses on the fault surface, where there is larger than average stress (in the sense of Fig. 23b, and of course, in two dimensions), can be adopted as a

causative mechanism to determine the size (area) and the number of events which can occur on the existing fault. Let W_{F_i} and L_{F_i} represent the widths and the lengths of L_T faults in the region. Let W_M and L_M represent the typical length and width of a patch (for $M < 5$ to 6) or of a group of patches (for $M > 6$), which are determined by the four fault models, for a magnitude interval $M \pm \Delta M/2$. Then the number of earthquakes of magnitude $M \pm \Delta M/2$ which may occur in the region during given time will be $N_M = \left(\sum_{i=1}^{L_T} W_{F_i} L_{F_i}\right) \Big/ (L_M W_M)$, where the summation is taken over all L_T faults in the area. In terms of the expressions for L and W for our four fault models (Table IV),

$$N_M = \frac{\sum_{i=1}^{L_T} W_{F_i} L_{F_i}}{ac} 10^{-(b+d)M}. \tag{56}$$

Since the typical magnitude frequency relationship is of the form $\log_{10} N_M = a_M - b_M M$, where N_M is the number of earthquake in the magnitude interval $M \pm \Delta M/2$, it is seen that $a_M = \left(\sum_{i=1}^{L_T} W_{F_i} L_{F_i}\right) \Big/ (ac)$ and $b_M = b + d$.

Empirical seismicity estimates usually give $0.8 < b_M < 1$. From Table IV it is seen that, for $M < M_*$, our results suggest $b_M \sim 1.1$, and for $M > M_*$, $b_M \sim .8$, i.e. there is a change in the slope of $\log N_M$ versus M relationship. This would imply $b_M \sim 1.1$ for frequency magnitude relationships in the subduction zones, for example, or where the thickness of the seismogenic zone does not provide a constraint on one of the fault dimensions, and $b_M \sim .5$ to .6 for a very shallow seismogenic zone (where $W \sim$ const.).

For example, for the period between 1900 and present, the Benioff zone only, south of Prince William Sound, and bellow Kenai Peniusula and Kodiak island in Alaska, gives $b_M \sim .9$ (for $5 < M < 8$). On the other hand, for shallow faults in the deformed zone just behind the trench, and the Castle Mountain Fault north of Cook Inlet, $b_M \sim .5$ (for $4 < M < 7$). In Southern California, in the Imperial Valley region, for the period from 1932 to 1971 (Hileman et al., 1973), for $3 < M < 5$, $b_M \sim 1$, and for $M > 5$, $b_M \sim .75$.

III.9 DISCUSSION AND CONCLUSIONS

The observed trends of the peaks of the Fourier amplitude spectra of strong motion acceleration ($\sim \sigma$) and of the corresponding estimates of the source dimensions (fault width W and fault length L), together with the average dislocation, $\overline{u}$, the seismic moment, M_0, and the dislocation rise time, T_0, can be interpreted by a population of events, which, for $M \lesssim 5$, have essentially "circular" faults ($W \sim L$) and are associated with one "patch" (single event, see Fig. 23). Near this magnitude, the width of the patch approaches 3-5 km and is constrained to grow further by the thickness of the seismogenic zone in California. For larger events, the larger fault area is realized by accretion of several ($M \sim 6$) to many such patches ($M \sim 8$). The small and intermediate events ($L < 2W$) can be visualized as "circular" dislocations at some depth, but for $M > 7$ our

analysis and the available strong motion data favor very long surface faults (strike slip or dip slip, Figs. 12, 17 and 18).

The available strong motion data is consistent with strain drop $\sim 10^{-5}$ for $M \sim 3$ and with $\sim 10^{-3}$ for $M \sim 7$. For large events, $\overline{u}$ appears to be proportional to the fault length (L), but for smaller events $\overline{u} \not\sim L$ and $\overline{u} \not\sim W$.

For $M > 5$, the expected amplitude of the stress drop, $E[\sigma] \sim FS(T_p)$, grows linearly with $[\ln(WL/A_0)]^{1/2}$, where $A_0 \sim 16$ km^2, and the slope of this linear growth is constant with $\overline{\sigma} = 100$ bars, the root mean square of the peaks of stress drop on the fault surface. Our model then can be interpreted to be consistent with $\overline{\sigma}$ growing to ~ 100 bars for $M \sim 6$ and remaining almost constant for $M \gtrsim 6$. Thus, in this interpretation, $E[\sigma]$ continues to grow for $M > 6$, but because $\left[\ln \frac{A}{A_0}\right]^{1/2}$ grows for large events, while $\overline{\sigma}$ remains close to a constant.

III. 10 REFERENCES

Amini, A., V.W. Lee, and M.D. Trifunac (1982). Noise in Earthquake Accelerograms, *ASCE, EMD*, **108**, 1121-1129.

Anderson, J.G. (1991). Strong Motion Seismology, in Contributions in Seismology, AGU, Washington, D.C.

Båth, M. and S.J. Duda (1964). Earthquake Volume, Fault Plane Area, Seismic Energy, Strain, Deformation and Related Quantities, *Ann. Geofis.* (Rome), **17**, 353-368.

Brune, J.N. (1970). Tectonic Stress and the Spectra of Seismic Shear Waves, *J. Geophys. Res.*, **75**, 4997-5009.

Gusev, A.A. (1983). Descriptive Statistical Model of Earthquake Source Radiation and its Application to an Estimation of Short-Period Strong Motion, *Geophy. J. R. Astr. Soc.*, **74**, 787-808.

Gutenberg, B. and C.F. Richter 1956). Earthquake Magnitude, Intensity, Energy and Acceleration, *Bull. Seism. Soc. Amer.*, **46**, 105-145.

Haskell, N.A. (1969). Elastic Displacement in the Near Field of a Propagating Fault, *Bull. Seism. Soc. Amer.*, **59**(2), 965-980.

Hileman, J.A., C.R. Allen, and J.M. Novdguist (1973). Seismicity of the Southern California Region, Seismological Laboratory, Calif. Inst. of Tech., Pasadena, California.

Irikura, K. and T. Yokoi (1984). Scaling law of Seismic Source Spectra for the Aftershocks of 1983 Central-Japan-Sea Earthquake, *Abstracts of the Seismological Society of Japan*, No. 1.

Izutani, Y. (1981). A Statistical Model for Prediction of Quasi-Realistic Strong Ground Motion, *J. Phys. Earth*, **29**, 537-557.

Joyner, W.B. (1984). A Scaling Law for the Spectra of Larger Earthquakes, *Bull. Seism. Soc. Amer.*, **74**(4), 1167-1188.

Kanamori, H. and D.L. Anderson (1975). Theoretical Basis of Some Empirical Relations in Seismology, *Bull. Seism. Soc. Amer.*, **65**, 1073-1093.

Keilis-Borok, V.I. (1960). Investigation of the Mechanism of Earthquakes, Soc. Res. Geophys. 4, (Transl. Tr. Geofiz. Inst. 40) Am. Geophys. U. Consultants Bureau, New York.

Lee, V.W., A. Amini and M.D. Trifunac (1982). Noise in Earthquake Accelerograms, *ASCE, EMD*, **108**, 1121-1129.

Lee, V.W. and M.D. Trifunac (1990). Automatic Digitization and Processing of Accelerograms Using PC, Dept. of Civil Eng., Rep. No. 90-03, Univ. Southern California, Los Angeles, California.

Matsuda, T., H. Yamazaki, T. Nakata, and T. Imaizuni (1980). The Surface Faults Associated with the Rikuu Earthquake of 1896, *Bull. Earthquake Res. Inst. Univ. Tokyo*, **55**, 795-855.

Papageorgiou, A.S. and K. Aki (1985). Scaling Law of Far-Field Spectra Based on Observed Parameters of the Specific Barrier Model, *Pageoph*, **123**, 353-374.

Parsons, I.D., J.F. Hall and G.A. Lyzenga (1988). Relationships Between the Average Offset and the Stress Drop for Two- and Three-dimensional Faults, *Bull. Seism. Soc. Amer.*, **78**(2), 931-945.

Richter, C.F. (1958). Elementary Seismology, Freeman and Co. S. Francisco.

Scholz, C.H. (1982). Scaling Laws for Large Earthquakes: Consequences for Physical Models, *Bull. Seismol. Soc. Amer.*, **72**, 1-14.

Savage, J.C. (1972). Relation of Corner Frequency to Fault Dimensions, *J. Geoph. Res.*, **77**(20), 3788-3795.

Seed, H.B., C. Ugas and J. Lysmer (1976). Site Dependent Spectra for Earthquake Resistant Design, *Bull. Seism. Soc. Amer.*, **66**, 221-243.

Thatcher, W., and T.C. Hanks (1973). Source Parameters of Southern California Earthquakes, *J. Geoph. Res.*, **78**, 8547-8576.

Trifunac, M.D. (1991). Zero Baseline Correction of Strong-Motion Accelerograms, *Bull. Seism. Soc. Amer.*, **61**, 1201-1211.

Trifunac, M.D. (1972a). Stress Estimates for San Fernando, California Earthquake of February 9, 1971: Main Event and Thirteen Aftershocks, *Bull. Seism. Soc. Amer.*, **62**, 721-750.

Trifunac, M.D. (1972b). Tectonic Stress and Source Mechanism of the Imperial Valley, California Earthquake of 1940, *Bull. Seism. Soc. Amer.*, **62**, 1283-1302.

Trifunac, M.D. (1972c). A Note on Correction of Strong-Motion Accelerograms for Instrument Response, *Bull. Seism. Soc. Amer.*, **62**, 401-409.

Trifunac, M.D. (1973). Analysis of Strong Earthquake Ground Motion for Prediction of Response Spectra, *Int. J. of Earthquake Eng. and Struct. Dynam.*, **2**(1), 59-69.

Trifunac, M.D. (1974). A Three-Dimensional Dislocation Model for the San Fernando, California, Earthquake of February 9, 1971, *Bull. Seism. Soc. Amer.*, **64**, 149-172.

Trifunac, M.D. (1976a). Preliminary Empirical Model for Scaling Fourier Amplitude Spectra of Strong Ground Acceleration in Terms of Earthquake Magnitude, Source to Station Distance and Recording Site Conditions, *Bull. Seism. Soc. Amer.*, **66**, 1343-1373.

Trifunac, M.D. (1976b). Preliminary Analysis of the Peaks of Strong Earthquake Ground Motion-Dependence of Peaks on Earthquake Magnitude, Epicentral Distance and the Recording Site Conditions, *Bull. Seism. Soc. Amer.*, **66**, 189-219.

Trifunac, M.D. (1989a). Dependence of Fourier spectrum Amplitudes of Recorded Strong Earthquake Accelerations on Magnitude, Local Soil Conditions and On Depth of Sediments, *Int. J. Earthquake Eng. and Struct. Dynam.*, **18**, 999-1016.

Trifunac, M.D. (1989b). Empirical Scaling of fourier Spectrum Amplitudes of Recorded Strong Earthquake Accelerations in Terms of Magnitude and Local Soil and Geologic Conditions, *Earthquake Eng. and Eng. Vibration*, **9**(2), 23-44.

Trifunac, M.D. (1990). How to Model Amplification of Strong Earthquake Motions by Local Soil and Geologic Site Conditions, *Int. J. Earthquake Eng. and Struc. Dynam.*, **19**(6), 833-846.

Trifunac, M.D. (1991). M_L^{SM}, *Int. J. Soil Dynam. and Earthquake Eng.*, **10**(1), 17-25.

Trifunac, M.D. and A.G. Brady (1975). On the Correlation of Seismic Intensity Scales with the Peaks of Recorded Strong Ground Motion, *Bull. Seism. Soc. Amer.*, **65**, 139-162.

Trifunac, M.D. and D.E. Hudson (1970). Laboratory Evaluation and Instrument Corrections of Strong Motion Accelerographs, Earthquake Engineering Research Laboratory, EERL 70-04, California Institute of Technology, Pasadena.

Trifunac, M.D. and V.W. Lee (1985). Preliminary Empirical Model for Scaling fourier Amplitude Spectra of Strong Ground Acceleration in Terms of Earthquake Magnitude Source to Station Distance, Site Intensity and Recording Site Conditions: Second Paper, with V.W. Lee, Department of Civil Engineering, Report No. 85-03. University of Southern Calif., Los Angeles, California.

Trifunac, M.D. and V.W. Lee (1987). Direct Empirical scaling of Response Spectral Amplitudes from Various Site and Earthquake Parameters, U.S. Nuclear Regulatory Commission, Report NUREG/CR-4903, Vol 1.

Trifunac, M.D. and V.W. Lee (1989). Empirical Models for Scaling Fourier Amplitude Spectra of Strong Ground Acceleration in Terms of Earthquake Magnitude, Source to Station Distance, Site Intensity and Recording Site Conditions, *Int. J. Soil Dynam. and Earthquake Eng.*, **8**(3), 110-125.

Trifunac, M.D. and V.W. Lee (1990). Frequency Dependent Attenuation of Strong Earthquake Ground Motion, *Int. J. Soil Dynam. and Earthquake Eng.*, **9**(1), 3-15.

Trifunac, M.D. and F.E. Udwadia (1974). Parkfield, California, Earthquake of June 27, 1966: A Three-Dimensional Moving Dislocation, *Bull. Seism. Soc. Amer.*, **64**, 511-533.

Wyss, M. and J.N. Brune (1968). Seismic Moment, Stress and Source Dimensions for Earthquakes in California – Nevada Region, *J. Geophys. Res.*, **73**, 4681-4694.

IV. Q AND HIGH FREQUENCY STRONG MOTION SPECTRA

Empirical scaling equations for Fourier Amplitude Spectra of strong ground motion are used to describe A_Q and k in the assumed (high frequency) shape of strong motion amplitudes: $FS(f) = A_Q^{-\pi kf}$. The results show (1) excellent agreement of the computed A_Q and k with other independent estimates, (2) smooth decay of strong motion spectral amplitudes for $f > 25$ Hz, without an abrupt low-pass filtering of the high frequencies, and (3) excellent agreement with other estimates of the regionally specific attenuation of high frequency seismic waves.

As the strong earthquake shaking in the western United States typically samples only the shallow (< 10 km) and local (< 100 km) characteristics of wave attenuation, the recorded strong motion accelerograms can be used as the most direct means of describing the nature of the high frequency attenuation of the entire strong motion signal. *Lg* and coda wave studies to estimate Q may sample different volume of the crust surrounding the station, and involve different paths of the waves. These differences must be carefully documented and understood before the results can be used in earthquake engineering characterization of strong motion amplitudes.

IV.1 INTRODUCTION

The high frequency Fourier spectrum amplitudes of strong motion acceleration for frequencies $f > v/r$ (where v is the dislocation velocity and r the smallest relevant source dimension), in linear elastic homogeneous and isotopic medium are expected to be proportional to $\sigma\beta/\mu$, where σ designates the stress drop and β and μ are the shear wave velocity and material rigidity in the region surrounding the earthquake (Brune, 1970). In the real earth, this spectrum is low-pass filtered by a combination of physical factors (scattering, diffraction, inelastic attenuation, nonlinear source and transmission phenomena). For frequencies typically higher than 1 to 10 Hz, this attenuation dominates the spectral amplitudes of recorded strong motion acceleration (Trifunac, 1973).

Several authors suggest the existence of high frequency "corner" (or cut-off) (Hanks, 1982), where the spectra of accelerograms recorded at close distances "crash" abruptly to progressively smaller amplitudes. Papageorgiou and Aki (1983a,b) and Papageorgiou (1988) attribute this to a source effect, which is caused by a non-linear zone at the edge of the crack, of dimension d, acting as a low-pass filter, with corner frequency $f_{\max} \sim v/d$. Anderson and Haugh (1984) show that if the logarithm of the spectral amplitudes is plotted versus frequency on a linear scale, this "corner" disappears and the spectral amplitudes decay linearly as in $e^{-\pi kf}$, until the recording and processing noise take over. The factor $k = \Delta/(Q\beta)$ is inversely proportional to the quality factor Q and velocity β integrated along the propagation path of length Δ (Cormier, 1982).

For frequencies higher than $\sim$ 10 Hz, the recorded accelerograms are distorted by the accelerograph transfer function (Trifunac and Hudson, 1970; Novikova and Trifunac,

1991), and must be corrected for the instrument response (Trifunac, 1971; 1972; Amini and Trifunac, 1985; Amini et al., 1982, 1991; Wong and Trifunac, 1977; Novikova and Trifunac, 1992). This correction is feasible as long as the signal to noise ratio is significantly larger than one, and, so, it depends on the size of the earthquake and on the recording distance (Amini et al., 1982; 1987). The typical accuracy of the high frequency instrument correction is such that the high frequency strong motion can be reproduced for frequencies well beyond the nominal recording range of the recording transducers (Lee and Trifunac, 1974) but, for practical reasons mainly related to the need to control the volume of the data storage, it was decided in the late 1960's to preserve the strong motion data up to 25 Hz only (50 points per second, Lee and Trifunac, 1982; 1987; 1990).

The purpose of this chapter is to summarize the observed nature of the high frequencies of the Fourier amplitude spectra of strong motion acceleration. In contrast to the previous studies (Anderson, 1991), we will not analyze selected accelerograms, but will use empirical equations for prediction of strong motion spectral amplitudes, to determine the nature of the high frequency attenuation. The consequence of this approach is that the fluctuations associated with individual recordings will be "smoothed out" via regression analyses, and so the overall average and regional picture may emerge. We will compare the results with other seismological inferences and will show that these are usually in good agreement. Also, in this work, the Fourier amplitude spectra of the complete strong motion signal will be used, rather than spectra of body or of surface waves. This is necessary for engineering characterization of strong ground motion. Various other studies of the high frequency attenuation and of Q use many different parts of the recorded motion (body waves, surface waves, coda) at small and at large distances. In this work, we will consider the strong ground motion recorded mainly in California, at distances typically less than 100 km, and for frequencies between $\sim$ 5 Hz and 25 Hz.

For short epicentral distances, the attenuation at depths less than $\sim$ 5 km may overshadow the attenuation along the deeper portions of the crust. For understanding and for prediction of strong motion amplitudes, it is thus necessary to know how Q changes with depth and with frequency. This requires higher space and time resolution than what is available from distant recordings, but, by averaging the results over representative depth, the inferences on shallow Q structure based on strong motion data, can be interpreted and compared with other surface wave and coda wave studies.

In this study, we will take the advantage of (1) small epicentral distances, (2) shallow sources and (3) high frequency strong motion acceleration data, to estimate Q near the surface, and only locally near the source. More distant seismological measurements are usually based on specific wave forms (e.g. Lg, Chun et al., 1987; Gupta and McLanghlin, 1987), or may use coda waves (e.g. Singh and Herrmann, 1983; Woodgold, 1990) and thus sample larger volume of the crust and along different rays. Since Q may change rapidly with depth and laterally, we must develop procedures to map Q in three-dimensions and for small epicentral distances. This will then allow improved estimation of strong motion amplitudes for earthquake engineering applications.

In what follows, we will study the amplitudes of $FS(T)$ for high frequencies $f > 5$ Hz, and will consider strong motion amplitudes for epicentral distance less than $\sim$ 100 km.

IV.2 HIGH FREQUENCY SPECTRA

Little observational work has been done on high frequency ($f > 25$ Hz) attenuation of strong motion data. Until recently, most of the recording instruments could register only moderately high frequencies (say < 30 Hz). Routine processing of strong motion data has been performed up to 25 Hz (50 Hz sampling rate, Fig. 26) even though the typical analog records are of good quality, so that we could have extracted even higher frequencies (perhaps up to 35 or 40 Hz). The main obstacle in understanding the attenuation of high frequencies is the lack of data on the irregularities in the earth's crust, and the relatively large distances separating the source and the strong motion recording stations. We could saturate some areas with broad band strong-motion instruments, but it is not likely that we will be able to describe the three-dimensional inhomogeneities in the earth's crust for some time. Furthermore the current computational capabilities to model scattering and diffraction for very high frequencies (short waves) are still very limited (e.g. Todorovska and Lee, 1990; 1991). Thus, most investigators continue to use the empirical description for the combined effects of inelastic and scattering attenuations in the form $\exp(-\omega\Delta^*/2Q\beta)$, where Δ^* is the distance traveled by the wave, Q is the quality "constant" and β is the (shear) wave velocity. For granites and basalts, Q is in the range of thousands, but for near surface soil and sediments it can be as low as 10. Recent results on the variation of Q through the central United States have been presented by Michell and Hwang (1987). They show Q values increasing from about 1000 to 5000 for depths between 0 and 50 km in the central United States. For the western United States, their models suggest Q between 150 and 300 at a frequency of about 1 Hz. For sediments, typical results from several studies suggest low surface Q's, in the range from 10 to 50, increasing to 25 to 100 between 500 m and 2 km (e.g. Baker and Stevens, 1983; McDonal et al., 1958; Ganley and Kanasevich, 1980; Hauge, 1981; Johnson and Silva, 1981; Joyner et al., 1976; Malin and Walker, 1985; Singh et al., 1982; Tullos and Reid, 1969).

We will approximate the high frequency spectral amplitudes by $FS(f) = A_Q e^{-\pi k f}$ (Trifunac, 1973; Anderson and Hough, 1984). Using two frequencies, f_l and f_r, both larger than the frequency corresponding to the peak of the spectral amplitudes (f_p in Fig. 26), one can compute k and A_Q from

$$k = \frac{\ln FS(f_r) - \ln FS(f_l)}{\pi(f_l - f_r)} \tag{57}$$

and

$$A_Q = FS(f_l)e^{\pi k f_l}. \tag{58}$$

In Figs. 27a and 27b, we plot k averaged for the models 3 and 4 from the G4RM. k changes little with respect to magnitude and, so, in these figures, this effect is averaged

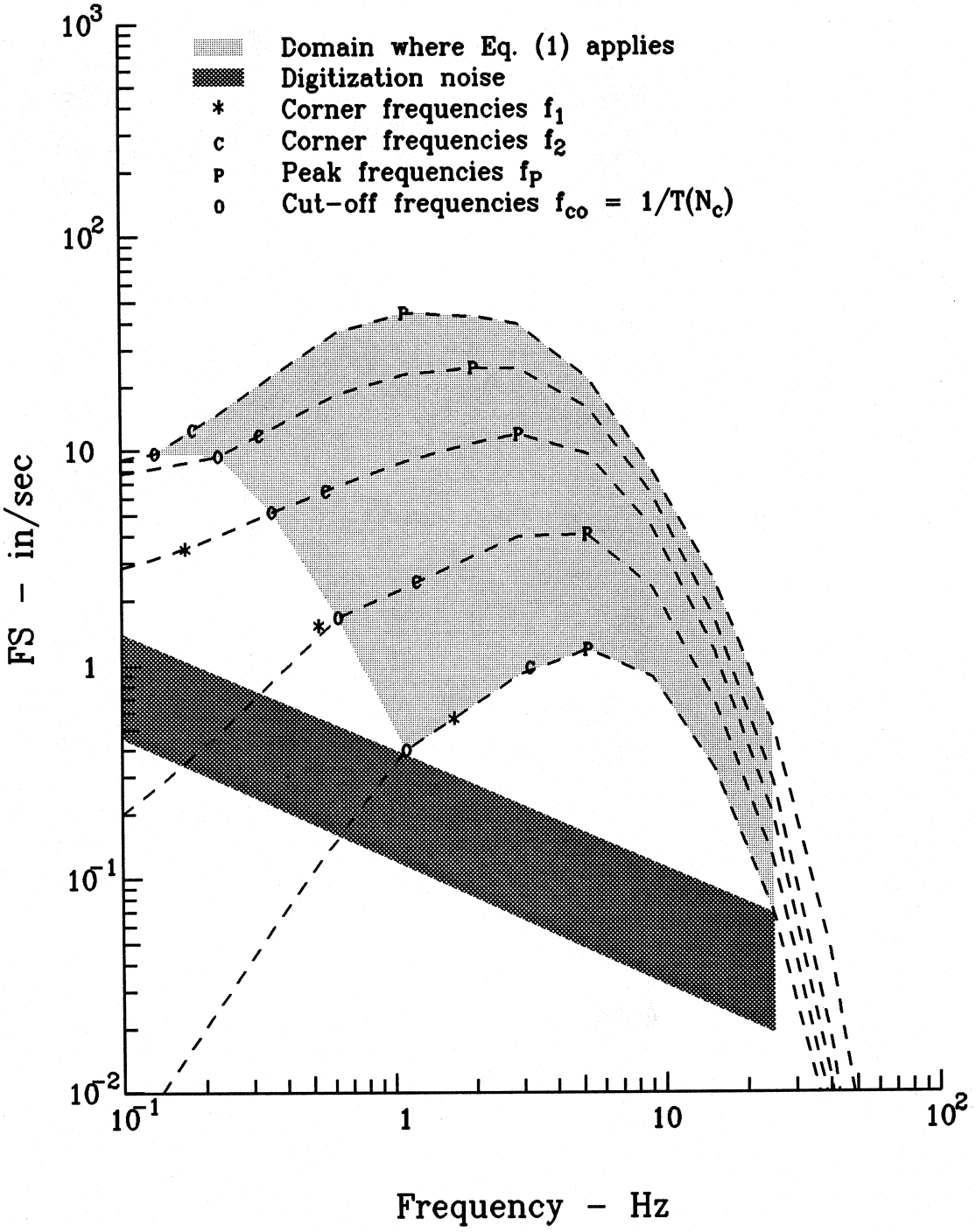

Fig. 26 Fourier amplitude spectra (in/sec), versus frequency (Hz) for probability of exceedance equal to 0.5, for $M = 4, 5, 6, 7$ and 8 (bottom to top), at epicentral distance $R = 10$ km, and for a source at depth $H = 0$ km. Outside the shaded region, between $f_{co} = 1/T(N_c)$ and $f = 25$ Hz, where Eq. (1) is valid, the spectral amplitudes (dashed lines) can be extrapolated as it is proposed in this paper. Corner frequencies f_1, f_2, and the cut off frequencies f_{co} are defined in the text. The processing and digitization noise amplitudes are shown by the shaded zone increasing from $FS \sim 10^{-1}$ to $FS \sim 1$ for frequencies decreasing from 10 to .1 Hz.

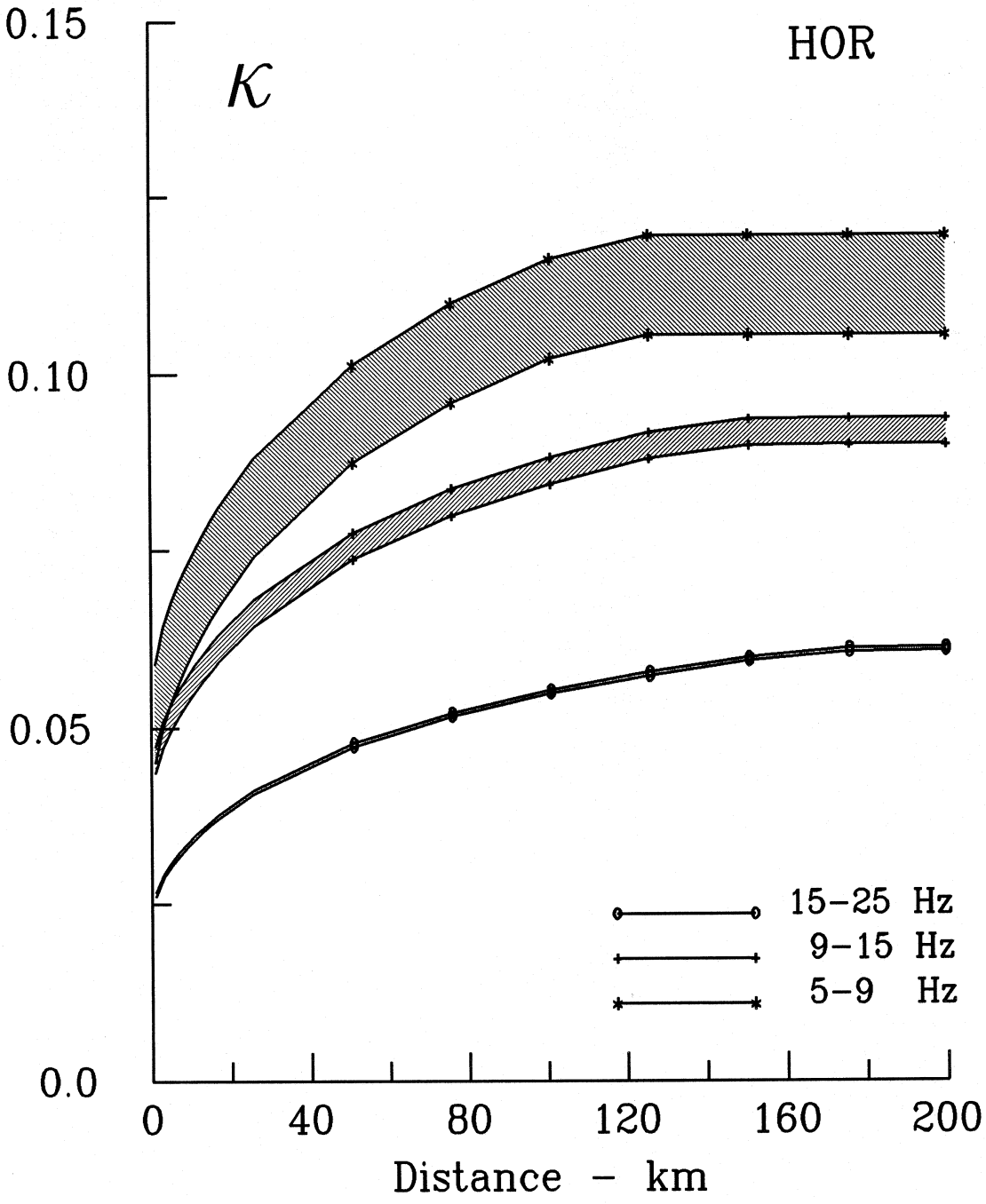

Fig. 27a $k = \Delta/(Q\beta)$ versus Δ (km), for three frequency bands (5.3 - 9.1) (9.1 - 15.4), and (15.4 - 25.), for horizontal motion, and for models 3 and 4 from the G4RM. The shaded zones outline the fluctuations caused by the local soil and local geologic site conditions.

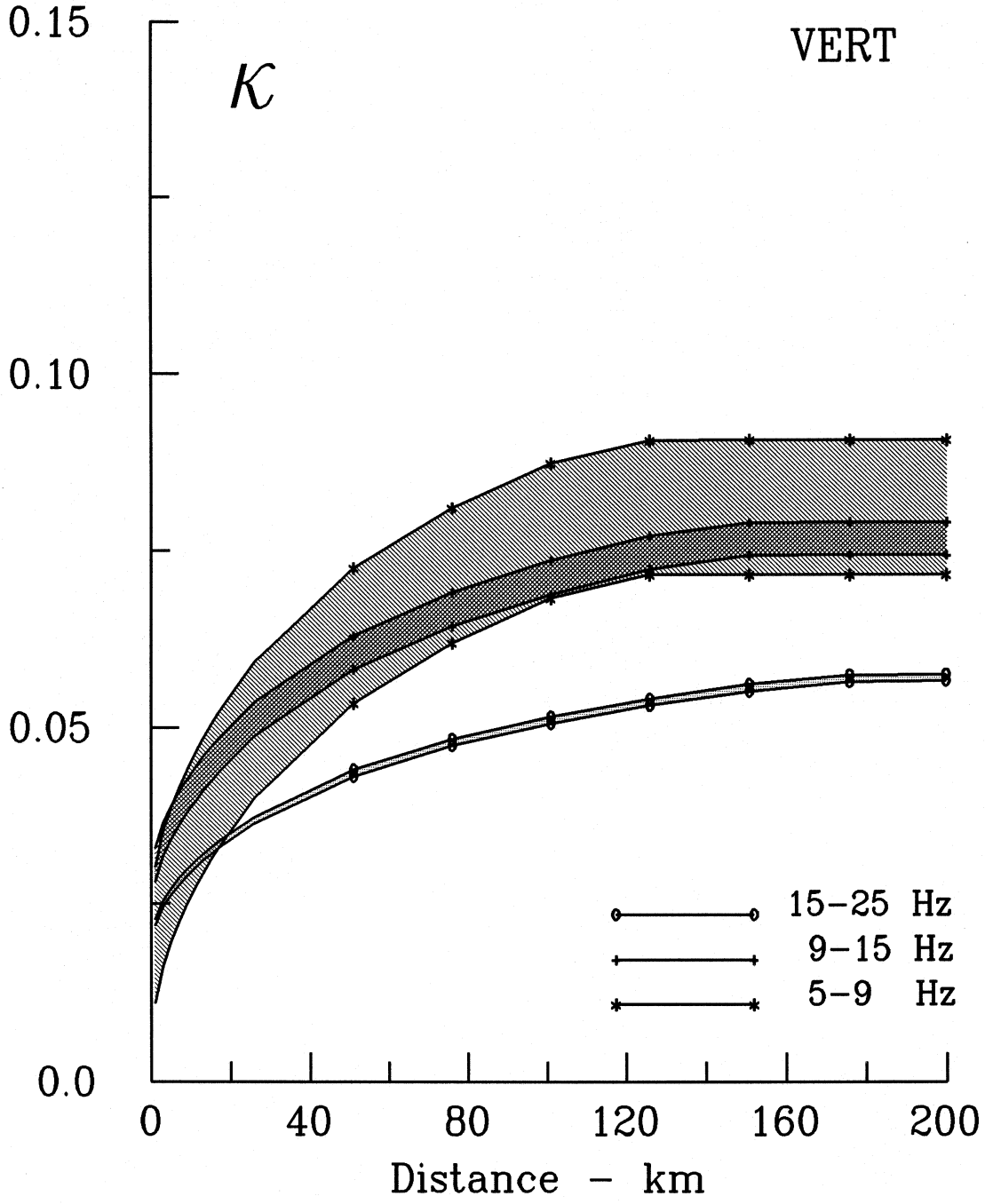

Fig. 27b $k = \Delta/(Q\beta)$ versus Δ (km), for three frequency bands (5.3 - 9.1) (9.1 - 15.4), and (15.4 - 25.), for vertical motion, and for models 3 and 4 from the G4RM. The shaded zones outline the fluctuations caused by the local soil and local geologic site conditions.

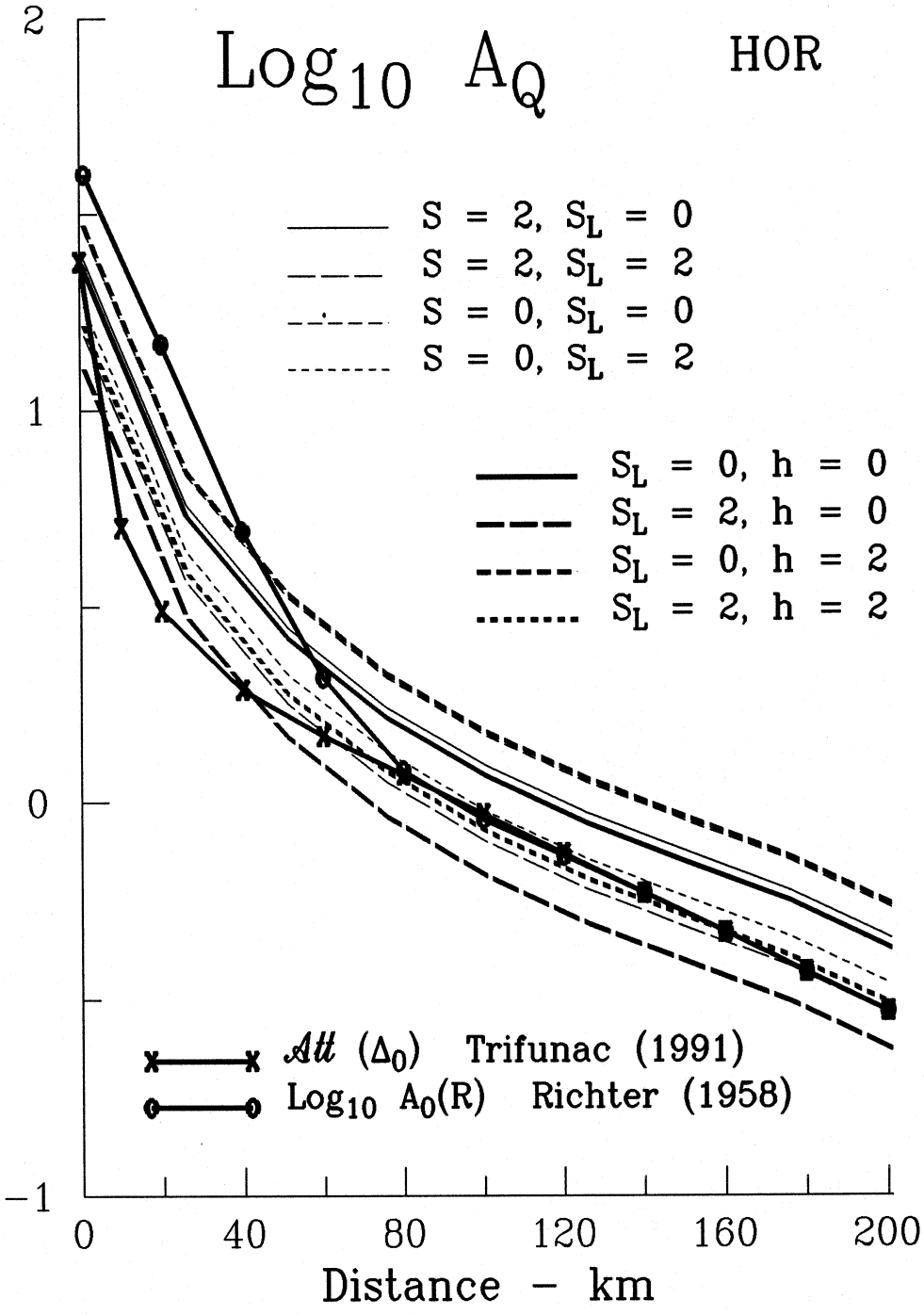

Fig. 28a $\log_{10} A_Q$ versus Δ (km), for $M = 6$, probability of exceedance $p = 0.5$, for horizontal motion and for different local soil (s_L) and geologic (s) site conditions. The Richter (1958) attenuation equation $\log_{10} A_0(R)$, where R is epicentral distance, and the Trifunac (1991) attenuation equation $Att(\Delta_0)$ with $\Delta_0 = (R^2 + H^2)^{1/2}$, both with an arbitrary vertical scale, are shown for comparison.

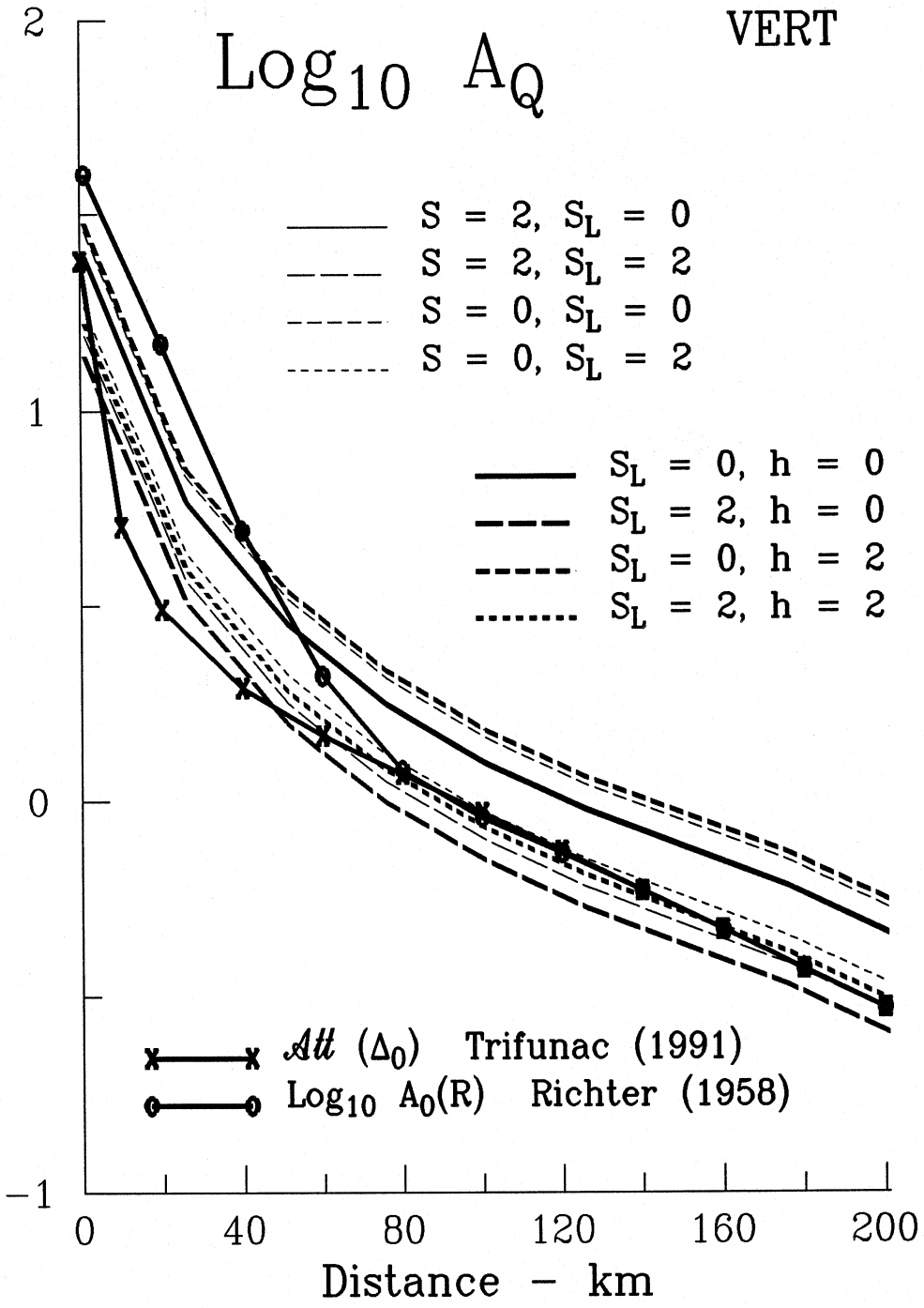

Fig. 28b $\log_{10} A_Q$ versus Δ (km), for $M = 6$, probability of exceedance $p = 0.5$, for vertical motion and for different local soil (s_L) and geologic (s) site conditions. The Richter (1958) attenuation equation $\log_{10} A_0(R)$, where R is epicentral distance, and the Trifunac (1991) attenuation equation $Att(\Delta_0)$ with $\Delta_0 = (R^2 + H^2)^{1/2}$, both with an arbitrary vertical scale, are shown for comparison.

Table VIII

A_Q^* at $R = 100$ km

Horizontal/vertical	$s_L = 0$	$s_L = 2$
$h = 2$ km	1.51/1.52	.85/.85
h= 0 km	1.16/1.26	.65/.70

	$s_L = 0$	$s_L = 2$
$s = 0$	1.48/1.45	.95/.93
$s = 2$	1.24/1.24	.79/.79

* $M = 6, \quad p = 0.5 \quad H = 0$ km

for $M = 5$ and 6. k also changes little in going from $s = 0$ to 2 and from $s_L = 0$ to 2. To display the frequency dependence of k, three bands are shown for the three pairs of (f_l, f_r), equal to (5.3, 9.1), (9.1, 15.4) and (15.4, 25.). k increases with distance (for the examples shown, it is assumed that the source is at the surface, $H = 0$), and asymptotically approaches a constant level for distance $\sim$ 100 km. Comparison of our results with selected estimates of k for sites in southern California (e.g. Hough et al., 1988) shows good agreement of the amplitudes and of the shape of k versus distance, computed for selected strong motion data.

The amplitudes of the high frequency spectra are determined by the zero frequency asymptote, A_Q, in Eq. (58). A_Q depends on the earthquake magnitude, hypocentral distance Δ, and the local soil and geologic site conditions. To illustrate its behavior with respect to the epicentral distance, Figs. 28a and 28b show A_Q for $M = 6$, $p = 0.5$, R between 0 and 200 km ($H = 0$), $s = 0$ and 2, $h = 0$ and 2 km and $s_L = 0$ and 2. As a function of R, the shape of A_Q should be close to the family of attenuation equations describing peak accelerations (e.g., Trifunac, 1976b), to the Richter's attenuation law used in estimation of local magnitude, $\log_{10} A_0(R)$ (Richter, 1958), and to our attenuation function $\mathcal{A}tt(\Delta_0)$ used in computation of the strong motion magnitude M_L^{SM} (Trifunac, 1991). It is seen from Figs. 28a and 28b that the slopes of $\log_{10} A_0(R)$ and of $\mathcal{A}tt(\Delta_0)$ are the same as for A_Q for distances greater than $\sim$ 80 km, but that $\mathcal{A}tt(\Delta_0)$ agrees better with A_Q for zero and small distances. Figs. 28a and 28b also show that for Models 3 and 4, A_Q is the smallest for sites on basement rock and for $s_L = 2$ (deep soil sites). It is largest in sediments ($s = 0$ or $h = 2$ km) and on "rock" soil sites ($s_L = 0$). Table VIII illustrates A_Q for $R = 100$ km. The amplitudes of A_Q increase by a factor between 1.5 and 2 in going from $s = 2$ to $s = 0$ (or from $h = 0$ to $h = 2$ km). At deep soil sites, A_Q is reduced by a factor in the range from 2 to 3, relative to the "rock" sites ($s_L = 0$).

IV.3 AVERAGE QUALITY FACTOR Q

Since $k = \Delta/(Q\beta)$ (for shear wave content of the strong motion), using k in Figs. 27a and 27b and estimating β, one can compute Q as a function of distance, Δ, and frequency. Fig. 29 shows Q^{-1} computed in this way for distances equal to 1, 26, 51 and 76 km, together with other but different estimates of Q^{-1} in California (Cormier, 1982). To compute Q from k, we assumed that the average velocity β is equal to 3.35 + 0.00175 Δ, which approximates the average travel times for S waves in southern California (Richter, 1958), and where Δ (< 200 km) is the hypocentral distance. Also, we have assumed here that $\Delta \approx \Delta^*$, where Δ^* is the distance traveled by the waves.

Figs. 30a and 30b show Q plotted versus distance, Δ, for Models 3 and 4 in the G4RM. To reduce clutter, but to illustrate how Q changes with frequency, and with s and s_L, we averaged the Q estimates for $M = 5$ and 6 and for Models 3 and 4. The label $s = 0$ represents the average result for $s = 0$ and $h = 2$ km, and where $s = 2$ stands for $s = 2$ or $h = 0$ km. At high frequencies (15.4, 25.) Hz, the site effects appear to be insignificant. For lower frequencies, (5.3, 9.1) and (9.1, 15.4) Hz, there is more variation

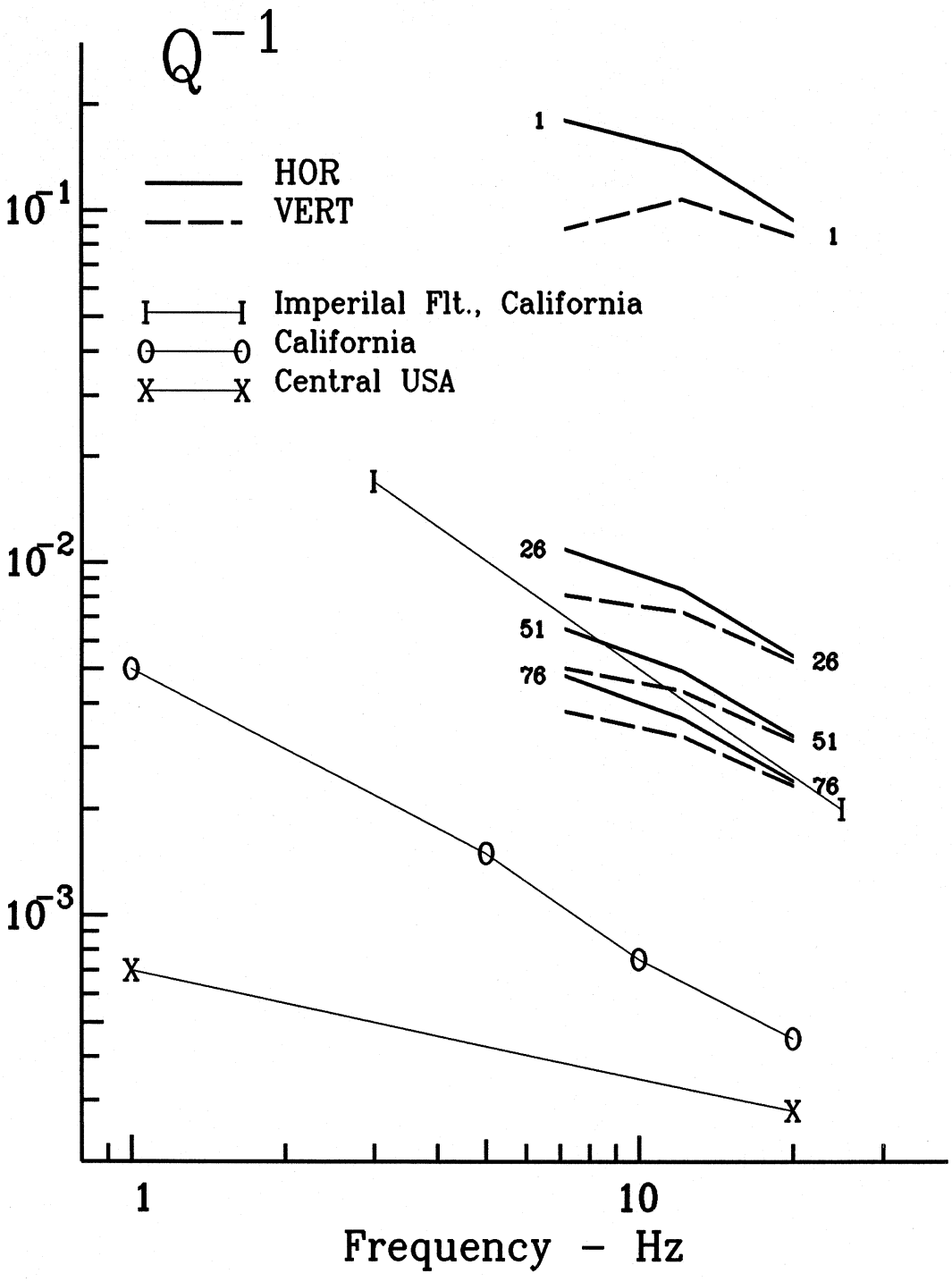

Fig. 29 Q^{-1} versus frequency, for distances equal to 1, 26, 51, and 76 km, compared with selected other estimates (Cormier, 1982).

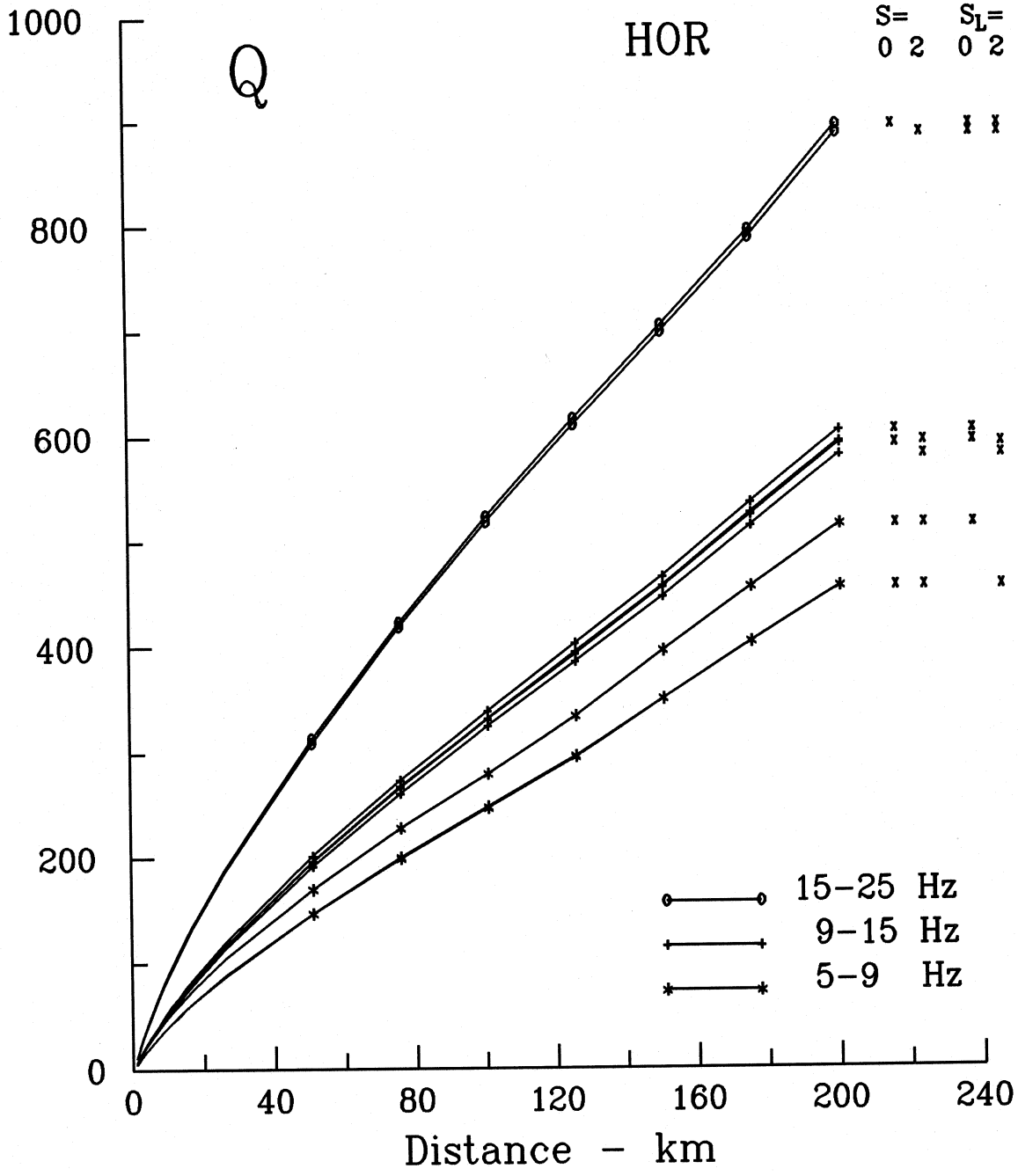

Fig. 30a Q versus Δ (km), for three frequency bands, and for horizontal motion. For each curve (note that many curves overalap), the corresponding local geologic ($s = 0$ and 2, first and second column) and local soil ($s_L = 0$ and 2, third and fourth column) site conditions are identified by an "x" placed in the corresponding columns at the same level and next to the right most point of the curve.

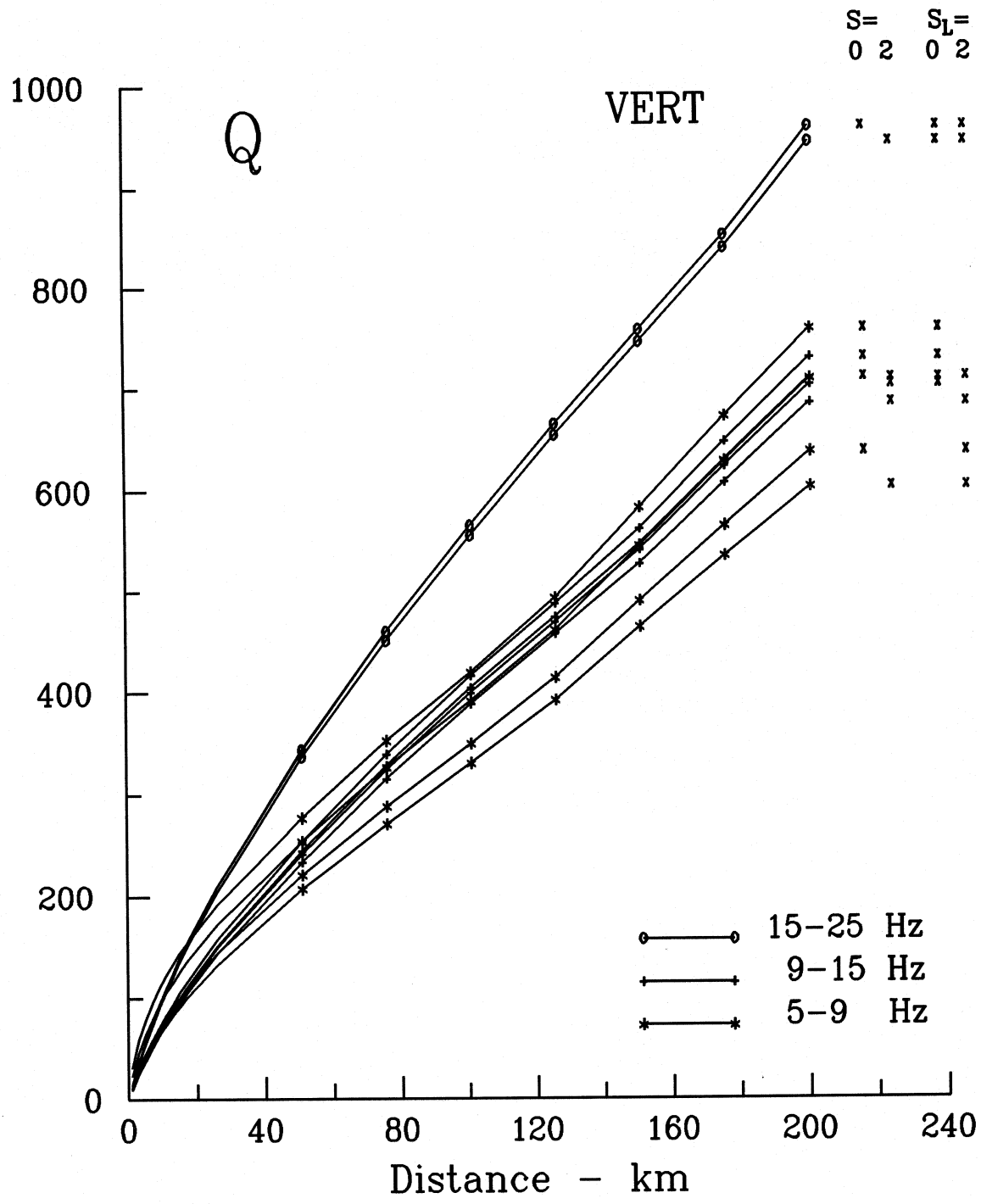

Fig. 30b Q versus Δ (km), for three frequency bands, and for vertical motion. For each curve (note that many curves overalap), the corresponding local geologic ($s = 0$ and 2, first and second column) and local soil ($s_L = 0$ and 2, third and fourth column) site conditions are identified by an "x" placed in the corresponding columns at the same level and next to the right most point of the curve.

with site conditions. The local site condition s_L seems to result in high Q on "rock" sites ($s_L = 0$). However, because of all other simplifying assumptions, these variations cannot be taken as significant. The only clear and distinct trend that is seen in Figs. 30a and 30b is the frequency dependent slope of Q versus distance.

The changes of Q with Δ are almost linear for broad intervals of Δ, and thus the average Q can be approximated by

$$\overline{Q} = a_Q + b_0 \Delta, \tag{59}$$

using two segments, say one for $0 < \Delta < 20$ km and the other for $20 < \Delta < 200$ km. Table IX summarizes a_Q and b_0 for horizontal and for vertical ground motion.

Inversion of data on average k or Q versus distance, to determine Q variations with depth, requires detailed description of the velocity of waves versus depth, and careful separation of the recorded motion into body and surface waves (e.g. Hough and Anderson, 1988). Our estimates of k and Q however are different, since we use empirical description of spectral amplitudes of the entire strong motion signal, thus arriving at the overall "average" values of these parameters. The resulting estimates of k and Q lead to so simple functional forms, that one can consider a simplified representation, to further interpret this data. Thus, we assume that it is possible to approximate the velocity structure by a linear dependence on depth, (Fig. 31) by

$$v(y) = v_0 + v_1(y - d), \quad y \geq d. \tag{60}$$

For shallow depths (short distances, $0 < \Delta < 20$), we will assume $v_0 = 1$ km/sec and $v_1 = .25$/sec. This may be typical of the Los Angeles basin, where many accelerograms in our data base have been recorded during San Fernando, 1971 earthquake, or of Imperial Valley near El Centro site, which also contributed many strong motion accelerograms. For a deeper structure (and for larger distances, $20 < \Delta < 100$ km), we will consider $v_0 = 2$ km/sec and $v_1 = .04$/sec.

For linearly increasing velocity, the ray path of body waves is defined by a circle of radius R_0, centered at $d = v_0/v_1$ above the surface (Fig. 31). For the source and the recording station both on the surface, the circular path has length $R_0\pi\varphi_0/180°$, where $\varphi_0 = 180° - 2\theta_Q$ (Fig. 31) and $\Delta = 2R_0 \cos\theta_Q$. In what follows, we will assume approximately that all strong motion waves collectively sample Q uniformly inside the circle $x^2 + y^2 = R_0^2$, for $-\Delta/2 < x < \Delta/2$ and for $d < y < (R^2 - x^2)^{1/2}$. Relative to the coordinate system (x, y), assuming that Q increases as a linear function of depth, we write $Q = a_1 + by_1$, for $y \geq d$ or $Q = g_0 + g_1(y - d)$, for $y \geq d$, with $a_1 = g_0 - g_1 d$ and $b_1 = g_1$. The average Q inside the circle in Fig. 31 is then equal to

$$Q_{Av} = a_1 + b_1 \Delta \frac{\cos^2\theta_Q}{3\left[\frac{\pi}{2} - \frac{\sin 2\theta_Q}{2} - \theta_Q\right]}. \tag{61}$$

The function $\cos^2\theta_Q / \left[3\left(\frac{\pi}{2} - \frac{\sin 2\theta_Q}{2} - \theta_Q\right)\right]$ increases at first slowly from .212 at $\theta_Q = 0$ to about 1 for $\theta_Q \sim \pi/3$ and then, as $\theta_Q \to \pi/2$, grows like $2/(\pi/2 - \theta_Q)$.

Table IX

Coefficients in $\overline{Q} = a_0 + b_0\Delta$

		(5.3–9.1) Hz		(9.1–15.4) Hz		(15.4–25) Hz	
	distance (km)	a_0	b_0	a_0	b_0	a_0	b_0
horizontal motion	$0 < \Delta <\sim 20$	5.	3.45	5.	4.65	9.	8.
	$\sim 20 < \Delta < 200$	50.	2.15	60.	2.65	100.	4.10
vertical motion	$0 < \Delta <\sim 20$	18.	5.15	19.	5.6	40.	6.7
	$\sim 20 < \Delta < 200$	75.	2.78	100.	3.25	100.	4.43

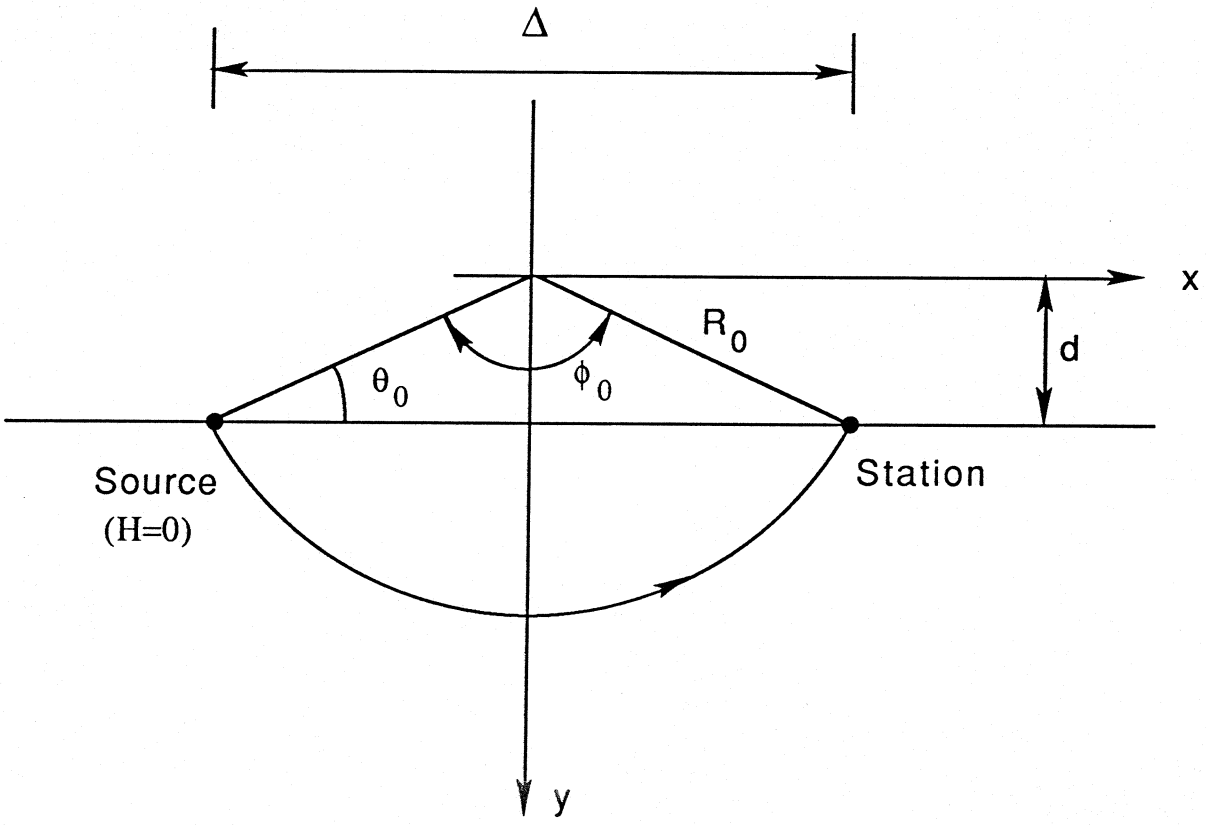

Fig. 31 Parameters of circular ray path, in the half space, $(y \geq d)$, with linear velocity structure $v(y) = v_0 + v_1(y - d)$, for a surface source $(H = 0)$.

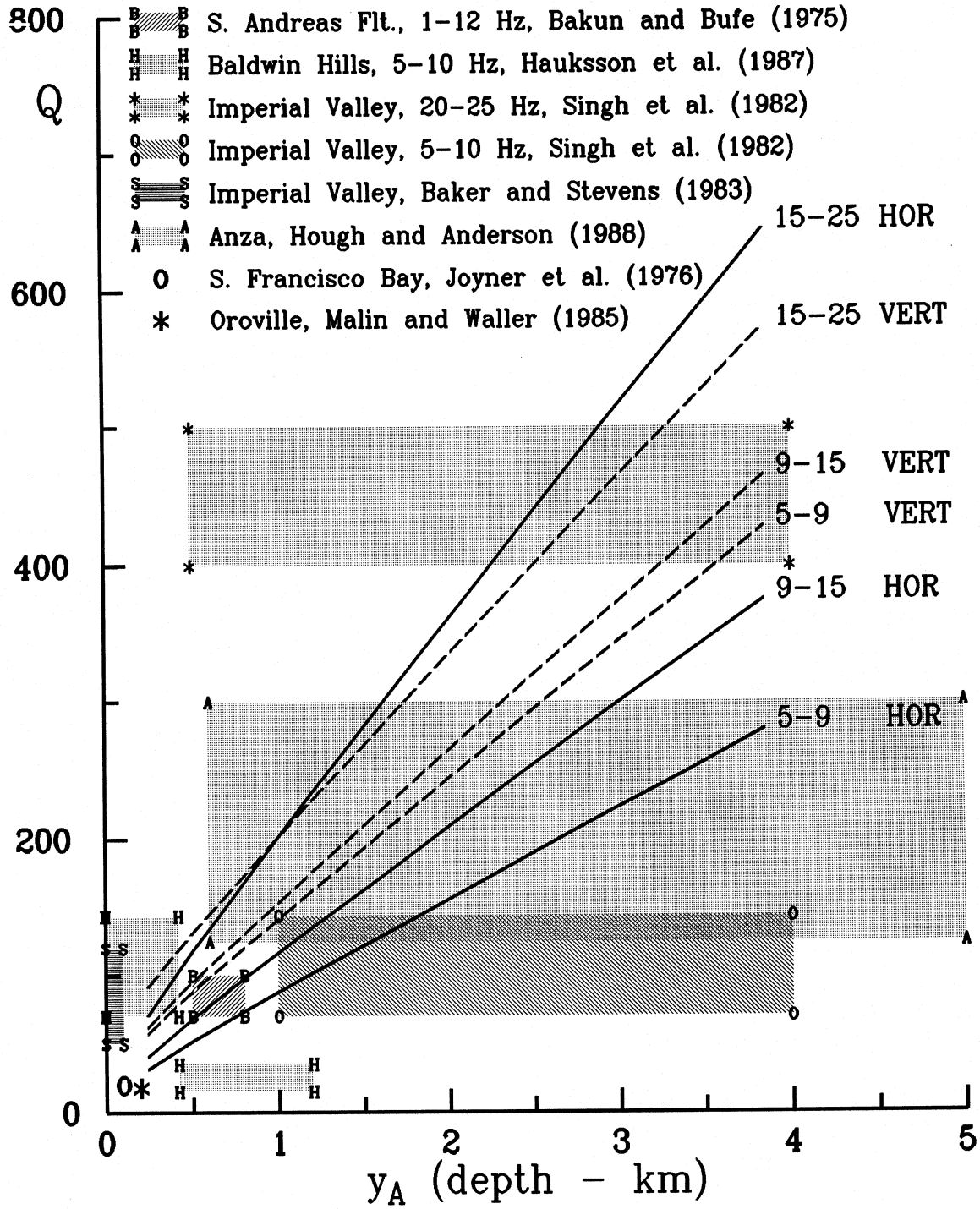

Fig. 32 Q_{Av} versus depth y_A. For comparison, different estimate of Q_s (based on shear waves) in California are shown also.

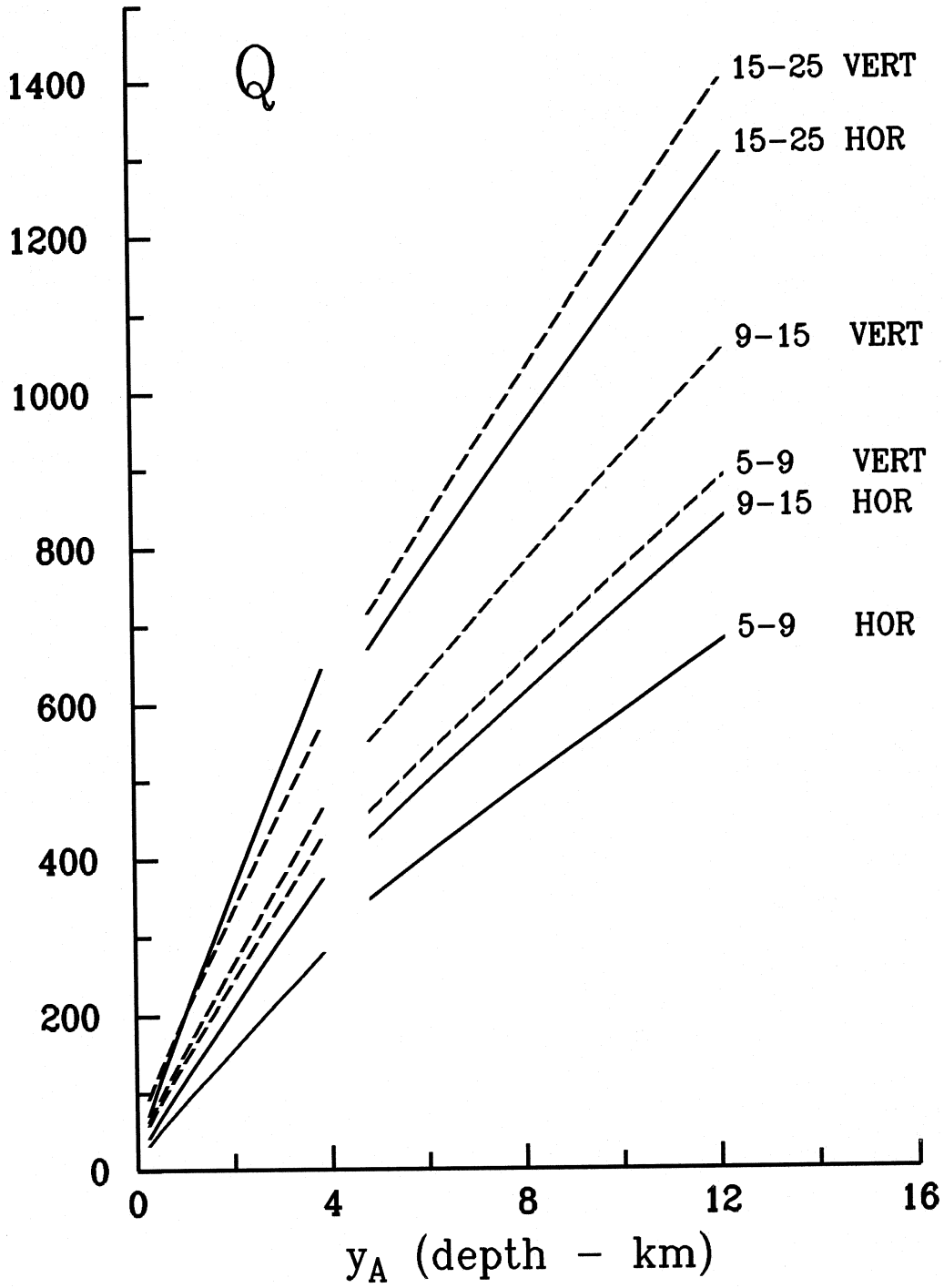

Fig. 33 Q_{Av} versus y_A.

Eqs. (59) and (61) can be combined to compute a_1 and b_1 and then g_0 and g_1, for a given Δ. Then, g_0 and g_1 can be used to compute Q_{Av} at some representative depth, say at $y_A = (R_0 - d)/2$. By repeating this process for successive Δ, one can arrive at estimates of Q versus y_A, which are shown in Fig. 32. For comparison, we also show the range of Q estimates for S waves for selected, but representative locations in California. In spite of the simplified and different nature of our and of these different estimates, and the differences in the wave types used, the agreement is good.

Fig. 33 shows a continuation of the Q estimates for $4 < y_A < 12$ km. In this second interval, we used $v_0 = 2$ km/sec and $v_1 = .04$/sec. With Δ less than about 100 km this approach allows estimation of Q for depths less than about $y_A = 12$ km. If the function $Q(y)$ is irregular or has large jumps, the above approach smooths those variations by fitting the best straight line and then estimating the average value of Q at some representative depth. For large jumps in Q, k versus Δ should become constant (when $Q \to \infty$) or suddenly increase (when $Q \to 0$), as the down going ray enters the layer with such Q values. For $\Delta \gtrsim 100$ km, k versus Δ for (5.3, 9.1) Hz becomes nearly constant (Fig. 27a,b). For a model consisting of parallel layers, this could be used to find the depth when Q jumps to higher values. However, since we study the attenuation of the entire strong motion signal, and not only of body waves, this distance of 100± km when k becomes nearly constant may also be associated with the horizontal dimensions of large sedimentary basins (e.g. Los Angeles, Imperial Valley), where high frequency strong motion surface waves should attenuate more than along paths which go through the basement rock. This interesting question is however beyond the scope of this brief study since it will require regional grouping of recorded accelerograms rather than the use of the overall k and Q, as used here, to represent the smooth trends of all strong motion data in the western United States.

IV.4 DISCUSSION AND CONCLUSION

Fourier Amplitude Spectra of the complete strong motion record can be characterized by $A_Q e^{-k\pi f}$ for $f > f_p$. A_Q and k (or $Q = \Delta/(k\beta)$) thus computed agree favorably with many other seismological estimates of the same quantities. Neither our empirical models of Fourier spectrum amplitudes (e.g. G4RM), nor the directly computed spectra of recorded strong motion indicate the existence of abrupt decay of spectral amplitudes in the sense of $f_{\max}$ (Hanks, 1982; Papageorgiou and Aki, 1983a,b). If some low-pass filtering effects (sharper than $e^{-\pi k f}$) exist, those must occur for $f > 25$ Hz, i.e. outside the range for which strong motion data is processed and achieved at present.

In the frequency band between 5 and 25 Hz, our results on Q are in good agreement with those of others, reported for the same region where the strong motion data has been recorded. These results give $Q \sim 10$ to 50 near the surface, increasing to about 300 to 500 at a depth of 4 km. The estimates of Q for vertical motion (with only one exception) are larger (by 5 to 20 percent) than the corresponding estimates for the horizontal motions. These differences diminish with increasing frequency, and for 25 Hz

become negligible. In all calculations we used the same velocity (β), for horizontal and for vertical motions. Assuming that for vertical motions the "representative" velocity is between $(\mu/\rho)^{1/2}$ and $[(\lambda+2\mu)/\rho]^{1/2}$ helps to explain the observed differences. At high frequencies, near and beyond 20 Hz, the same Q estimates for horizontal and vertical motions invite consideration of scattered waves, with about equal participation of S- and P-wave potentials, in both the horizontal and vertical direction. Near 10 Hz, $b_3(T)$ changes sign (see Table I), also implying that, for f near and larger than 10 Hz, the spectral amplitudes of horizontal and of vertical motions are about the same (between 1 and 3 Hz, horizontal motions are about two times larger than the vertical). At high frequencies ($f > 10$ Hz), $b_3(T)$ becomes positive, i.e. vertical spectral amplitudes become larger than the horizontal. Another explanation for the observed trends may be sought in the increased participation or recording, digitization and processing noise in the recorded high frequency signals exceeding $\sim$ 10 Hz. Obviously, more detailed investigation will be required to explain all these trends in a unique and consistent way.

Since 1970, we have been processing strong motion data up to 25 Hz. This choice was governed by the characteristics of older strong motion accelerographs and their transfer functions (Lee and Trifunac, 1974; Amini et al., 1982, 1987). Currently used transducers (Amini and Trifunac, 1985; Amini et al., 1991) would allow extending this frequency limit to 50 Hz, but this would probably not alter much the overall quality and the information, contained in the processed strong motion data. For significant new information, it may be necessary to extract strong motion data up to, say, 100 Hz. Though this is technically feasible, it is not likely that this can be realized at the level of national and world wide strong motion networks in the near future. So, we must devise more detailed and ingenious analyses to infer the high frequency characteristics of strong ground motion by extrapolation from the presently available data.

Assuming the simple functional form $Q = Q_0 f^{\gamma}$ to describe Q versus frequency f, our study leads to $\gamma \sim .4$ (horizontal motions) and $\gamma \sim .2$ (vertical motions), for frequencies between 5.3 and 9.1 Hz, and to $\gamma \sim .7$ (horizontal) and $\gamma \sim .6$ (vertical), for frequencies between 15.4 and 25 Hz, and for the distance range from 25 to 75 km (Fig. 29).

Seismological studies of the frequency dependent Q (using Lg and coda waves) give $\gamma \sim .1$ to .3 for the central and south-eastern United States, $\gamma \sim .3$ to .4 for north-earthen U.S. and $\gamma \sim .4$ to .8 for the western U.S. (e.g. Singh and Herrmann, 1983).

IV.5 REFERENCES

Amini, A., V.W. Lee and M.D. Trifunac (1982). Noise in Earthquake Accelerograms, *ASCE, EMD*, **108**, 1121-1129.

Amini, A., R.L. Nigbor and M.D. Trifunac (1987). A Note on the Noise Amplitudes in Some Strong Motion Accelerographs, *Soil Dynam. and Earthquake Eng.*. **6**(3), 180-185.

Amini, A. and M.D. Trifunac (1985). Analysis of Force Balance Accelerometer, *Soil Dynam. and Earthquake Eng.*, **4**(2), 82-90.

Amini, A., O. Hata and M.D. Trifunac (1991). Experimental Analysis of RJL-1 Force Balance Accelerometer, *Earthquake Eng. and Eng. Vibration*, **11**(1), 77-88.

Anderson, J.G. (1991). Strong Motion Seismology, in Contributions in Seismology, AGU, Washington, D.C.

Anderson, J.G. and S.E. Hough (1984). A Model for the Shape of the Fourier Amplitude Spectrum of Acceleration at High Frequencies, *Bull. Seism. Soc. Amer.*, **74**, 1969-1993.

Barker, T.G. and J.L. Stevens (1983). Shallow Shear Wave Velocity and Q Structures at the El Centro Strong Motion Accelerograph Array, *Geophys. Res. Lett.*, **10**, 853-856.

Brune, J.N. (1970). Tectonic Stress and the Spectra of Seismic Shear Waves, *J. Geophys. Res.*, **75**, 4997-5009.

Chun, K.Y., G.W. West, R.J. Kokoski, and C. Sampson (1987). A Novel Technique for Measuring Lg Attenuation – Results from Eastern Canada Between 1 to 10 Hz, *Bull. Seism. Soc. Amer.*, **77**(2), 398-419.

Cormier, V.F. (1982). The Effect of Attenuation on Seismic Body Waves, *Bull. Seism. Soc. Amer.*, **72**, S169-S200.

Ganley, D.C. and E.R. Kanasevich (1980). Measurement of Absorption and Dispersion from Check Shot Surveys, *J. Geophys. Res.*, **85**, 5219-5226.

Gupta, I.N. and K.L. McLaughlin (1987). Attenuation of Ground Motion in the Eastern United States, *Bull Seism. Soc. Amer.*, **77**(2), 366-383.

Gusev, A.A. (1983). Descriptive Statistical Model of Earthquake Source Radiation and its Application to an Estimation of Short-Period Strong Motion, *Geophy. J. R. Astr. Soc.*, **74**, 787-808.

Hanks, T.C. (1982). $f_{\max}$, *Bull. Seism. Soc. Amer.*, **72**(6), 1867-1879.

Hauge, P.S. (1981). Measurements of Attenuation from Vertical Seismic Profiles, *Geophysics*, **46**, 1548-1558.

Hough, S.E., J.G. Anderson, J. Brune, F. Vernon, II, J. Berger, J. Fletcher, L. Haar, T. Hanks, and L. Baker (1988). Attenuation Near Auza, California, *Bull Seism. Soc. Amer.*, **87**, 672-691.

Hudson, D.E. (1962). Some Problems in the Application of Spectrum Techniques to Strong-Motion Earthquake Analysis, *Bull. Seism. Soc. Amer.*, **52**, 417-430.

Johnson, L.R. and W. Silva (1981). The Effect of Unconsolidated Sediments Upon the Ground Motion During Local Earthquakes, *Bull Seism. Soc. Amer.*, **71**, 127-142.

Joyner, W.B., R.W. Warrick and A.A. Oliver, III (1976). Analysis of Seismograms from a Downhole Array in Sediments Near San Francisco Bay, *Bull. Seism. Soc. Amer.*, **66**, 937-958.

Lee, V.W. and M.D. Trifunac (1974). A Note on the Accuracy of Computed Ground Displacements from Strong Motion Accelerograms, *Bull. Seism. Soc. Amer.*, **64**, 1209-1219.

Lee, V.W. and M.D. Trifunac (1982). EQUINFOS (The Strong -Motion Earthquake Data Information System) Department of Civil Engineering, Report No. 82-01, University of Southern Calif., Los Angeles, California.

Lee, V.W. and M.D. Trifunac (1987). Strong Earthquake Ground Motion Data in EQUINFOS: Part I, Department of Civil Engineering, Report No. 87-01, University of Southern California, Los Angeles, California.

Lee, V.W. and M.D. Trifunac (1990). Automatic Digitization and Processing of Accelerograms Using PC, Dept. of Civil Eng., Rep. No. 90-03, Univ. Southern California, Los Angeles, California.

Malin, P.E. and J.A. Walker (1985). Preliminary Results from Vertical Seismic Profiling of Oroville Microearthquake S-waves, *Geophys. Res. Lett.*, **12**, 137-140.

Mitchell, B.J. and H.J. Hwang (1987). Effect of Low Q Sediments and Crustal Q on L_g Attenuation in the United States, *Bull. Seism. Soc. Amer.*, **77**, 1197-1210.

McDonal, J.F. F.A. Angona, R.L. Mills, R.L. Sengbush, R.G. Van Nostrand and J.E. White (1958). Attenuation of Shear and Compressional Waves in Pierre Shale, *Geophysics*, **23**, 421-439.

Novikova, E.I. and M.D. Trifunac (1991). Instrument Correction for the Coupled Transducer-Galvanometer Systems, Dept. of Civil Eng. Report No. CE 91-02, Univ. Southern California, Los Angeles, California.

Novikova, E.I. and M.D. Trifunac (1992). Digital Instrument Response Corrections for the Force Balance Accelerometer, *Earthquake Spectra*, **8**(3), 429-442.

Papageorgiou, A.S. (1988). On Two Characteristic Frequencies of Acceleration Spectra: Patch Corner Frequency and $f_{\max}$, *Bull. Seism. Soc. Amer.*, **78**(2), 509-529.

Papageorgiou, A.S. and K. Aki (1983a). A Specific Barrier Model for the Quantitative Description of Inhomogeneous Faulting and the Prediction of Strong ground Motion I. Description of the Model, *Bull. Seism. Soc. Amer.*, **73**(3), 693-722.

Papageorgiou, A.S. and K. Aki (1983b). A Specific Barrier Model for the Quantitative Description of Inhomogeneous Faulting and the Prediction of Strong Ground Motion II. Application of the Model, *Bull. Seism. Soc. Amer.*, **73**, 953-978.

Richter, C.F. (1958). Elementary Seismology, Freeman and Co. S. Francisco.

Seed, H.B., C. Ugas and J. Lysmer (1976). Site Dependent Spectra for Earthquake Resistant Design, *Bull. Seism. Soc. Amer.*, **66**, 221-243.

Singh, S. and R.B. Herrmann (1983). Regionalization of Crustal Coda Q in the Continental United States, *Jour. Geoph. Res.*, **88**(B1), 527-538.

Singh, S.K., R.J. Apsel, J. Fried, and J. Brune (1982). Spectral Attenuation of SH waves Along the Imperial Fault, *Bull. Seism. Soc. Amer.*, **72**, 2003-2016.

Todorovska, M. and V.W. Lee (1990). A Note on Response of Shallow Circular Valleys to Rayleigh Waves; Analytical Approach, *Earthquake Eng. and Eng. Vibration*, **10**(1), 21-34.

Todorovska, M. and V.W. Lee (1991). Surface Motion of Circular Alluvial Valleys of Variable Depth for Incident Plane SH Waves, *Soil Dyn. and Earthquake Eng.*, **10**(4), 192-200.

Trifunac, M.D. (1971). Zero Baseline Correction of Strong-Motion Accelerograms, *Bull. Seism. Soc. Amer.*, **61**, 1201-1211.

Trifunac, M.D. (1972). A Note on Correction of Strong-Motion Accelerograms for Instrument Response, *Bull. Seism. Soc. Amer.*, **62**, 401-409.

Trifunac, M.D. (1973). Analysis of Strong Earthquake Ground Motion for Prediction of Response Spectra, *Int. J. of Earthquake Engineering and Struct. Dynam.*, **2**(1), 59-69.

Trifunac, M.D. (1976a). Preliminary Empirical Model for Scaling Fourier Amplitude Spectra of Strong Ground Acceleration in Terms of Earthquake Magnitude, Source to Station Distance and Recording Site Conditions, *Bull. Seism. Soc. Amer.*, **66**, 1343-1373.

Trifunac, M.D. (1976b). Preliminary Analysis of the Peaks of Strong Earthquake Ground Motion-Dependence of Peaks on Earthquake Magnitude, Epicentral Distance and the Recording Site Conditions, *Bull. Seism. Soc. Amer.*, **66**, 189-219.

Trifunac, M.D. (1989a). Dependence of Fourier spectrum Amplitudes of Recorded Strong Earthquake Accelerations on Magnitude, Local Soil Conditions and On Depth of Sediments, *Int. J. Earthquake Eng. and Struct. Dynam.*, **18**, 999-1016.

Trifunac, M.D. (1989b). Empirical Scaling of Fourier Spectrum Amplitudes of Recorded Strong Earthquake Accelerations in Terms of Magnitude and Local Soil and Geologic Conditions, *Earthquake Eng. and Eng. Vibration*, **9**(2), 23-44.

Trifunac, M.D. (1990). How to Model Amplification of Strong Earthquake Motions by Local Soil and Geologic Site Conditions, *Int. J. Earthquake Eng. and Struct. Dynam.*, **19**(6), 833-846.

Trifunac, M.D. (1991). M_L^{SM}, *Int. J. Soil Dynam. and Earthquake Eng.*, **10**(1), 17-25.

Trifunac, M.D. and A.G. Brady (1975). On the Correlation of Seismic Intensity Scales with the Peaks of Recorded Strong Ground Motion, *Bull. Seism. Soc. Amer.*, **65**, 139-162.

Trifunac, M.D. and D.E. Hudson (1970). Laboratory Evaluation and Instrument Corrections of Strong Motion Accelerographs, Earthquake Engineering Research Laboratory, EERL 70-04, California Institute of Technology, Pasadena.

Trifunac, M.D. and V.W. Lee (1985). Preliminary Empirical Model for Scaling Fourier Amplitude Spectra of Strong Ground Acceleration in Terms of Earthquake Magnitude Source to Station Distance, Site Intensity and Recording Site Conditions: Second Paper, with V.W. Lee, Department of Civil Engineering, Report No. 85-03. University of Southern Calif., Los Angeles, California.

Trifunac, M.D. and V.W. Lee (1987). Direct Empirical scaling of Response Spectral Amplitudes from Various Site and Earthquake Parameters, U.S. Nuclear Regulatory Commission, Report NUREG/CR-4903, Vol 1.

Trifunac, M.D. and V.W. Lee (1989). Empirical Models for Scaling Fourier Amplitude Spectra of Strong Ground Acceleration in Terms of Earthquake Magnitude, Source to Station Distance, Site Intensity and Recording Site Conditions, *Int. J. Soil Dynamics and Earthquake Eng.*, **8**(3), 110-125.

Trifunac, M.D. and V.W. Lee (1990). Frequency Dependent Attenuation of Strong Earthquake Ground Motion, *Int. J. Soil Dynam. and Earthquake Eng.*, **9**(1), 3-15.

Tullos, F.N. and A.C. Reid (1969). Seismic Attenuation of Gulf Coast Sediments, *Geophysics*, **34**, 516-528.

Wong, H.L. and M.D. Trifunac (1977). Effects of Cross-Axis Sensitivity and Misalignement on Response of Mechanical–Optical Accelerographs, *Bull. Seism. Soc. Amer.*, **67**, 929-956.

Woodgold, C.R.D. (1990). Estimation of Q in Eastern Canada Using Coda Waves, *Bull. Seism. Soc. Amer.*, **80**(2), 411-429.

APPENDIX A: NOTATION

a - empirical scaling coefficient in description of the fault length $L = a \times 10^{bM}$;

a_0, a_1 - scaling coefficients for Q;

a_M - coefficient in $\log_{10} N_M = a_M - b_M M$;

$\mathcal{A}_0(T)$ - parabola w.r.t. $\log_{10} T$ which defines the frequency dependent attenuation in $\Delta^{\mathcal{A}_0(T)}$ (see Eq. (2));

$$\mathcal{A}_0(T) = \begin{cases} -0.732 & T \geq 1.8 \text{ sec} \\ a + b \log_{10} T + C(\log_{10} T)^2 & T < 1.8 \text{ sec} \end{cases}$$

where $a = -0.767$, $b = 0.271$ and $c = -0.526$, (see Trifunac and Lee, 1989).

$\mathcal{A}tt(\Delta, M, T)$ - a function describing the frequency dependent ($f = 1/T$) attenuation of the spectral amplitudes versus distance Δ and magnitude M (is defined by Eq. (2));

a_{NF}, a_{FF} - a function describing the contribution of near-field ($a_{NF} = e^{-\frac{3S_1}{4S}}$) and of far-field spectra $\left(a_{FF} = 1 - e^{-\frac{3S_1}{4S}} \right)$ to the Fourier Amplitude spectra of strong motion acceleration, $FS(T)$

A - fault area, $A = WL$ (km^2);

A_0 - area of a single path (asperity);

A_Q - zero frequency asymptote in $FS(f) = A_Q e^{-\pi k f}$;

b - empirical scaling coefficient in $L = a \times 10^{bM}$;

b_0, b_1 - scaling coefficients for Q;

b_M - coefficient in $\log_{10} N_M = a_M - b_M M$;

$b_i(T)$ - empirical scaling "coefficients" in Eq. (1);

$b_i^{(j)}(T)$ - empirical scaling coefficients in Eq. (1) for the indicator variable j;

c - empirical scaling coefficient in $W = c \times 10^{dM}$

C_0 - scaling "coefficient" relating the average fault displacement, $\overline{d}$, or the average fault dislocation, $\overline{u}(\overline{u} = 2\overline{d})$, with the source dimension r and the rigidity of the surrounding rocks, μ;

C_0^* - proposed "average" trend of C_0 versus M;

C_s - a scaling constant (see Eq. (26) and (27));

d - empirical scaling coefficient in $W = c \times 10^{dM}$; also used as 1) the position above surface for the center of a circular ray path of radius R_0, $d = v_0/v_1$ (see Fig. 31), and 2) the width of the nonlinear tip of the fault breaking through an unfractured fault zone;

d_p - permanent ground displacement, $d_p = d_{NF}(t)$, for $t \to \infty$;

$d(t)$ - displacement of the ground motion versus time;

$d_{NF}(t)$ - near field strong motion displacement (for $\Delta < S$);

$d_{FF}(t)$ - far-field strong motion displacement (for $\Delta >> S$);

$\overline{d}$ - average of $d_{NF}(t)$, for $t \to \infty$, on the fault surface;

$D(\overline{M}_L^{SM})$ - difference between M_L^{SM} and M_p;

E_s - seismic energy;

$E[\sigma]$ - expected value of σ;

f - frequency (Hz); also used as a coefficient in $W = e + fM$;

f_1 - corner frequency, $f_1 = \left(\frac{L}{v} + T_0\right)^{-1}$ (Hz);

f_2 - corner frequency, $f_2 = 2.2/W$ (Hz);

f_p - frequency where $FS(f)$ has peak amplitude (see Fig. 1);

f_{co} - frequency ($= 1/T(N_c)$) below which Eq. (1) is not valid (see Table II)

f_H - cut-off frequency, $f_H = Q\beta/(5\Delta)$;

$f_{\max}$ - high frequency corner or cut-off frequency.

$FS(T)$, $FS(\omega)$, $FS(f)$ - Fourier amplitude spectrum of strong motion acceleration at period T, circular frequency ω, or frequency f.

$FS_{NF}(w)$ $FS_{NF}(T)$, $FS_{FF}(w), FS_{FF}(T)$ - Fourier amplitude spectra of near-field and far-field strong motion acceleration, at frequency ω, or period T;

g_0, g_1 - coefficients in $Q = g_0 + g_1\ (y - d)$;

$G4RM$ - group of four regression models. Model 4 is shown in Eq. (1). (1. MAG-SITE; 2. MAG-DEPTH; 3. MAG-SITE-SOIL; 4. MAG-DEPTH-SOIL);

h - depth (thickness) of the sedimentary layer beneath the station (km);

h_0 - depth (below the surface) of the top edge of a vertical fault plane (km);

H - focal depth (km);

k - slope of $\log_{10} M_0$ versus M (see Eq. (28));

L, $L_{\min}$ - fault length and minimum fault length (km);

L_{F_i} - length of L_T faults in a region;

L_M - length of a patch (for $M < 5$ to 6);

M - magnitude;

M_* - cut off magnitude;

$M_{\min}$, $M_{\max}$ - minimum and maximum magnitudes defining the range $M_{\min} < M < M_{\max}$ where the strong motion amplitudes begin to saturate. For $M > M_{\max}$, $FS(T)$ in Eq. (1) is constant, i.e. does not grow with M;

M_0 - seismic moment ($= \mu\bar{u}A$) (dyne cm);

M_0^{SM} - seismic moment computed from strong motion data;

M_L - the local magnitude scale (Richter, 1958);

M_L^{SM} - local magnitude computed from strong motion accelerograms;

M_p - "magnitude" as published in various catalogues (without specification of the wave type, used, or the procedure employed);

M_s - surface wave magnitude;

N_p - number of peaks of a random function ($N_p = WL/A_0$);

N_M - number of earthquakes of magnitude $M \pm \frac{\Delta M}{2}$ in a region during a given time;

$p(\varepsilon, T)$ - probability density function describing the distribution of $\varepsilon(T)$ in Eq. (7);

Q - the quality factor;

Q_0 - the value of Q at $f = 1$ Hz;

Q_A - the average value of Q for a range of depths;

r - the characteristic source dimension (see Table III) (km);

R - epicentral distance (km);

R_0 - transition distance where the frequency dependent attenuation $Att(\Delta, M, T)$ becomes $\sim R/200$ as in $\log_{10} A_0(R)$ (Richter, 1958); R_0 is also used to represent the radius of the ray path in Fig. (31);

s - the geologic site condition parameter ($s = 0$ for sediments, $s = 2$ for basement rock and $s = 1$ for intermediate sites);

s_L - a parameter describing the local soil site condition ($s_L = 0$ for "rock" sites, $s_L = 1$ stiff sites, and $s_L = 2$ for deep soil sites);

S - the source dimension used in Eq. (3) and defined by Eq. (4). Also used in Eq. (29); the "source dimension" $S = .01 \times 10^{.5M}$(km);

$S_L^{(1)}$, $S_L^{(2)}$ - indicator variables describing the local soil conditions (see Eq. (5));

S_0 - the coherence radius (Gusev, 1983) of the source (km);

S_1 - distance between the station and the top of a vertical fault (km);

t - time (sec);

t' - delayed time, $t' = t - R/\beta$;

T - period of vibration, $T = 1/f$ (sec);

$T(N)$ - periods ($N = 1,2,...,12$) for which $b_i(T)$, $M_{\min}$, $M_{\max}$, $\mu(T)$ and $\sigma(T)$ are prescribed in Table I. Eq. (1) can be used for $N < N_c$ (see Table II) i.e. for $T < T(N_c)$;

T_p - period where $FS(T)$ is maximum, $T_p = 1/f_p$;

T_c - cut off period $T_c = T(N_c) = 1/f_{co}$ (see Table II);

T_0 - the dislocation rise time, $T_0 \sim \frac{\overline{u}\mu}{\sigma\beta}$ (sec);

u, $u_{\max}$ - dislocation amplitude, maximum dislocation amplitude;

$\overline{u}$ - dislocation averaged over the fault surface;

v - an indicator variable; v = 0 for horizontal motion, v = 1 for vertical motion;

v - dislocation velocity (km/sec);

v_0, v_1 - coefficients in Eq. (60);

W, $W_{\min}$, W_* - fault width, minimum fault width, a distance such that $W = \xi W_*$, for $0 < \xi < 1$, (km);

W_{F_i} - width of L_T faults in a region;

W_M - the width of a patch (for $M \lesssim 5$ to 6);

y_A - the depth, $y_A = (R_0 - d)/2$, where the average Q is evaluated;

α - corner frequency in the Brune's spectrum (see Eq. (18));

α_0 - scaling constant (in $\overline{u} = \alpha_0 L$);

β - velocity of shear waves, $\beta = (\mu/\rho)^{1/2}$ (km/sec);

γ - exponent in $Q = Q_0 f^{\gamma}$;

Δ - the "representative" source to station distance (see Eq. (3));

ε - a factor $(0 < \varepsilon < 1)$ indicating a fraction of the stress drop σ (Brune, 1970);

$\varepsilon(T)$ - residuals, $\varepsilon(T) = \log_{10} FS(T) - \log_{10} \widehat{FS}(T)$ (see Eq. (6));

η - the efficiency in the expression for the apparent stress, $\sigma_a = \eta\overline{\sigma}$;

k - the high frequency attenuation constant, $k = \Delta/(Q\beta)$;

μ - shear modulus, $\mu = \rho\beta^2$ (dyne/cm^2);

$\mu(T)$ - the mean of distribution $p(\varepsilon, T)$;

π - constant (=3.14159);

ρ - material density (gr/cm^3);

σ - effective stress (also used as stress drop, Brune, 1970), defined as the difference of stress before the earthquake and the frictional stress during faulting;

$\overline{\sigma}$ - root-mean-square of the peak stress amplitudes on the fault surface (different from $\overline{\sigma}$ in $\sigma_a = \eta\overline{\sigma}$);

$\sigma(T)$ - standard deviations of the distribution $p(\varepsilon, T)$ in Eq. (7);

σ_a - the apparent stress, also designated by $\eta\overline{\sigma}$, here and in literature (note that in this paper $\overline{\sigma}$ has different meaning when it is used alone (without η), e.g. to represent the root mean square amplitude of the peaks of the stress on the fault surface;

τ - the characteristic source time, $\tau = 1/f_1 = \frac{L}{v} + T_0$;

ω - circular frequency, $\omega = 2\pi f$ (rad/sec);

$\Omega_{NF}(\omega)$, $\Omega_{FF}(\omega)$ - near-field and far-field Fourier amplitude spectra of strong motion displacement;

ω_1, ω_2 - corner frequencies $\omega_1 = 2\pi f_1$, $\omega_2 = 2\pi f_2$, (rad/sec).